Investigation of Power Generation by Small-Scale Wind Turbines

How a Vortex affects Power Generation

Master's Thesis in Automotive Engineering

Till Rune Gebel

DEPARTMENT Mechanics and Maritime Sciences

CHALMERS UNIVERSITY OF TECHNOLOGY
Gothenburg, Sweden 2021
www.chalmers.se

Master's thesis 2021:69

Investigation of the Power Generation by Small-Scle Wind Turbines

How a Vortex affects Power Generation

TILL RUNE GEBEL

CHALMERS
UNIVERSITY OF TECHNOLOGY

Department of Mechanics and Maritime Sciences
Division of Fluid Dynamics
Chalmers University of Technology
Gothenburg, Sweden 2021

Investigation of the Power Generation by Small-Scale Wind Turbines
How a Vortex impacts Power Generation
Till RUNE GEBEL

Supervisor: Dr. Salim Azzouz, Midwestern State University &
Dr. Pranaya Pokharel, Midwestern State University
Examiner: Lars Davidson, Division of Fluid Dynamics, Chalmers University of Technology

Master's Thesis 2021
Department of Mechanics and Maritime Sciences
Division of Fluid Dynamics
Chalmers University of Technology
SE-412 96 Gothenburg
Telephone +46 31 772 1000

Typeset in LaTeX
Printed by Chalmers Reproservice
Gothenburg, Sweden 2021

Investigation of the Power Generation by Small-Scale Wind Turbines
How a Vortex affects Power Generation
TILL RUNE GEBEL
Department of Mechanics and Maritime Sciences
Chalmers University of Technology

Abstract

The area of wind turbines is the subject of many contemporary researches given the importance of the field for electricity production. The purpose of this research project is to use additive manufacturing techniques to 3-D print several resin based wind turbine profiles, and test them for electricity production in the McCoy School of Engineering closed loop wind tunnel at the Midwestern State University. Different prototypes of wind turbines will be designed, printed, and tested for their performance and power production using a small scale electric generator. Different obstacle designs will be tested to efficiently channel the air flow toward the blades of the wind turbine. This coupling between obstacles and wind turbines is designed to increase the efficiency and the power production of the wind turbine. Inside the wind tunnel, the blades of the wind turbine will be subjected to different wind speeds. Their optimal performance will be experimentally determined using LabVIEW software. This research puts an emphasis on vertical axis wind turbines for the purpose to shift the placement of the gearbox and the generator from high horizontal elevation configuration to a ground level configuration. This design shows to have a significant impact on the efficiency, dimension, cost, and maintenance of the wind turbine themselves. This vertical configuration opens the possibility to equip future wind turbines with a high powered generator. Equipment and supplies for this research requires the purchase of miniature generators, resin for 3D printing of the blades, and electrical measurement devices. A LabVIEW program will be created to monitor continuously the output power of the wind turbine as well as the voltage and current output at different wind speeds and resistance loads. Furthermore, the flow field around the turbine blades, will be investigated using a Particle Image Velocimetry (PIV) system. The PIV system will be essentially used to check the system design and optimize the flow channeled toward the wind turbine blades. Using the powerful fluid dynamic sofware ANSYS, a simulation will be run to obtain a velocity flow field around the obstacle.

Keywords: wind turbine, vertical wind turbine, 3-D printing, PIV, CFD, vortex.

Acknowledgements

I am giving my appreciations to my two supervisors and mentors Dr. Salim Azzous and Dr. Pranaya Pokharel who always supported me with beneficial and valuable input, feedback, and guidance during the project. Their determination made it possible that my goals were reached. I also thank Ernuel Tonge for the help with the electrical part of the project. I am also thankful for Chalmers University and Midwestern State University for the opportunity to use their resources. Last, I express my gratitude towards Lars Davidson for being my examiner.

TILL RUNE GEBEL, Gothenburg, June 2021

Contents

List of Figures

List of Tables

1
Introduction

1.1 Background

The engineering and design of windmills goes back as far as 3000 years. That makes them extremely old. Stone windmills have been discovered near Alexandria in Egypt eventhough there is no prove that Egyptians, Phoenicians, Greeks, or Romans really knew how windmills function or what to do with them [2]. Historians mention the year 644 A.D. as the year where the first evidence of windmills originated in the region of Seistan which is on the Persian-Afghan border. A sketch and description from the year 945 show vertical windmills used to mill grain. Those can still be found in today's Afghanistan [2]. The same style of windmill were used in China to drain rice fields. It is not known if the Chinese used those before the Persians [2]. The windmills that are widely known through this world are, in contrast to the ones mentioned above, windmills with a horizontal axis of rotation. Their origin comes most likely from Europe, where sources mention a windmill in the Duches of Normandy in the year 1180 and in the province of Brabant in 1119 [2]. Quickly, windmills spread all over to Europe and developed into the fom that is now widely known[2]. The need of electricity started in New York (1882) and Berlin (1884) where the first power plants where built [3]. The demand for electricity was rising rapidly and therefore new inventions and innovations had to be tried. But the first tries to generate power from windmills did not happen until most large cities were already supplied with electricity. 'Do-it-yourself enthusiasts in America' were most likely the first ones to try power generation with windmills used to pump water [2]. However, the first significant success in generating electricity took place in Denmark where a pioneer named Poul La Cour built a wind turbine driving a dynamo [2]. Generally, there are two different vertical wind turbine designs. One, the Savonius Wind Turbine, and second, the Darrieus Wind Turbine.

1.2 Savonius Wind Turbine

The Savonius Wind Turbine, also called the Savonius-Rotor, is commonly found on trains or delivery vans as air ventilators. Also the cup anemometer used to measure wind velocity, is a very common application of a Savonius Wind Turbine [2]. As the design suggests, this type of wind turbine only spins as fast as the passing wind passes by. The turbine is 'scooping' air [13]. A simple schematic of a Savonius Wind Turbine or Savonius-Rotor is shown in Figure 1.1. Hau also states, that sometimes Savonius Wind Turbines are used for small simple wind rotors for driving small

water pumps. In this project, it is tried to design a Savonious inspired turbine that is suitable for electricity generation.

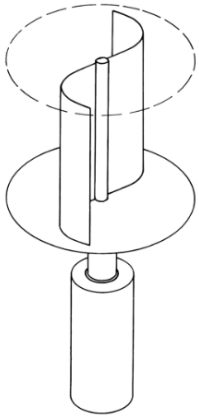

Figure 1.1: Schematic of Savonius-Rotor[2]

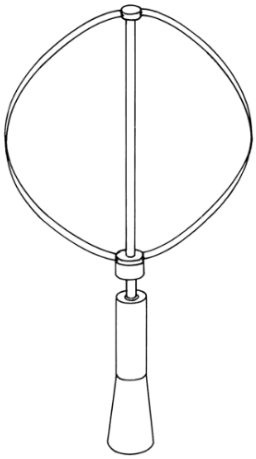

Figure 1.2: Schematic of Darrieus-Rotor[2]

1.3 Darrieus Wind Turbine

The Darrieus Wind Turbine, or Darrieus-Rotor like Erich Hau calls it, are designed to use aerodynamic lift. The first design was proposed by a French Engineer called Darrieus. Darrieus-Rotors are difficult to manufacture because of the complicated shapes of the rotor blades [2]. A simple schematic of a Darrieus Wind Turbine is shown in Figure 1.2 Darrieus Wind Turbines have been used for large scale energy generation in The United States by the former American Flowing Company. They used a rotor diameter of 19 m and created a power output of 170 kW. Unfortunately this company does not exist anymore. A variation of the Darrieus-Rotor, the 'H-Rotor', created a power output of 300 kW in Heidelberg until the beginnings of 1990. This specific variation has straight blades connected to the rotor shaft instead of curved blades. Unfortunately the costs of producing such turbines is too high to make them lucrative and a adequate alternative to the commercially used horizontal-axis rotors [2].

1.4 Vortices

According to the Merriam-Webster Dictionary a vortex is a mass of fluid with a whirling or circular motion that tends to form a cavity or vacuum in the center of the circle and to draw toward this cavity or vacuum bodies subject to its action [4]. Vertices are a very powerful phenomena. A perfect example for that is a tornado. Tornadoes can reach speeds of up to 100 mph and can be catastrophic events [5]. In the case of this thesis, the immense force of a vortex is used for good. There is many ways of forming a vortex. It can occur naturally but also can be created. For example, in a tornado, the vertices occur naturally. When the air flows around an

airplane wing or a paddle gets dragged through water, those vertices get created by humans. In this project, an obstacle is used to create vertices. Bengt Sunden shows the flow around a smooth tube for different flow regimes. At a Reynolds number of 5-15 $<$ Re $<$ 40 a fixed pair of vertices in the wake is shown [7]. This would be the desired outcome in this project as well. Roya and Shademani Ghadimi et. al. state that this is also possible around a triangular cylinder [8]. They invested the Reynolds Number range 1.4 $<$ Re $<$ 38.03. The first vertices started forming at Re=2.77 but very small. Starting at Re=20.8, the first clearly shown symmetric vertices appear. The following vertices are more turbulent. In Sundens study, airflow at a higher Reynolds Number show the same result. Vortices start shedding first sinusoidal, then randomly. In this thesis, a vertical wind turbine is placed in the vortex, created by air flowing past an obstacle. The goal is to create an area with very high wind speeds to make the turbines spin faster than they would spin if the vortex would not be there and the wind would just come straight at the wind turbine.

1.5 It's significance to the Automotive Sector

In Sweden, about 12% of the total electricity comes from wind turbine energy and it is only rising [9]. In general, electrification is an important factor in today's world and automotive field. Electric vehicles produce less to no harmful emissions like CO_2, NO_x, and particle matter (PM) and are also quieter than conventional combustion engine vehicles. Less harmful emissions result in reduced health problems caused by exhaust gases and by the automotive industry. Besides, noise pollution is and can cause physical problems, physiological problems, sleep and behavioral disorders, and memory and concentration losses to residents, pedestrians, drivers and so on. Because of the pollution, caused by all kind of vehicles, cities are starting to ban certain vehicles from certain zones in cities and electric vehicles are starting to be a solution to the problem. Wind energy is one of the renewable energy sources and therefore widely supported when serving additional electricity demands. With the increase of electrified vehicles and the resulting higher overall electricity consumption new and innovative forms of power production are needed. Wind turbine energy is extensively used for powering electric cars.

2

Theory

The following sections describe the theory behind the used methods in this Thesis.

2.1 Computational Fluid Dynamics

Computational Fluid Dynamics (CFD) is a form of virtual prototyping. It is the standard method to develop new products in the automotive industry and other major industries. In chemical engineering CFD is used to model reactors, separations, and heat transfer [18]. In this thesis it is focused on flow simulation, to be more precise the turbulent flow simulation. There is Navier-Stokes equations for turbulent flows but unfortunately, it is not possible to solve these equations for real engineering applications. This is because of the properties of the flow [18]. It is possible to do a Direct Solution of the Navier-Stokes equations (DNS) for small systems, for example at small Reynolds Numbers. Another method, the large-eddy simulation (LES) filters out the fine-scale turbulence and only resolves the large-scale turbulence. It is possible to do simulations on a fast computer. However, for some applications it can take several days or weeks to acquire good results [18]. In addition to those two methods, Reynolds-averaged Navier-Stokes (RANS) methods can be used. In fact, RANS methods are the most widely known and applied methods used for engineering simulations. Turbulent fluctuations are time averaged and velocity averages can be simulated. The method used here is the Realizable $k - \epsilon$. It is part of the Two-equation models. Usually, they predict velocity and length scales of turbulence with transport equations. They give good results for a wide variety of engineering applications. The Realizable $k - \epsilon$ model is a modification of the standard $k - \epsilon$ model with improved simulations for swirling flows and flow separation. This is exactly what is needed here. However, it is not as stable as the standard $k - \epsilon$ model [18].

2.2 Computer Aided Design

Computer Aided Design (CAD), as the the name suggests, is a design process in which a computer software is used to design a part.It has several benefits over traditional sketching by hand like the visualization, detail and accuracy of the drawing and part, optimization in case something went wrong during the design process, and realization. CAD makes it easier to realize designs in the form of physical objects with the help of new fabrication technologies [19]. CAD models can be sent directly

to a 3D printer and get printed. Today, all engineering drawings are made in a CAD software.

2.3 Particle Image Velocimetry

Particle Image Velocimetry (PIV) makes it possible to visualize velocity flow field. Small tracer particles are added to the flow and from the position of those particles at two time instances, the fluid motion is made visible [20]. The ideal tracer particles appear when the particles follow the exact motion of the fluid, do not alter the flow or the fluid properties, and do not interact with each other [20]. The velocity of the particles is measured from their displacement $D(X; t', t'')$ in a finite time interval $\Delta t = t'' - t'$,

$$D(X; t', t'') = \int_{t'}^{t''} v[X(t), t]\, dt, \tag{2.1}$$

where $v[X(t)]$ is the velocity of the tracer particle [20]. In an ideal case, the particles velocity v is equal to the velocity of the flow velocity $u(X, t)$. Since the concept of ideal tracers can only be approximated, D cannot exactly represent u. However, it can also be approximated.

$$||D - u * \Delta t|| < \epsilon, \tag{2.2}$$

where ϵ is a small finite error. When injecting particles with a high pressure into the flow, the seeding concentration rises with pressure. When the seeding concentration is high, it is not possible to identify matching particle pairs clearly. Consequently the tracer particles are usually described as a pattern. This pattern is given as,

$$G(X, t) = \sum_{n=1}^{N} \delta[X - X_i(t)] \tag{2.3}$$

N represents the total number of particles in the flow system, $\delta(X)$ is the Dirac $\delta - function$, and $X_i(t)$ is the position vector of the particle with index i at time t [20]. For a good visualization, it is important to seed the flow as homogeneous as possible. In planar domain PIV, a cross section is lit up with a thin light sheet, usually with a laser. Pictures are taken of the reflecting particles. It is assumed, thickness of the lit up sheet ΔZ_0 only changes in the z-direction. Another assumption is that all particles are in focus. This is granted when ΔZ_0 is less than the particles focal depth [20]. The visualization of the tracer pattern can be described as a projection of the tracer pattern on the planar domain. The following equation describes this mathematically.

$$g(x, y) = \frac{1}{I_Z} \int I_o(Z) G(X, Y, Z)\, dZ, \tag{2.4}$$

where $x = MX$, $y = MY$, $I_o(Z)$ is the light-sheet intensity profile with a maximum I_Z, and M is the image magnification. How well the velocity vectors are represented directly depends on the concentration of the tracer particles within the laser sheet. The density can be defined as:

$$N_s = C \Delta Z_0 M^{-2} \frac{\pi}{4} d_t^2, \tag{2.5}$$

where C is the number of density of seeding. When $N_s << 1$ the a low source density exists and the average distance between particles is significantly larger than the particle-image diameter. A high source density, $N_s >> 1$, particle images overlap [20].

2.4 Vertical Wind Turbines

Vertical Axis Wind Turbines (VAWT) are very beneficial in its application for the power generation. They have a simple structure and assembly compared to Horizontal Axis Wind Turbines (HAWT). Because of the vertical orientation, the electric generator and possible gear system can be placed on the ground. It makes them easier accessible for maintenance purposes. HAWT have to face the direction of the wind to function properly. A deviation of a small degrees can cause significant changes in the power production. On the other hand, VAWT do not have to face the direction of the wind. No matter what direction they face, the produced power stays the same if the wind speed is consistent [16]. However, VAWT have significantly lower efficiency and higher material demand. This is part of the reason why HAWT are more used. In fact, almost all wind power plants consist of HAWT [16]. The Tip Speed Ratio (TSR) is one of the most important parameters when designing VAWT and HAWT. The TSR is the ratio of circumferential speed (u) in RPS and the real wind speed (v_W) in m/s.

$$\lambda = \frac{u}{v_W} \tag{2.6}$$

[16] [17] The circumferential speed is the speed of the turbine blades. From the TSR the apparent wind speed can be calculated.

$$v_A = v_W\sqrt{1+\lambda^2} \tag{2.7}$$

The optimum TSR for the maximum power production is given as:

$$\lambda = \frac{4\pi}{n}, \tag{2.8}$$

where

$$n = \#\, of\ blades.$$

In general the following TSRs in Table 2.1 are optimum for the maximum power output.

Table 2.1: Optimum TSR for Maximum Power Output depending on # of Blades

# of Blades	**Optimum TSR**
2	≈ 6
3	$\approx$ 4-5
4	≈ 3
6	≈ 2

So if the the calculated TSR matches the TSR in Table 2.1 at a given speed, the turbine has the highest possible power output for this configuration.

3
Methods

3.1 Design Phase

To begin this project brainstorming was conducted to see what was necessary for a good design and good experimental setup. After that a Computational Fluid Dynamics (CFD) Analysis was done to test different obstacles shapes and to see the resulting vortex positioning. Computer Aided Design (CAD) is used to design all parts of the experimental assembly.

3.1.1 CFD Analysis

The CFD Analysis was done using ANSYS Fluent. ANSYS Fluent is a Green-Gauss Finite Volume Method with a Cell-Centered Formulation. [10] In SpaceClaim, an ANSYS Fluent embedded software, a model of the test section with obstacle was designed. Three different obstacle shapes where considered. Figure 3.1 shows an obstacle with sharp edges. The obstacle in Figure 3.2 has the same dimensions as before but the edges are not sharp but round. The last obstacle shape, shown in Figure 3.3 still has the same dimensions but has a perfect triangular shape.

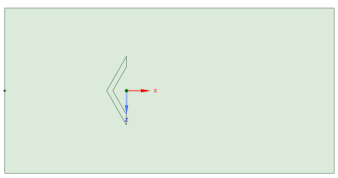

Figure 3.1: Obstacle 1 Sharp Edges

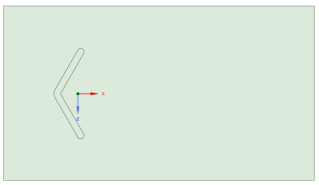

Figure 3.2: Obstacle 2 Round Edges

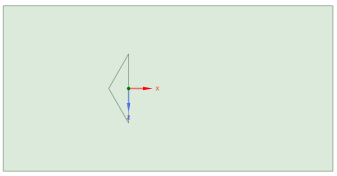

Figure 3.3: Obstacle 3 Triangular Shape

To create the mesh, an element size of $2E - 3m$ is used. Also inflations are added around the edges or the obstacle and the walls because those are the areas where the flow is most likely to change and especially in those areas, a more precise result is needed. The outside walls are treated as walls and not as symmetry which would make the simulation slightly easier. The computed mesh for obstacle 1 is shown in Figure 3.4
The solver type chosen is pressure based and the time model is transient. It is also used the absolute velocity formulation. That mean the equations are solved in a rotating coordination system. In a non-rotating coordinate system the relative velocity would have been used. The turbulent flow model chosen is the Realizable

$k - \epsilon$ with the enhanced wall treatment enabled to intensify the importance of the obstacle impact. The inlet is defined as a velocity inlet with a given velocity and the outlet is a pressure outlet.

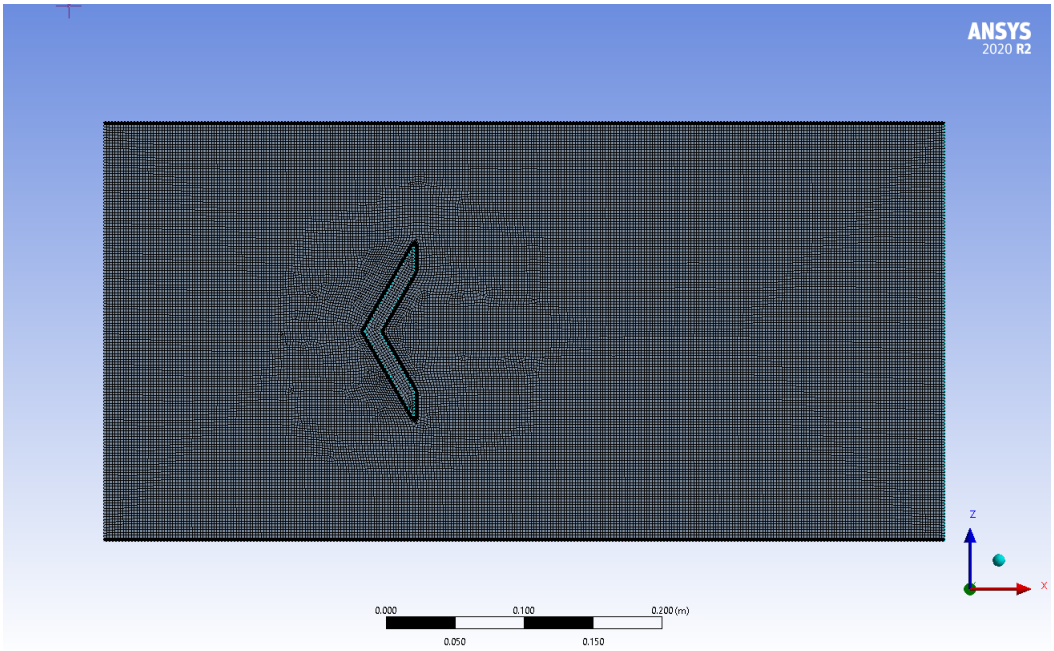

Figure 3.4: Mesh for Obstacle 1 Sharp Edges

3.1.2 Computer Aided Design

To design the obstacle, wind turbines, and other parts needed and used in the experiment, SolidWorks, a 3D CAD software, is used. During this phase multiple designs were proposed and discussed.

3.1.2.1 Obstacle

The Obstacle is needed to create the above mentioned vertices. It has a height of 30cm and is 13cm wide and therefore fits perfectly inside the wind tunnel test section. The sides of the obstacle have a thickness of 1.27cm. The triangular shape will form vortexes behind the obstacle. It is desired to create a low pressure area behind the obstacle as well. This has the aspect of pulling the vertices closer to the obstacle since the length of the test section is limited. The Figures 3.5 to 3.8 show the obstacle. Figure 3.9 is a drawing of the obstacle. At a height of 10cm and 23cm, two slots for the attachment of the support and slider mechanism, to which the turbines are attached, are located. The bottom part of the obstacle has a support platform to provide additional support when attaching the obstacle to the building platform. The isometric view of the obstacle in Figure 3.8 shows the slots, as well as the support platform on the bottom. The slots are 2 cm high and have a hollow area of 5mm to provide perfect fitting of the supports. The back is round to enable the supports to be able to turn.

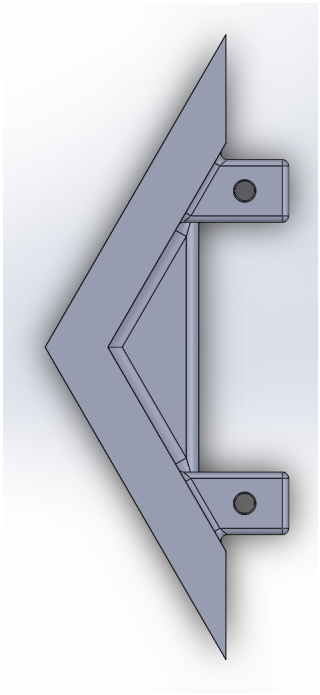

Figure 3.5: Obstacle Top View

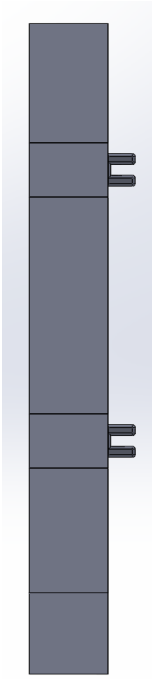

Figure 3.6: Obstacle Side View

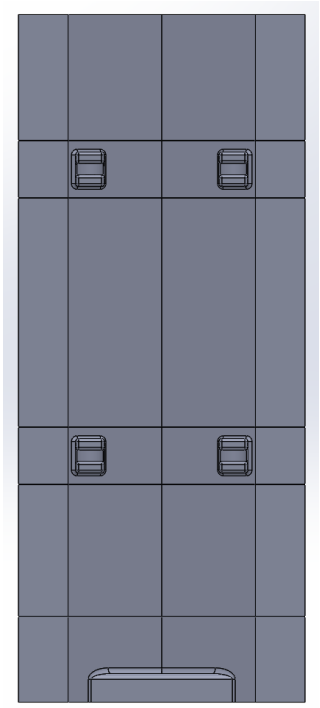

Figure 3.7: Obstacle Back View

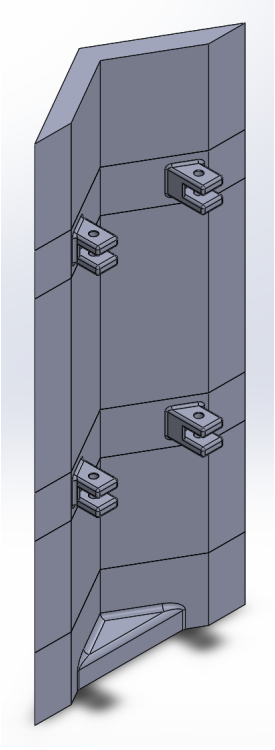

Figure 3.8: Obstacle Isometric View

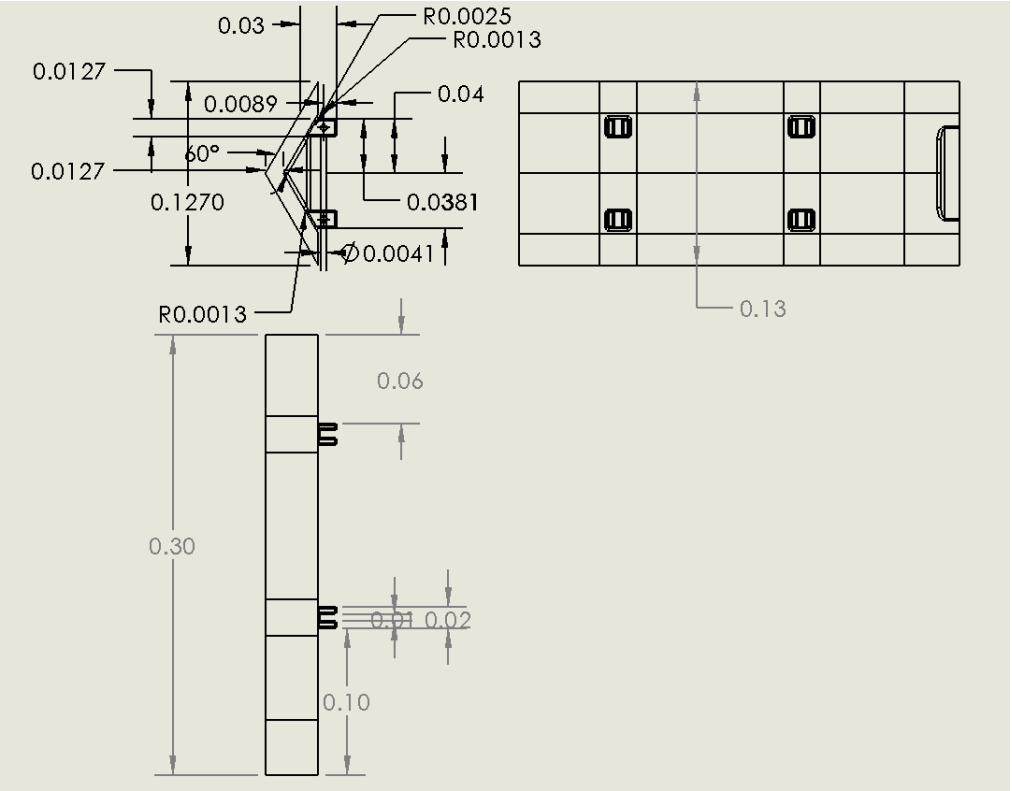

Figure 3.9: Obstacle Drawing

3.1.2.2 Supports

The supports fit into the perfectly shaped slots of the obstacle. Using those supports and the slot at the obstacle, provides the variable positioning of the turbines along a variable radius. They have a length of 12.7 cm , width of 1.27 cm , and height of 0.48 cm. The hollow part of the support has a width of 0.76 cm and height of 0.25 cm. Figure 3.10. to Figure 3.13 show the support. Figure 3.14 is a drawing of the support.

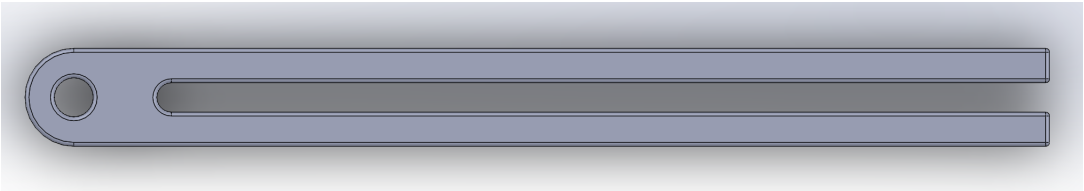

Figure 3.10: Support Top View

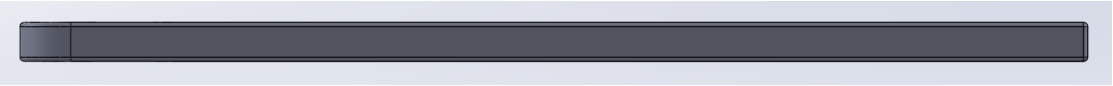

Figure 3.11: Support Side View

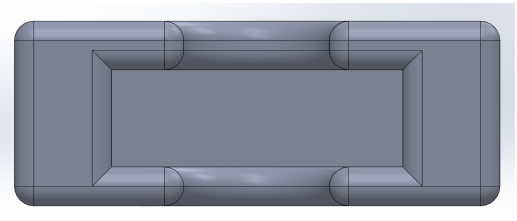

Figure 3.12: Support Back View

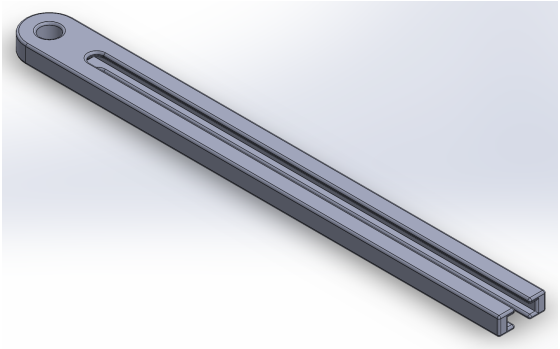

Figure 3.13: Support Isometric View

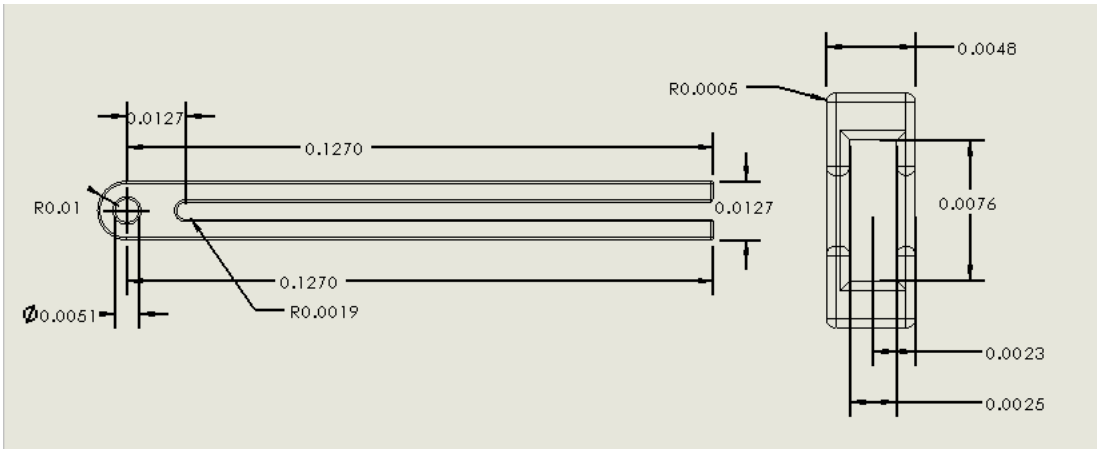

Figure 3.14: Support Drawing

3.1.2.3 Sliders

The sliders perfectly fit in the slots and provide that the radius, along which the turbines can be positioned, can be adjusted and be variable. In this assembly, two different designs of sliders are needed. One for the top and one for the bottom.

3.1.2.3.1 Bottom Slider

Figure 3.15 to Figure 3.17 shows the bottom slider. It has a bigger area where the turbine is attached since below the slider the electric generator inside its 'motorbox' has to be attached as well. Its wider area provides the holes needed to attach the generator with bolts. It was decided to make this the bottom slider because of the natural understanding that the motor should be hanging down from the slider and not 'sitting' on the slider and therefore pressing down on the slider and turbine. The slider is 0.76 cm wide and has a height of 0.25 cm. As before, this fits perfectly inside the designated fitting, in this case the support. The slider has a possible range of 10 cm.

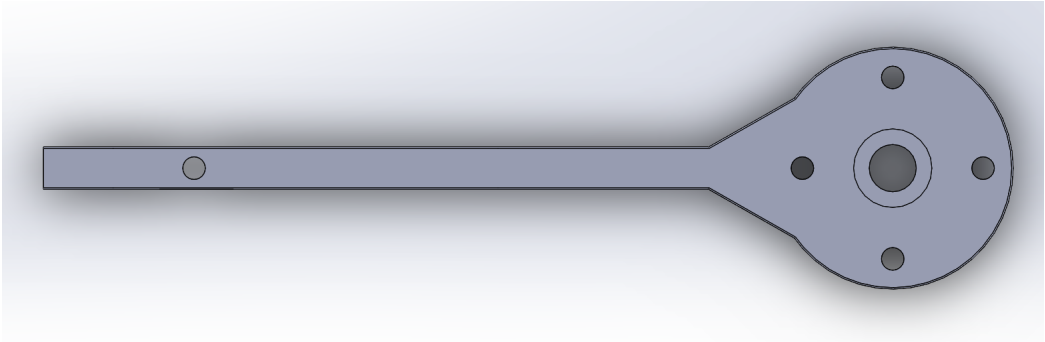

Figure 3.15: Bottom Slider Top View

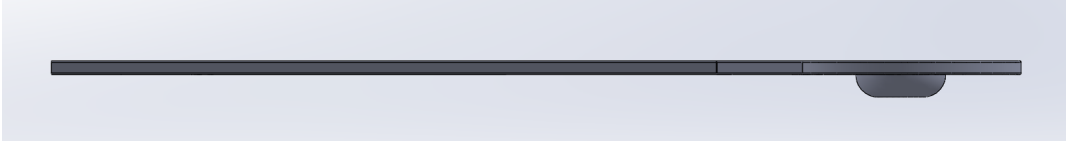

Figure 3.16: Bottom Slider Side View

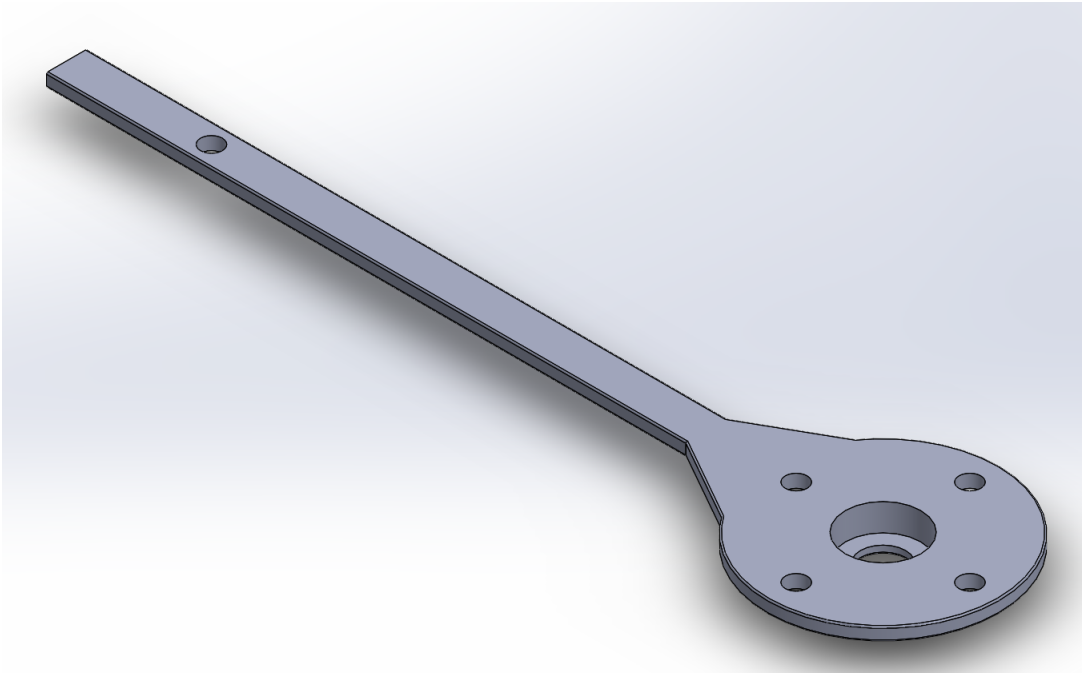

Figure 3.17: Bottom Slider Isometric View

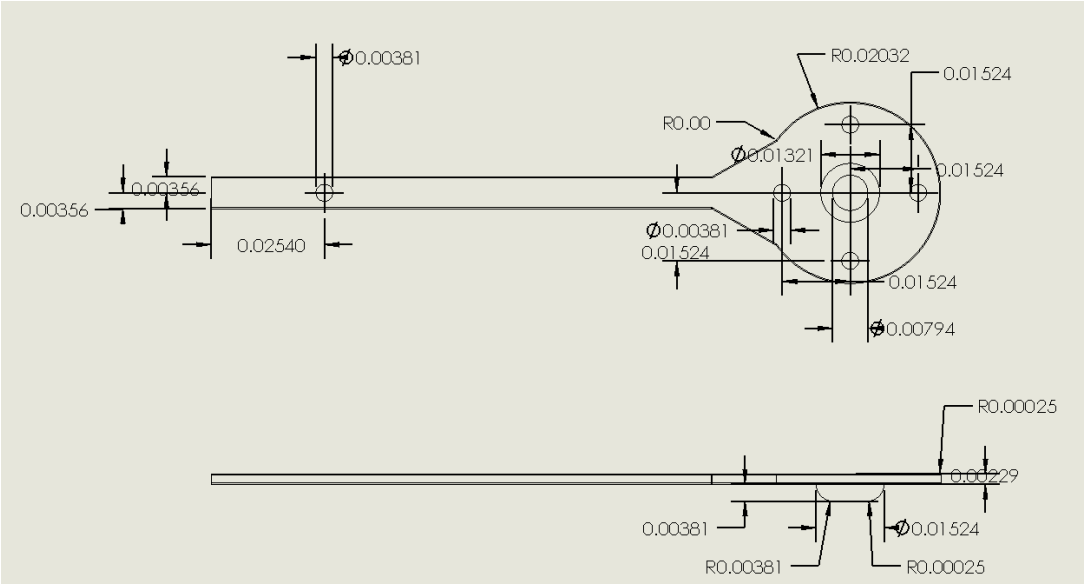

Figure 3.18: Bottom Slider Drawing

3.1.2.3.2 Top Slider

The top slider has the same dimensions as the bottom slider besides the part where the turbine is attached. It is kept as small as possible to provide the least possible disturbance to the airflow. It is the smallest possible fitting for the needed bearing to which the turbine is attached. The sliders very simple design is shown in Figure 3.19 to Figure 3.21. The drawing for the slider is shown in Figure 3.22. The small hole on the left of the slider, seen in Figure 3.19 and Figure 3.21 is needed to connect the slider with the support with bolts.

Figure 3.19: Top Slider Top View

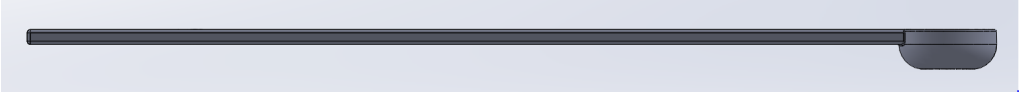

Figure 3.20: Top Slider Side View

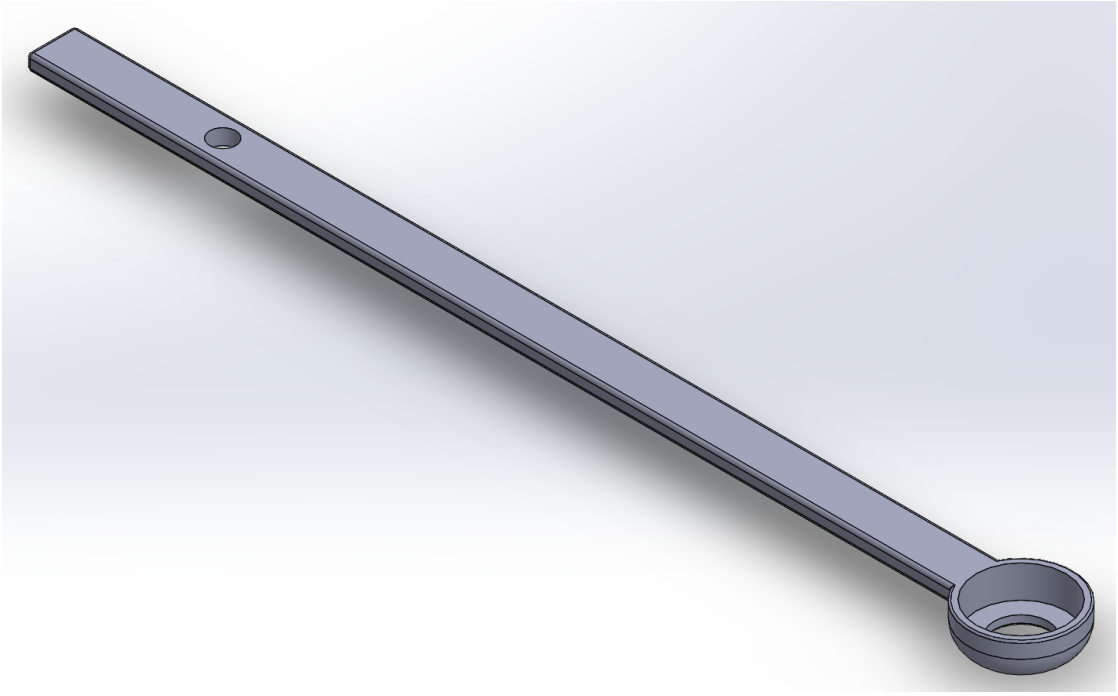

Figure 3.21: Top Slider Isometric View

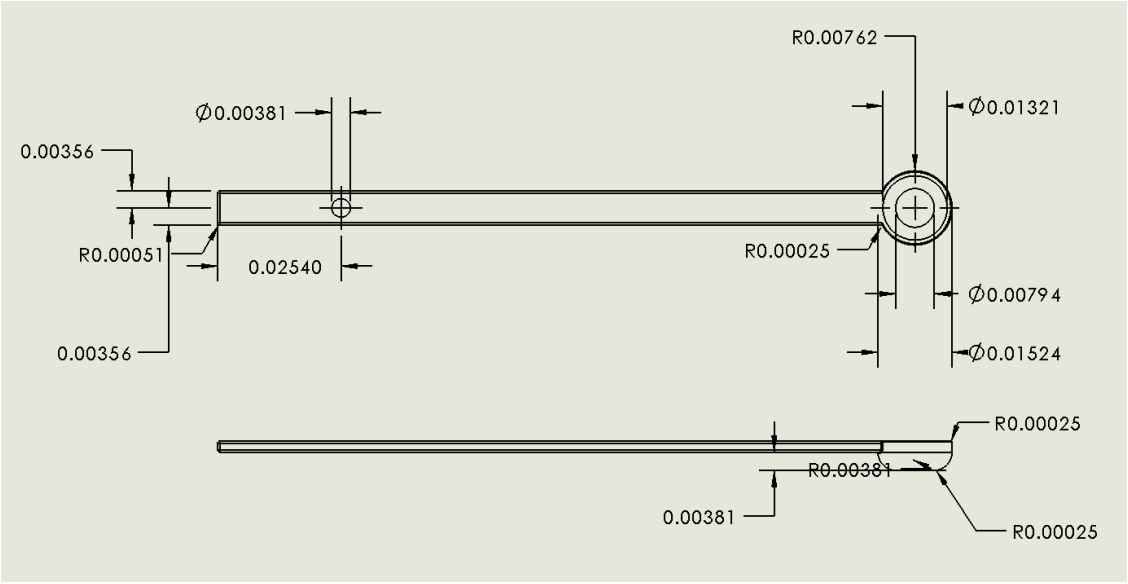

Figure 3.22: Top Slider Drawing

3.1.2.4 Turbines

After brainstorming, it was decided to progress with two different turbine designs. One Savonious Inspired Vertical Conical Turbine (SIVCT) and one NACA Profile Vertical Turbine (NPVT). These names have only been developed after the designs were finished and it was decided to move forward with these designs.

3.1.2.4.1 Earlier Turbine Designs

Figure 3.23 and Figure 3.24 show two designs that have been proposed but also have been disregarded later one. However, parts of those two designs have been considered when designing more turbines.

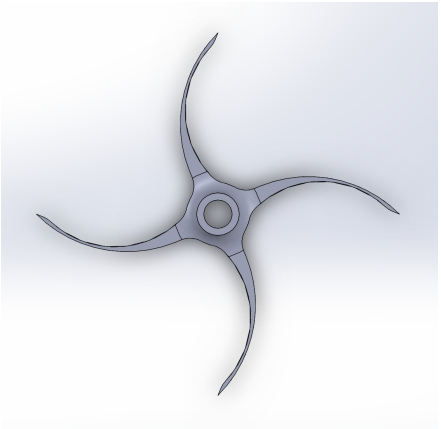

Figure 3.23: Old Turbine Design 1

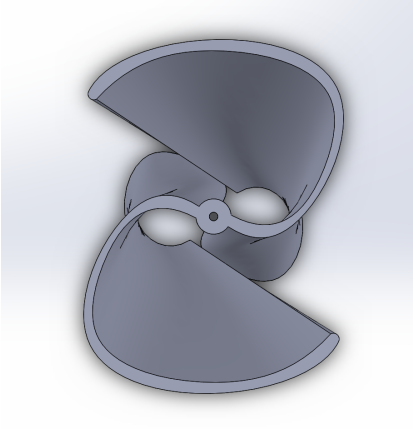

Figure 3.24: Old Turbine Design 2

3.1.2.4.2 Savonius Inspired Vertical Conical Turbine

The Savonius Inspired Vertical Conical Turbine (SIVCT) was designed with the objection of creating a pressure drop along the profile so the air would have a designated path to follow. Figures 3.25 to Figure 3.28 show the SIVCT. Its drawing in Figure 3.29 shows that the total turbine height is 13 cm but only 10 cm are covered by the two blades. In Figure 3.28 the hollow center of the turbine is seen. This is needed to install a support throughout the turbine to reduce vibration in the system and to make the turbine less fragile.

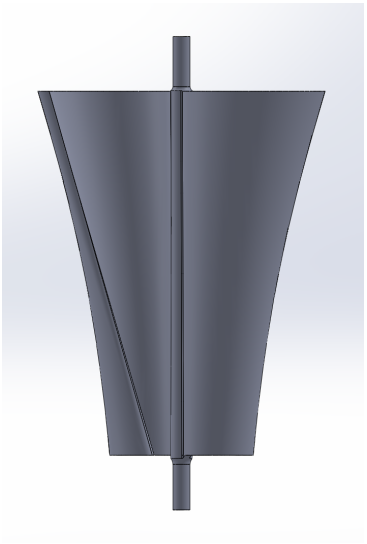

Figure 3.25: SIVCT Front View

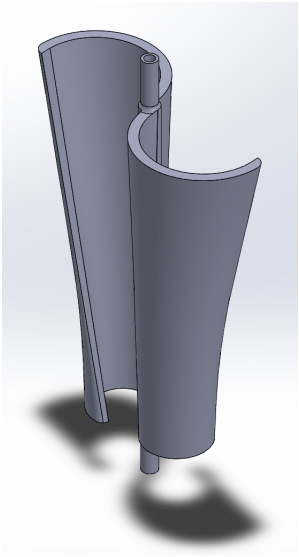

Figure 3.26: SIVCT Isometric View

The turbine is designed by using two symmetrical half circles at the top and two symmetrical 3/4 circle at the bottom that are mirrored twice, once around the x-axis

and once around the y-axis. Throughout the turbine perfectly round shaped edges are used and fillets are applied when necessary.

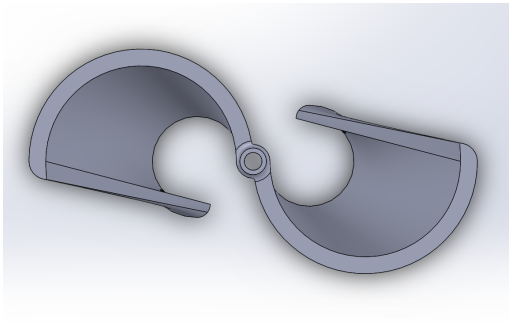

Figure 3.27: SIVCT Top View

Figure 3.28: SIVCT Bottom View

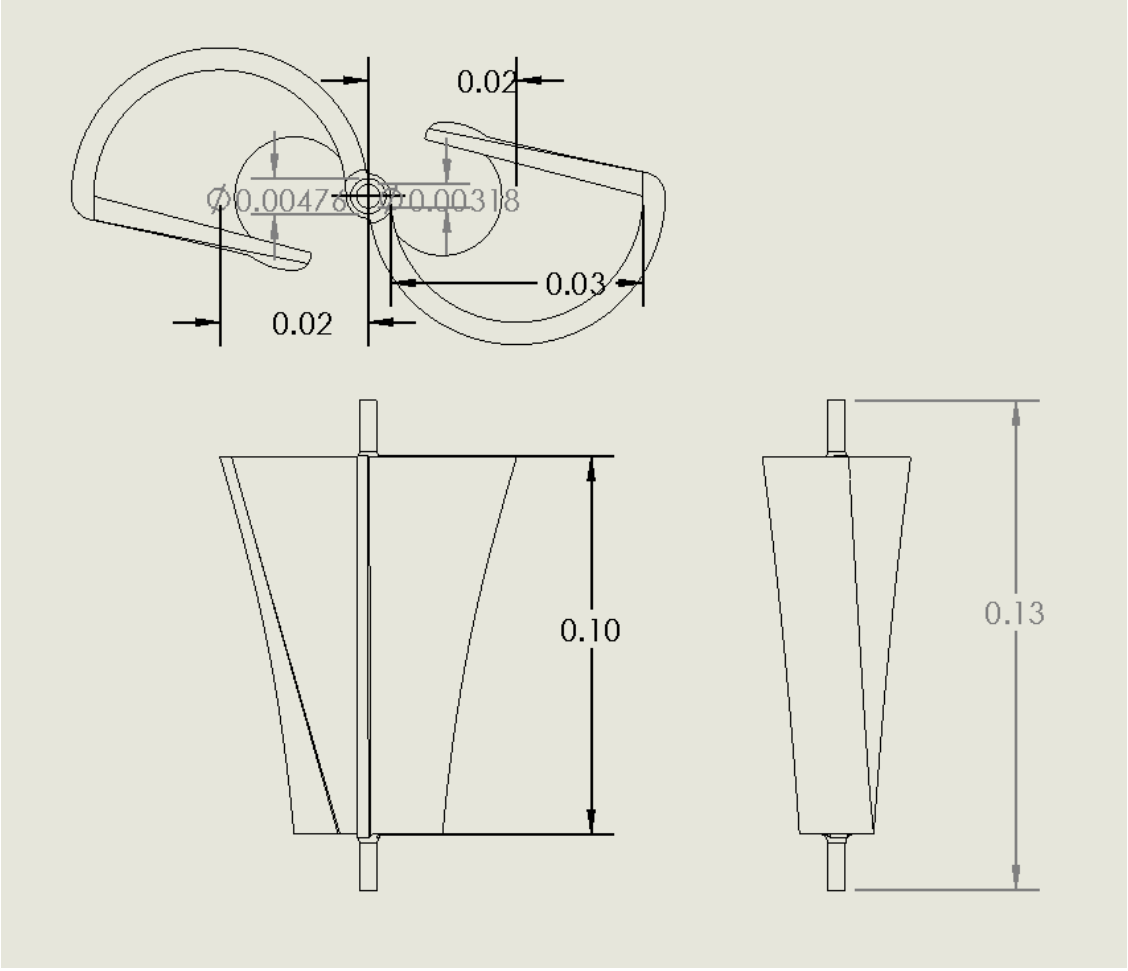

Figure 3.29: SIVCT Drawing

3.1.2.4.3 NACA Profile Vertical Turbine

The NACA Profile Vertical Turbine (NPVT) was designed using a NACA 9519 airfoil. It has a maximum thickness 10.1% at 28.1% chord and a maximum chamber of 8.8% at 50% chord. It has a total height of 13 cm, the blades cover 10 cm of

that. The turbine has a wingspan of 8cm where one blades is 4 cm long. As shown in Figure 3.33, the outer radius of the blade is 0.00476 cm and the inner radius of the blade is 0.00318 cm. Unfortunately, because of limited resources, it was not possible to to manufacture a turbine that looks closer to the Darrieus Wind Turbine. Especially the printability was of concerns because of the complexity of the designs.

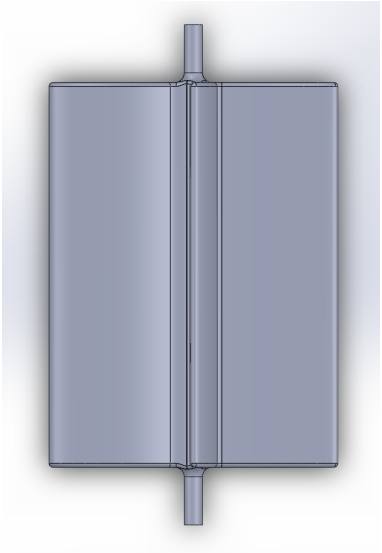

Figure 3.30: NPVT Front View

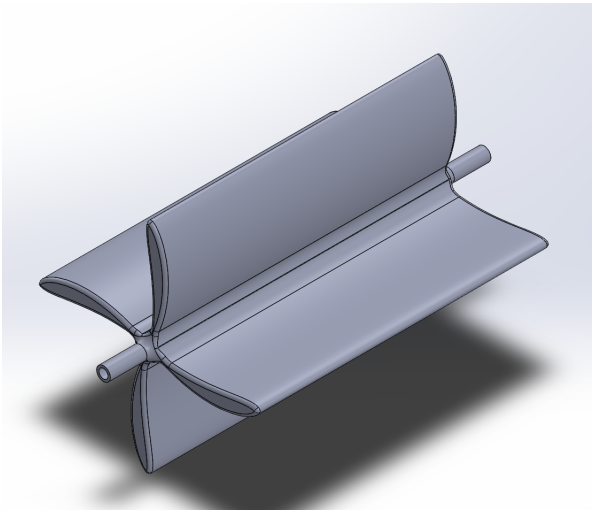

Figure 3.31: NPVT Isometric View

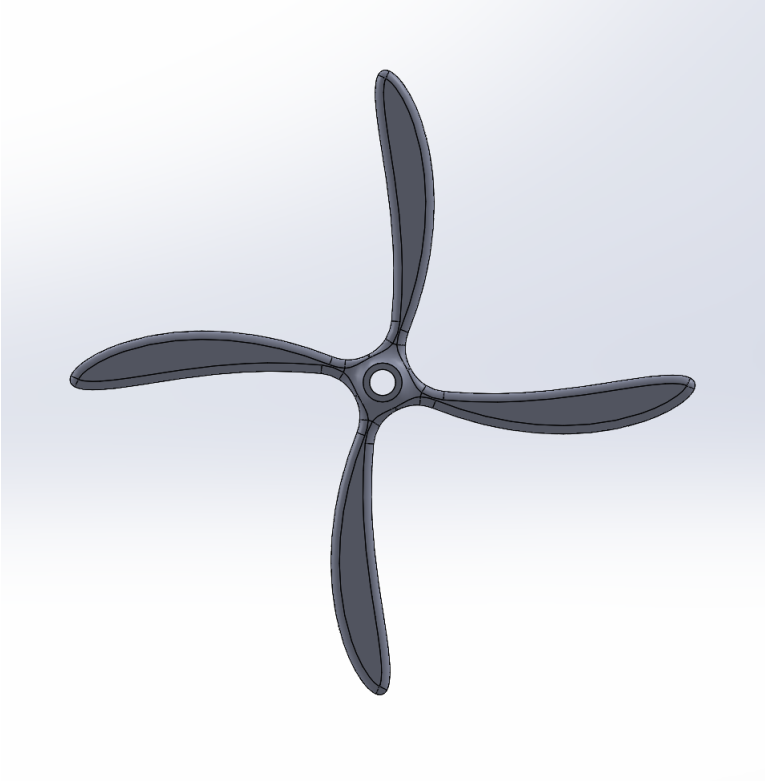

Figure 3.32: NPVT Top View

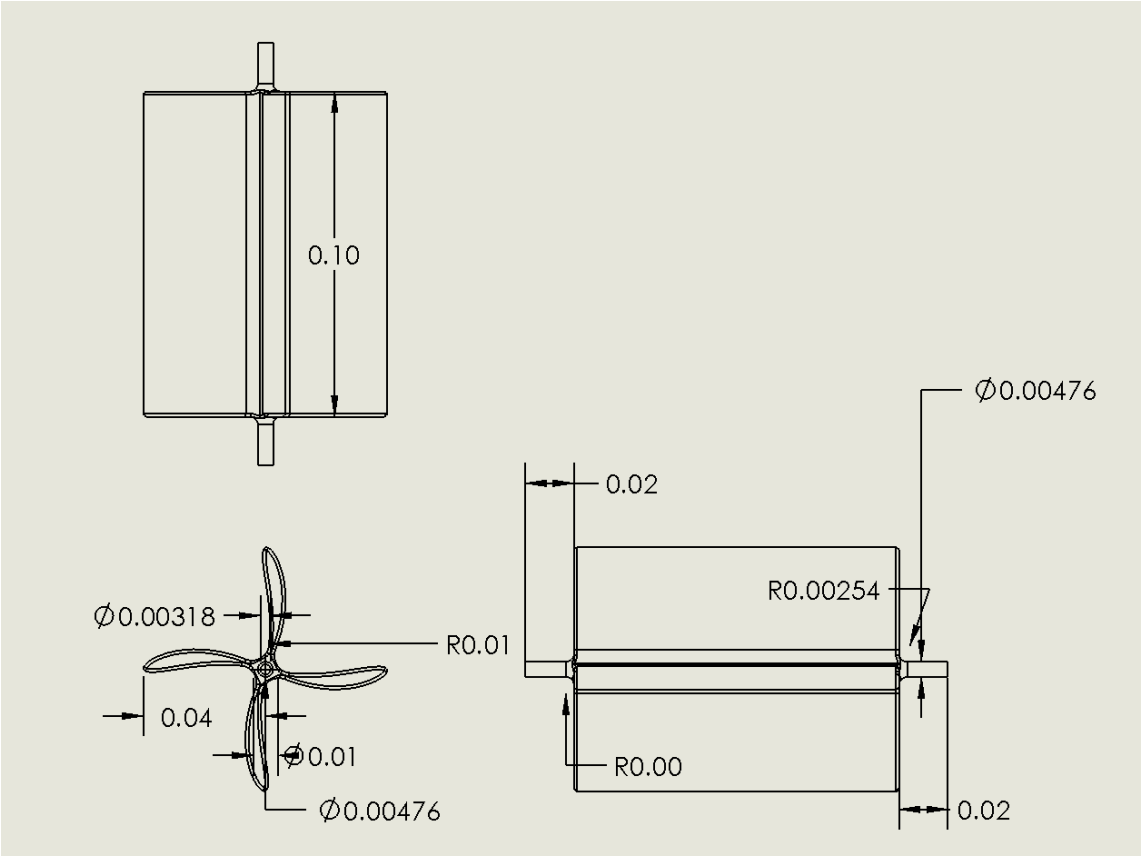

Figure 3.33: NPVT Drawing

3.1.2.5 Motorbox

The Motorbox provides housing for the electric generator. It has integrated cooling holes for the case of the generator generating a large amount of heat and possible material melting of the Motorbox. The small slot seen in Figure 3.36 is for the wires connecting the generator to the rest of the electric circuit. The holes on the top of the box are designed to fit perfectly below the holes in the bottom slider.

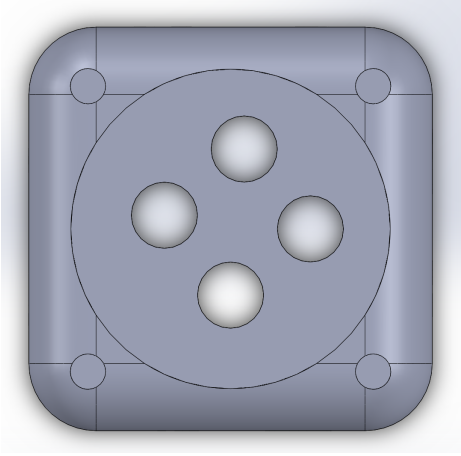

Figure 3.34: Motorbox Top View

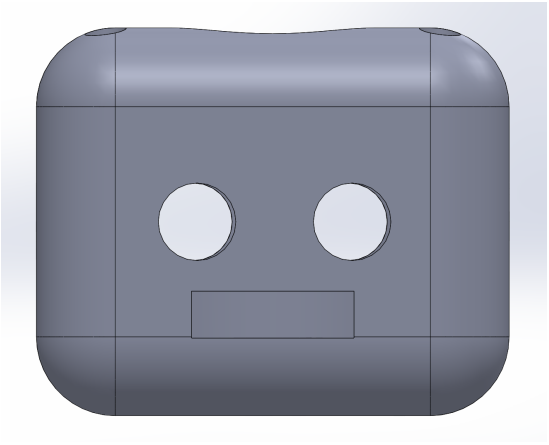

Figure 3.35: Motorbox Side View

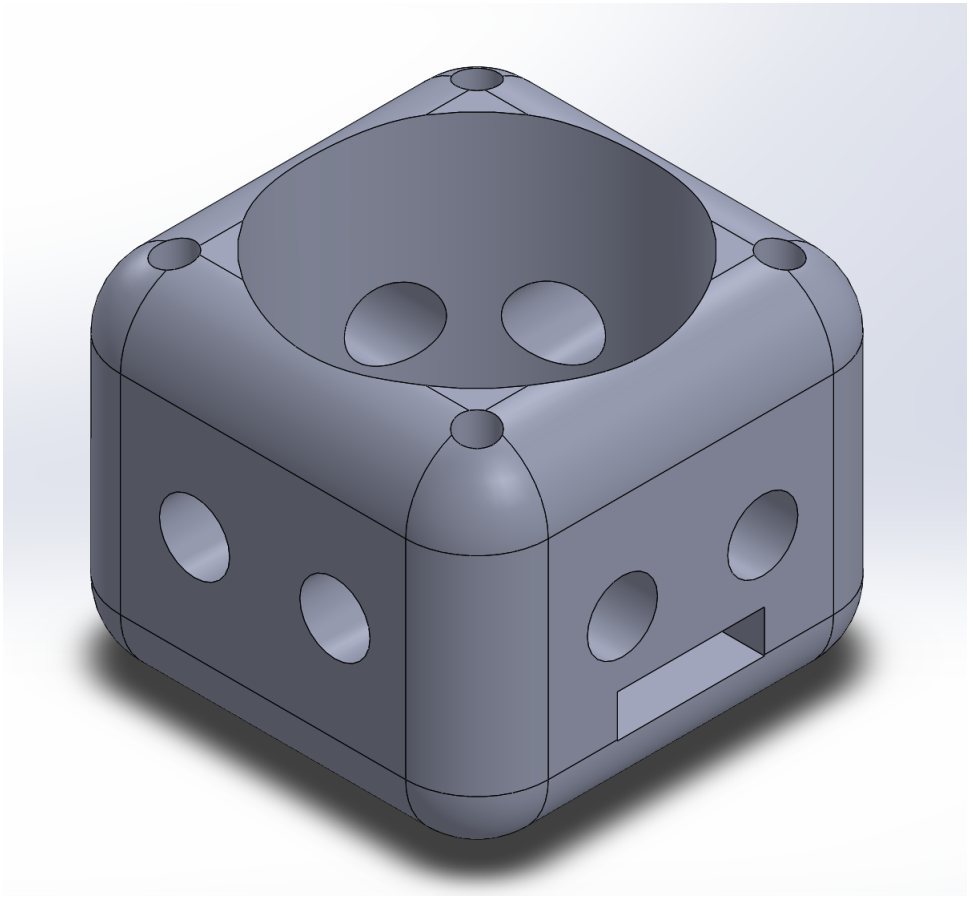

Figure 3.36: Motorbox Isometric View

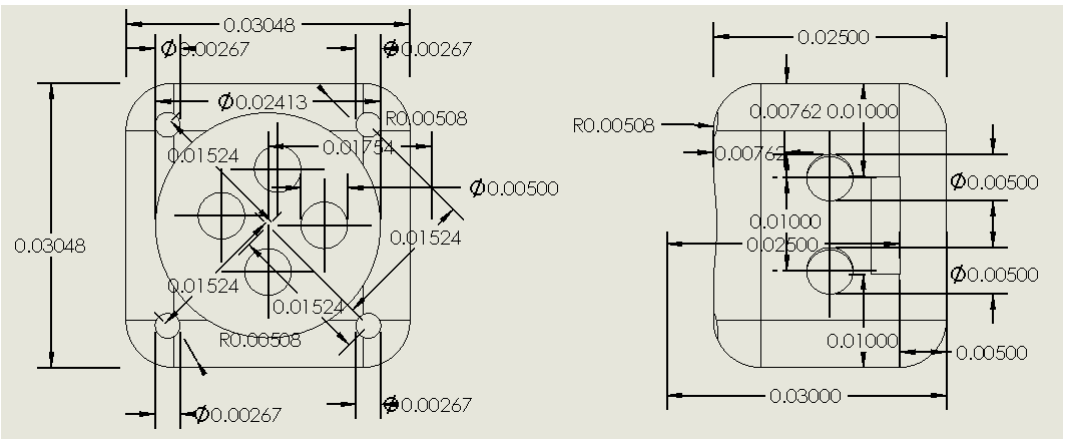

Figure 3.37: Motorbox Drawing Drawing

3.2 Manufacturing/Assembly Phase

To manufacture the obstacle, sliders, slots, and wind turbines, two different 3D printers were used. First, a LulzBot TAZ Workhorse 3D Printer was used to print

the parts of the obstacle. Secondly, a Formlabs Form 2 3D Printer was used to print the two parts of the slider and the wind turbines.

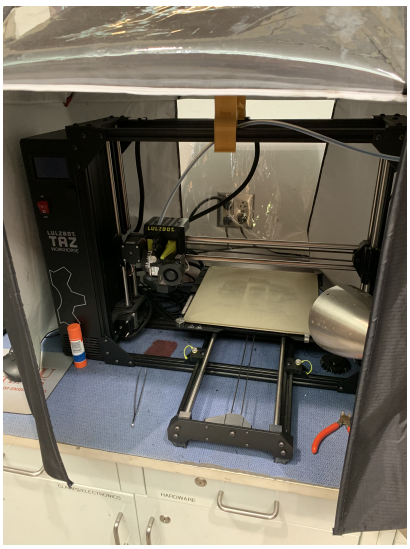

Figure 3.38: LulzBot TAZ Workhorse

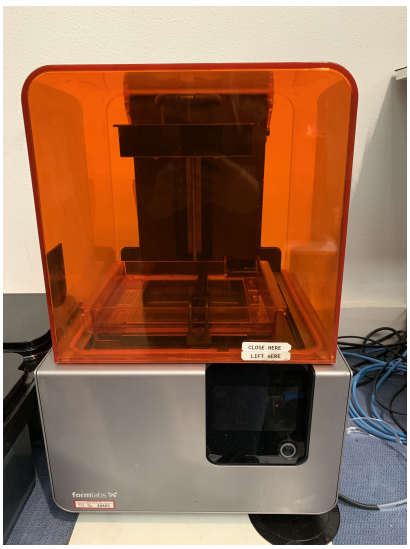

Figure 3.39: Formlabs Form 2

Once the obstacle pieces were printed, they were mounted onto a round plastic plate, with a diameter of 26 cm, using 3 1/4 in bolts fully threaded. Underneath the plate the bolts were supported by a aluminum plate to make the assembly as stable as possible.

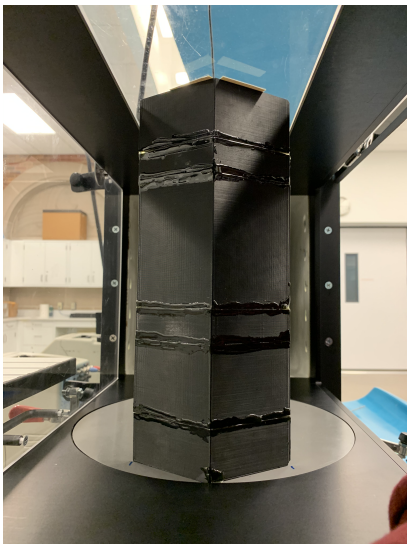

Figure 3.40: Assembled Obstacle

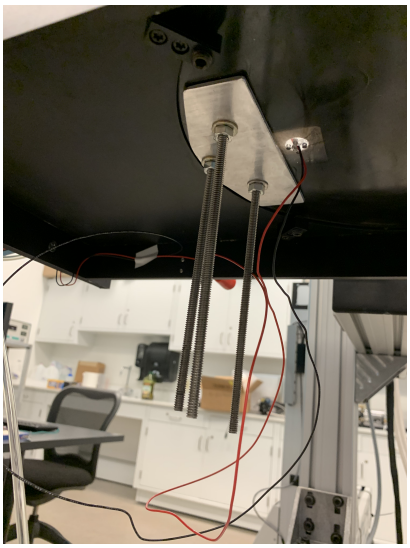

Figure 3.41: Obstacle Support

The supports are attached to the obstacle using bolts, washers, and nuts. And, again, the sliders are attached to the supports using also bolts, washers, and nuts. The hole going all the way through the turbine 'rod' has to be redrilled using an extended length 1/8 in drill bit. The 3D printer was not able to print the hole in the exact needed size. It is the housing for a steel rod providing more stability

and less vibration to the turbine itself and therefore also to the whole assembly. The rod used is a ground High-Strength 1045 Carbon Steel Rod with a 1/8 in diameter. Underneath the supports and sliders the same rods were attached to further reduce vibration in the system. The two sliders, bottom and top, have a housing for bearings. In this case, R3 open Ball Bearings for a 3/16 in shaft diameter were used and glued into the designated fittings in the sliders. The turbines now perfectly fit inside the bearings. The bearings provide a very smooth rotating cycle. Below the bottom slider, as mentioned earlier, the Motorbox is attached. To do so, the four holes on the Motorbox were tapped with a 6-32 tap drill bit to provide the perfect fitting for the 6-32 bolts. Those bolts have a length of 1 in. Additional nuts were used right below the bottom slider to prevent the bolts to come off and also to make the structure more stable.

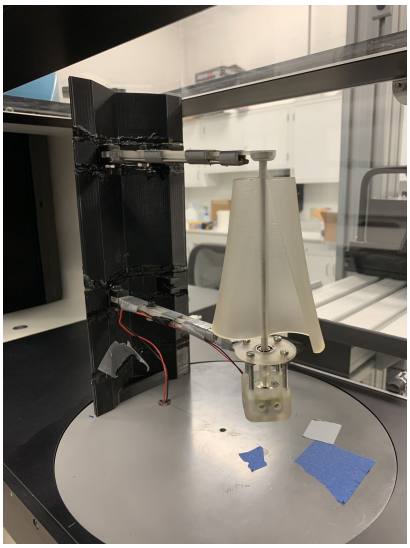

Figure 3.42: Attached SIVCT Turbine

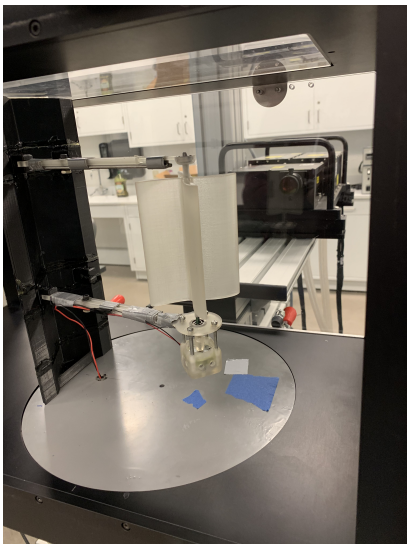

Figure 3.43: Attached NPVT Turbine

Additional pictures of the design, assembly, and parts in detail can be found in Appendix 1.

3.3 Test Phase

The phase is the final 'hands on' past of the project. For testing a closed loop Aerolab wind tunnel with a Twin City Fan & and Blower 15kW fan is used. This wind tunnel is locate in the Energy Systems Laboratory at Midwestern State University. It can be seen in Figure 3.45. The maximum wind speed that can be reached inside this wind tunnel is 90 mph. However, this limit will not be reached during the Test Phase. The speeds that are tested are significantly lower. The schematic of how the laboratory is set up can be seen in Figure 3.44 The Test Phase consisted of two steps. The Particle Image Velocimetry (PIV) and the Energy Generation Testing.

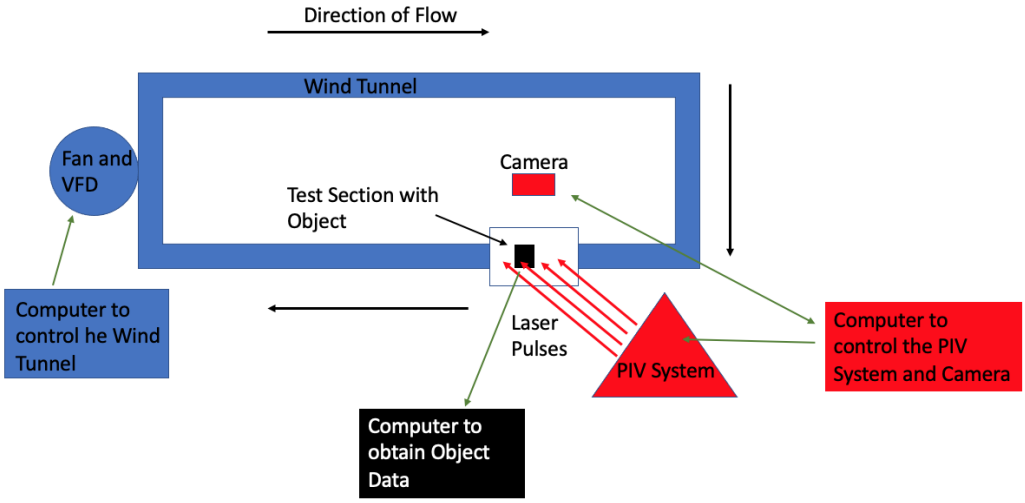

Figure 3.44: Wind Tunnel Schematics

Figure 3.45: Aerolab Wind Tunnel

Figure 3.46: PIV System

3.3.1 PIV Analysis

To perform the PIV Analysis, the TSI software Insight 4G is used. It is the latest version of the Global Imaging, Acquisition, Analysis and Display Software and the complete package for Fluid Mechanics research in PIV. [14] It uses a LaserPulse Synchronizer 610034 and a Canon MP Camera. The heart of the PIV System are the two Big Sky Laser Ultra systems, YAG120-BSL and YAG190-BSL. The PIV System can be seen in Figure 3.46. For the oil particle injection a Porter Cable 150 psi compressor is used. The compressor is connected to a cylinder which is filled with extra virgin olive oil. As the pressure in the cylinder builds up, the oil gets injected into the wind tunnel right before the last diffuser before reaching the test section. The injection system is shown in Figure 3.47 and Figure 3.48

Figure 3.47: Compressor

Figure 3.48: Oil Cylinder

During the PIV Analysis, the first goal was to confirm the designated vortex position established in the CFD Analysis. The analysis is done at several camera positions and wind speeds to confirm the results are conclusive. Significant tweaking is done inside the software and also on the oil particle injection. For all runs, the laser intensity is set on 'high' for both laser pulses. The Gaussian Peak differs from run to run to obtain the best possible velocity vectors. In most cases a Gaussian Peak of 1.5 was used. To successful display the wanted velocity vectors and vortices, the camera has to take pictures from the top, hanging above the test section. The Big Sky Laser shoots its laser pulses horizontally from the side to ideally form a 'laser sheet' that goes through the whole test section. The results of the PIV Analysis are presented in the Results Chapter.

3.3.2 Energy Generation Testing

For generating energy, a Topoox DC 3V 1730RPM Mini Electric Generator is used. It is connected to a LabView program with a basic circuit including a small 592Ω resistor. The LabView program is shown in Figure 3.49.

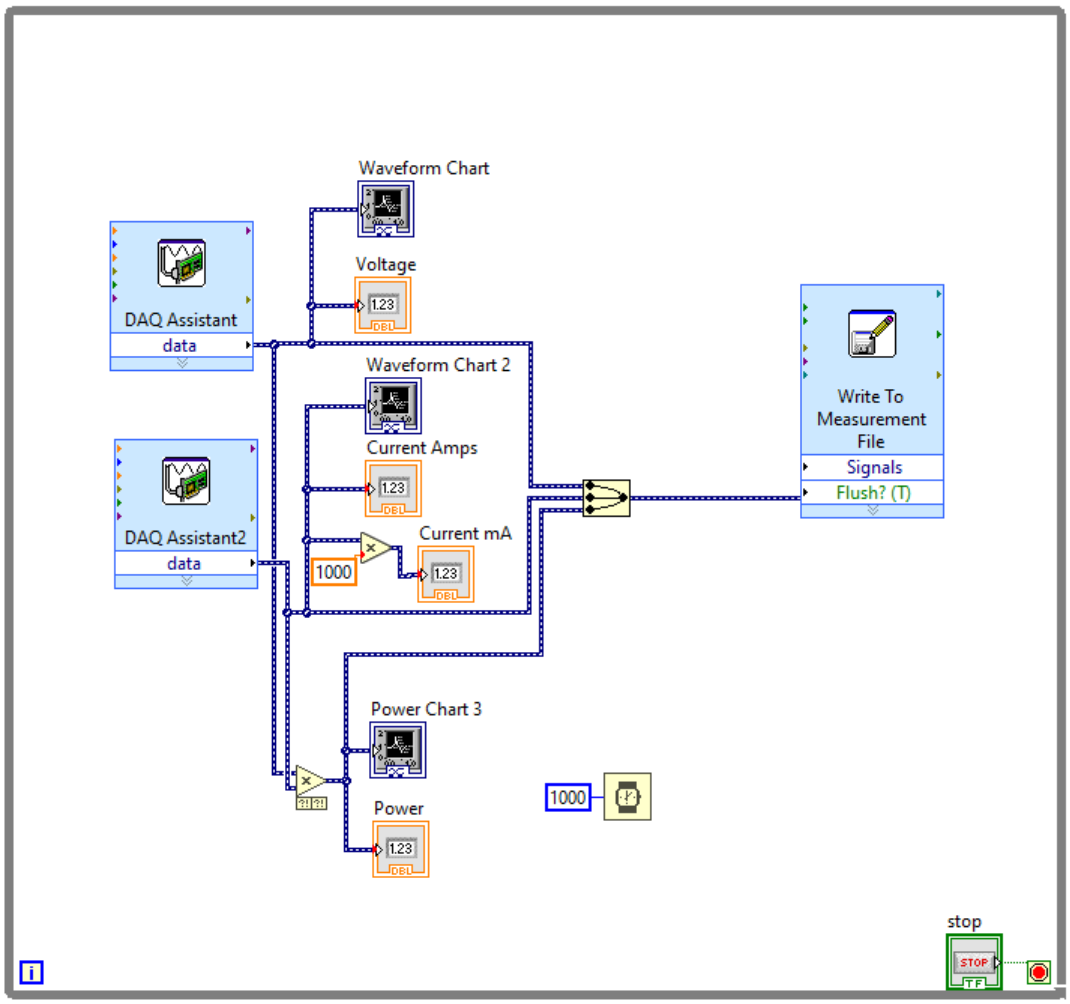

Figure 3.49: LabView Program

As seen, the LabView Program reads the voltage and current from the generator and calculates the power using the following equation.

$$P = V * I \tag{3.1}$$

where

$$P = Power\ [W]$$

$$V = Voltage\ [V]$$

$$I = Current\ [mA]$$

The output can be displayed in form of a graph and also plain numbers. During this phase, both turbine models are tested in the wind tunnel at different wind speeds and different positions. The positions are specified in Figure 3.50. Position 2 is at the designated vortex position obtained from the CFD Analysis. The radius that can be seen interjects that position and has its origin at the mount on the obstacle. Position 1 is outside of the region of the obstacle and the only flow that interferes with the turbine located in that position is the by flow. Position 3 is centrally

located behind the obstacle, technically in between the two vortices forming behind the obstacle.

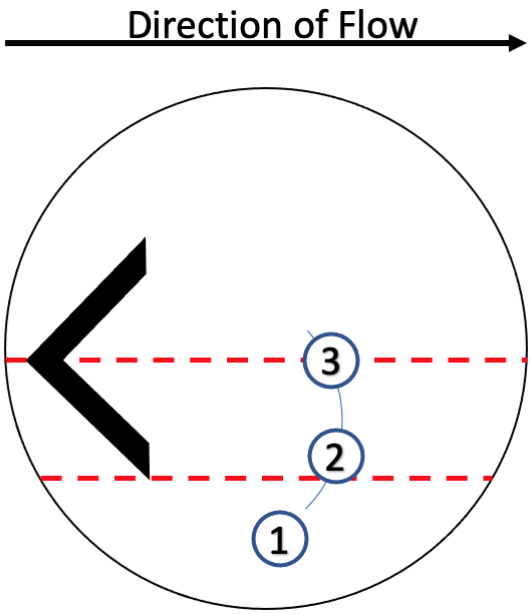

Figure 3.50: Testing Positions

Beforehand, the speed of the turbines is measured using a Monarch Instruments PLT200 tachometer. To do so, a small strip of reflector tape is stuck onto each of the turbines. The results of the Energy Generation Testing are presented in the Results Chapter. During this step, the electric generator is not attached to the turbines so the measured speed will be slightly higher than in the step when the energy generation is tested. The generator and circuit with the resistor have a certain resistance that also has to be overcome by the wind.

4
Results

4.1 CFD Results

The results of the CFD Analysis is presented in this section. First, the optimum shape of the obstacle was determined by trying different designs ob obstacle shapes. Then, the optimum shape is tried at different wind speeds, to be specific 10 m/s and 5 m/s, to check if the results are conclusive. As seen in Figure 4.1 and Figure 4.2 the vortices behind the second and third obstacle are not symmetrical. They are shifted. The same occurs for both at 5 m/s and at 10 m/s. Figure 4.1 shows the flow for 5 m/s and Figure 4.2 shows the flow for 10 m/s. Since the wind speed is varied during the experiment, those obstacles would also not be suited if they displayed symmetrical vortices at one of the 2 simulated speeds.

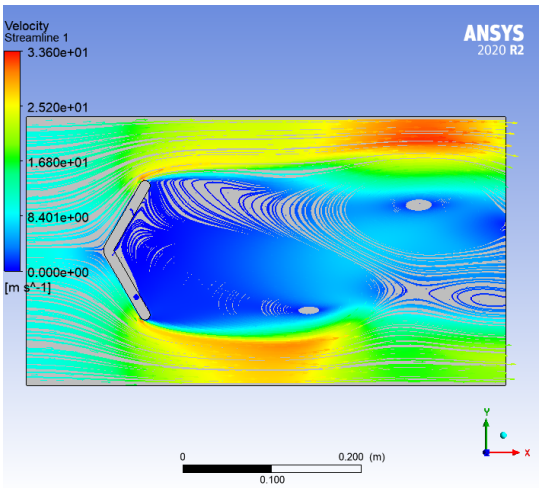

Figure 4.1: Vortices behind Obstacle 2

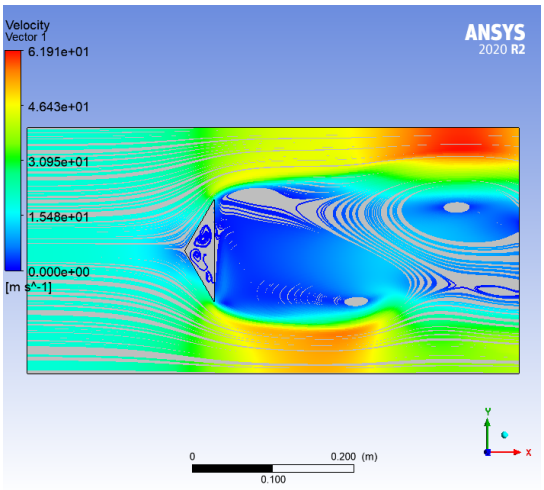

Figure 4.2: Vortices behind Obstacle 3

When simulating obstacle 1, the results look certainly different than for obstacle 2 and 3. The velocity streamlines for the obstacle 1 simulations for 5 m/s and 10 m/s are shown in Figure 4.3 and Figure 4.4 respectively. It can be seen, the vortices are almost identically forming behind the edges of the obstacle. The higher wind velocity in Figure 4.4 results in vortices that are located a little further away from the obstacle compared to the ones shown in Figure 4.3. Also, the 'eye' of the vortices are smaller and more compact. Based on these findings, it was decided to use obstacle 1 when designing the obstacle used in the experiment. Since the displayed section is exactly the dimensions of the test section of the wind tunnel used, the designated

vortex position can be determined using those simulations. Table 4.1 displays the x distances of the vortex eyes from the obstacle for the two simulated wind speeds.

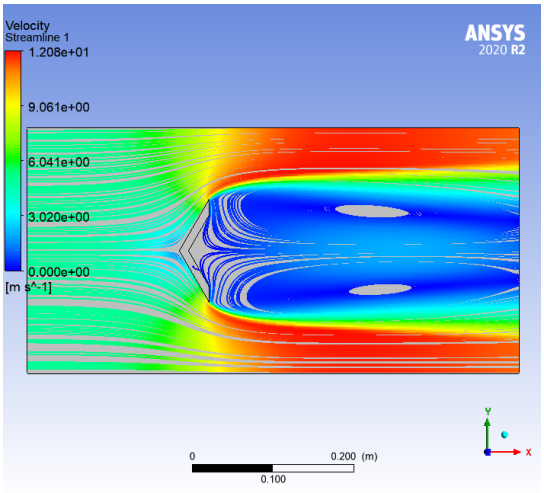

Figure 4.3: Vortex Shedding Series 1a

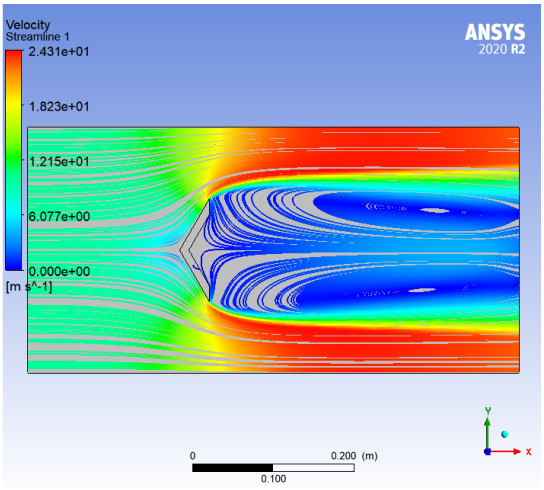

Figure 4.4: Vortex Shedding Series 1b

Table 4.1: Vortex X Distance from Obstacle for Different Wind Speeds

Wind Speed [m/s]	Vortex X Distance from Obstacle [cm]
5	18-20
10	25

4.2 PIV Results

The results of the PIV Analysis are shown in this section. First, the vortex was made visible. During the analysis, new findings have come up. Which led to another subsection in this section.

4.2.1 Visible Vortex

4.2.1.1 Visible Vortex without Turbine over Multiple Layers

To check if the creation of vortices is consistent throughout the system, multiple PIV pictures are taken at several heights of the test section. For the top height picture the laser sheet is above the turbine placement, for the middle height picture, the laser sheet is in the turbine area, and for the bottom height picture, the laser sheet lays below the turbine. Figures 4.5, 4.6, and 4.7 show three vortices in similar positions but different heights in the system. X pixel and Y pixel determine the distance from the origin. This has been done at 5 m/s and 10 m/s. 5 m/s corresponds to 11 mph and 10 m/s corresponds to 22 mph. In the future, when talking about wind speeds, the speed is in the unit mph. Clearly, it can be said, the system is continuous throughout all heights of the system.

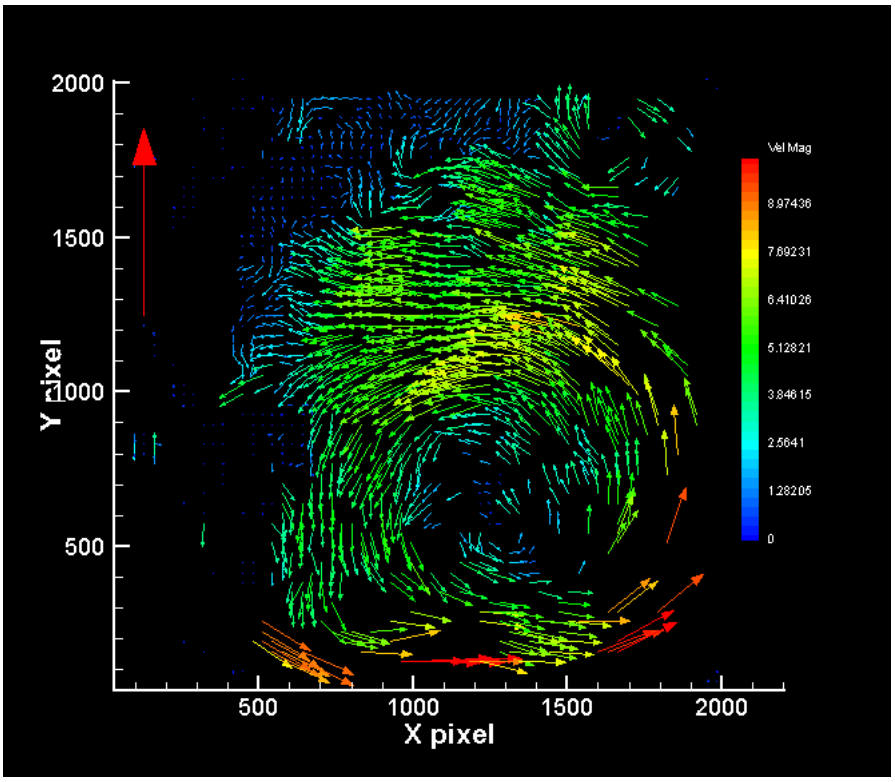

Figure 4.5: Vortex at the Top Height of the System

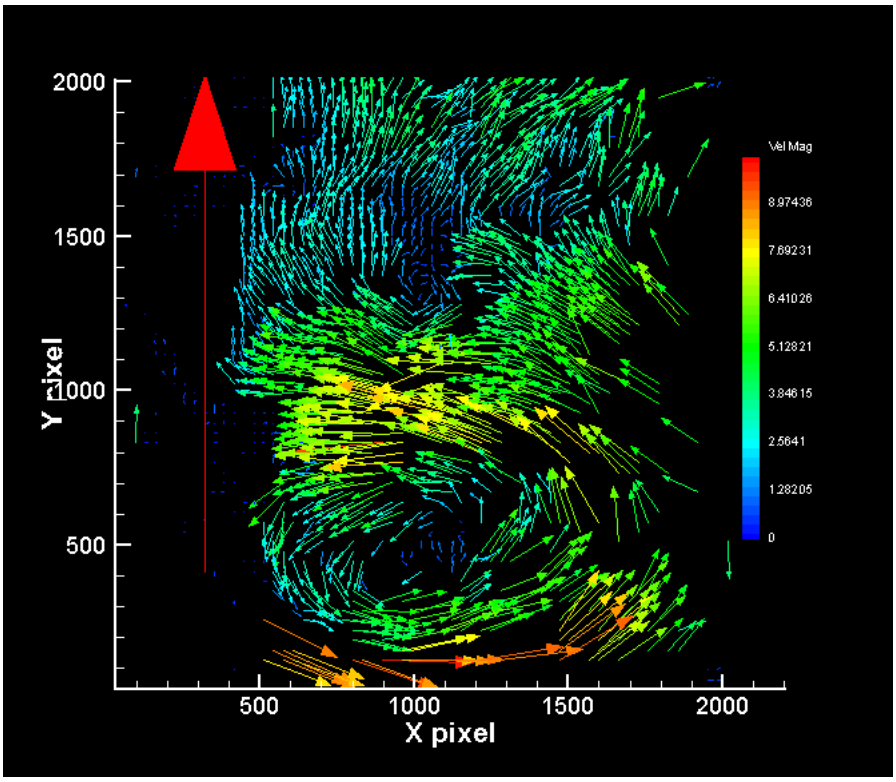

Figure 4.6: Vortex at the Middle Height of the System

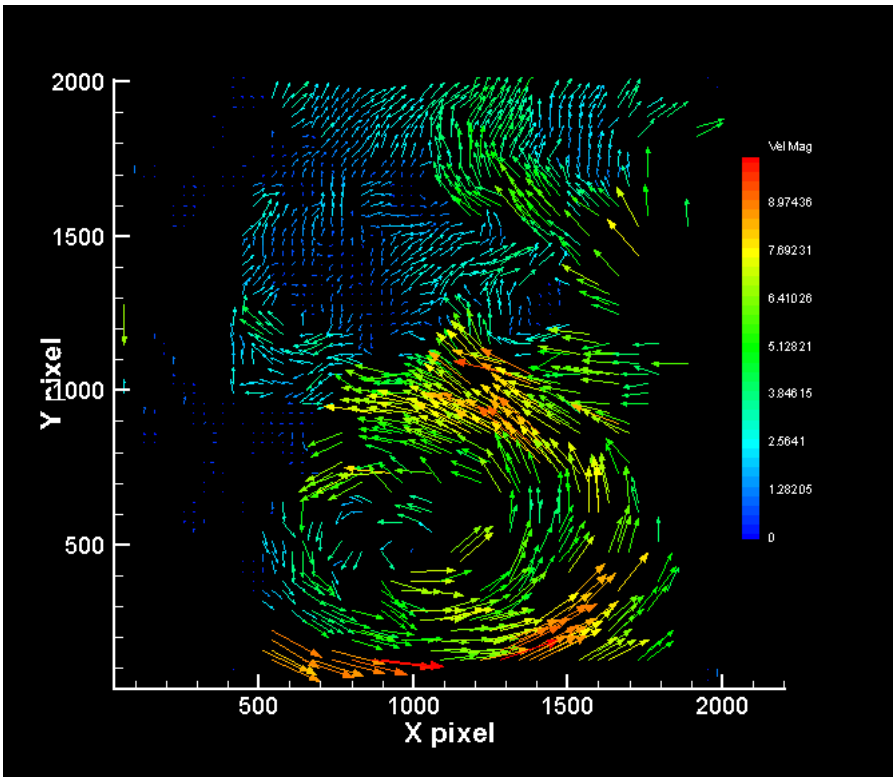

Figure 4.7: Vortex at the Bottom Height of the System

4.2.1.2 Visible Vortex with Turbine

The next goal was to establish a well visible picture of a vortex in the designated position with the turbine in the system. The designated position was determined in the CFD Analysis. Figure 4.8 and Figure 4.9 show well visible vortices. To be specific, Figure 4.8 shows a vortex that is rotating counterclockwise with the turbine visible and Figure 4.9 shows a vortex rotating clockwise with the turbine visible as well. The turbines are circled in red. The flow direction in the pictures is left to right. If looking at the pictures from a top view, the left edge is close to the inlet and the right edge is close to the outlet. This is continuous throughout all future PIV Analysis pictures. The counterclockwise vortex is generated by flow passing the obstacle on the right side, the clockwise vortex is generated by flow passing the obstacle on the left side.

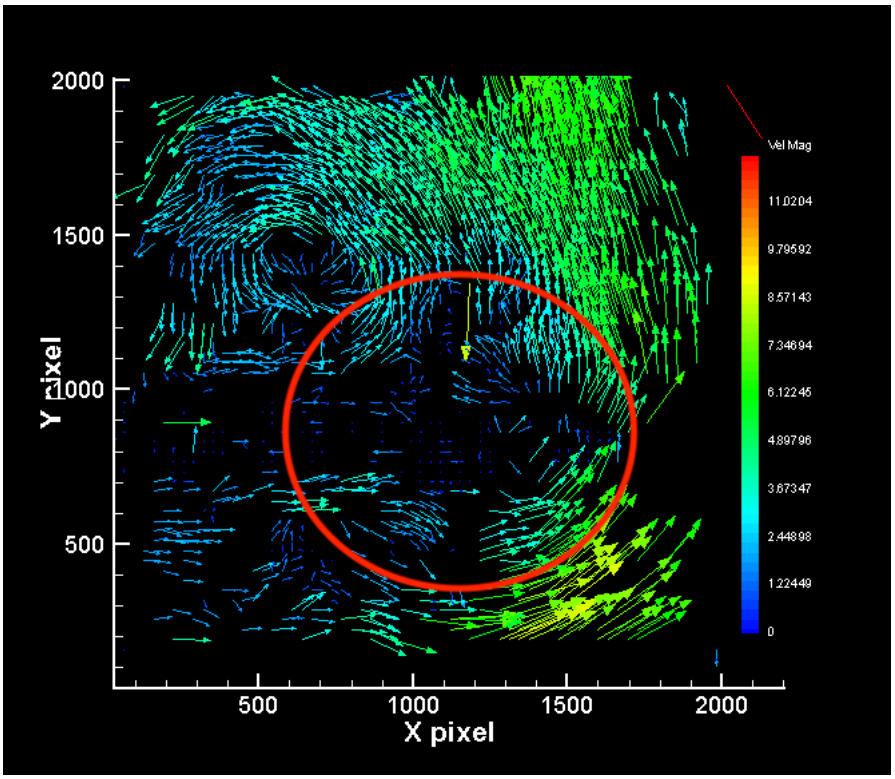

Figure 4.8: Counterclockwise Vortex

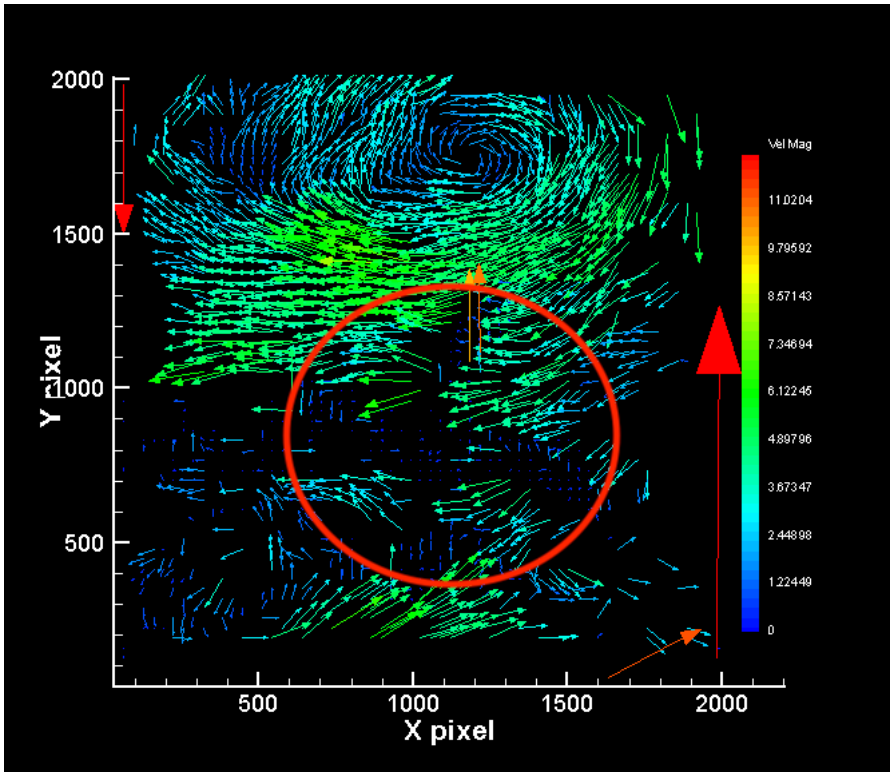

Figure 4.9: Clockwise Vortex

4.2.2 Vertex Shedding

Both of the above show vertices in Figures 4.8 and 4.9 are located in almost the same location. This indicates a 'Vertex Shedding'. Bengt Sunden describes vortex shedding as a major importance in engineering design because the alternate formation and shedding of vortices also creates alternating forces, which occur more frequently as the velocity of the flow increases. [11] The full example series of vortex shedding is shown in Figure 4.10 to Figure 4.17. The shown series is recorded at a wind speed of 11 mph which is approximately 5 m/s. It is clearly seen that the vortices are shedding. The time instance t1 is previous is time compared to t2, therefore $t1 < t2$.

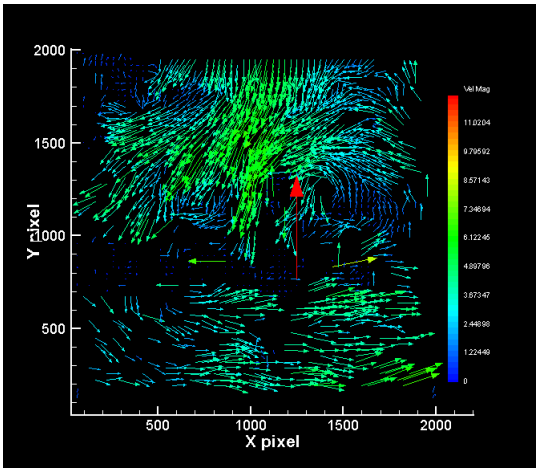

Figure 4.10: Vortex Shedding Series 1 at t1

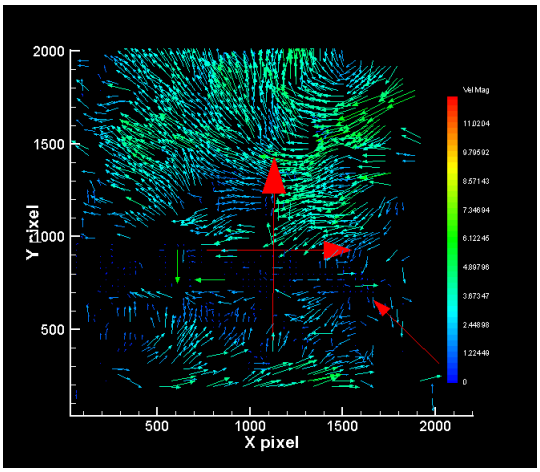

Figure 4.11: Vortex Shedding Series 1 at t2

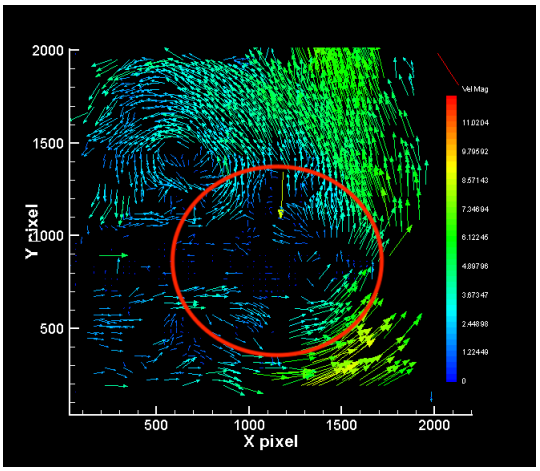

Figure 4.12: Vortex Shedding Series 1 at t3

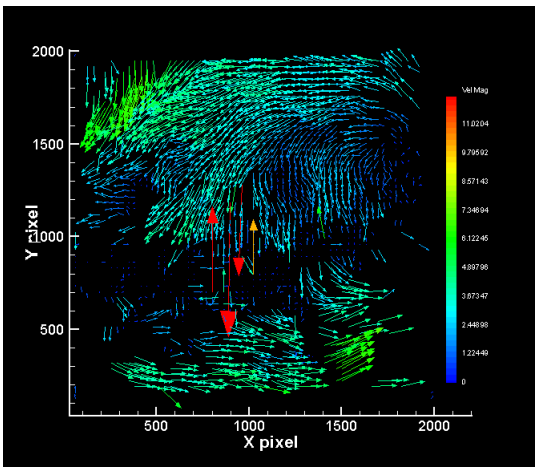

Figure 4.13: Vortex Shedding Series 1 at t4

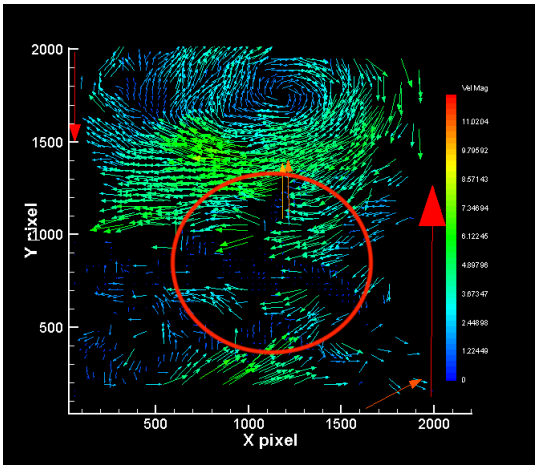

Figure 4.14: Vortex Shedding Series 1 at t5

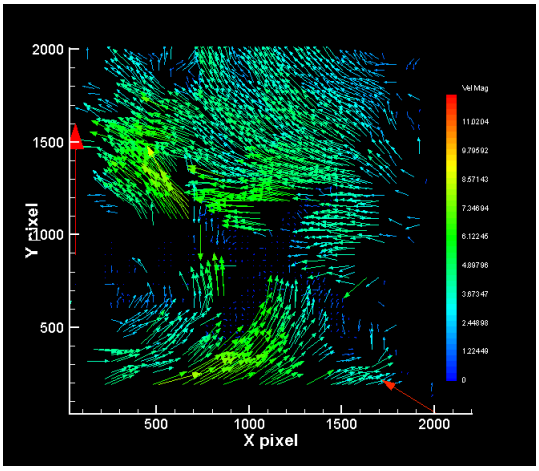

Figure 4.15: Vortex Shedding Series 1 at t6

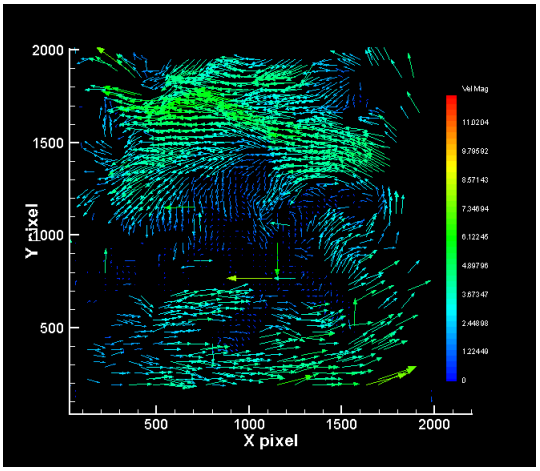

Figure 4.16: Vortex Shedding Series 1 at t7

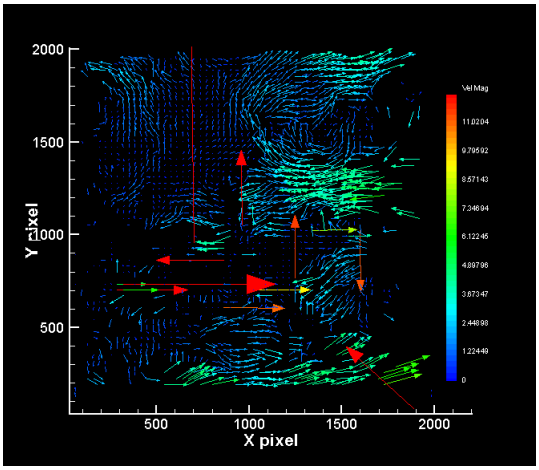

Figure 4.17: Vortex Shedding Series 1 at t8

There were found several examples of vortex shedding, not just at 5 m/s, but also at approximately 2.5 m/s. This series is shown in Figure 4.18 to Figure 4.27. In this case it is not as clearly shown as before but it is still very strong evidence that suggests vortex shedding at lower speeds. Between Figure 4.21, which does not show a vortex but a obvious direction of flow, and the clearly shown vortex in Figure 4.23, an evident change of direction is shown. Additional series of vortex shedding can be found in Appendix A.

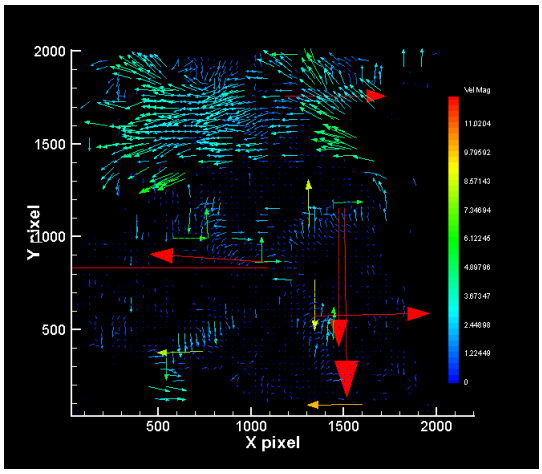

Figure 4.18: Vortex Shedding Series 2 at t1

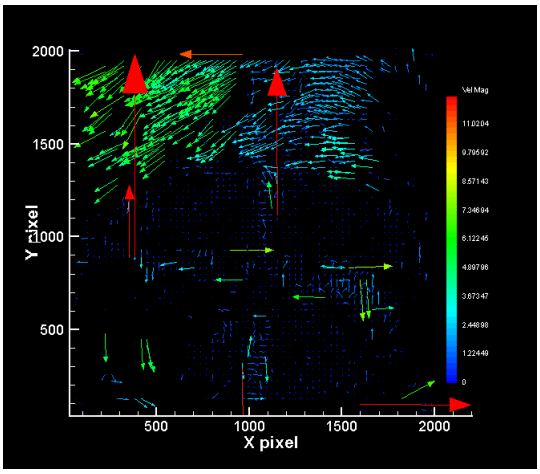

Figure 4.19: Vortex Shedding Series 2 at t2

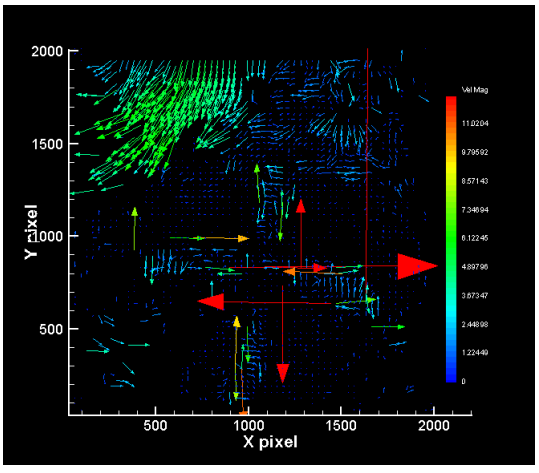

Figure 4.20: Vortex Shedding Series 2 at t3

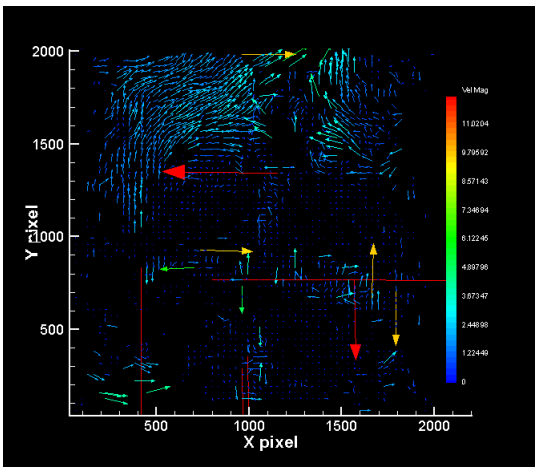

Figure 4.21: Vortex Shedding Series 2 at t4

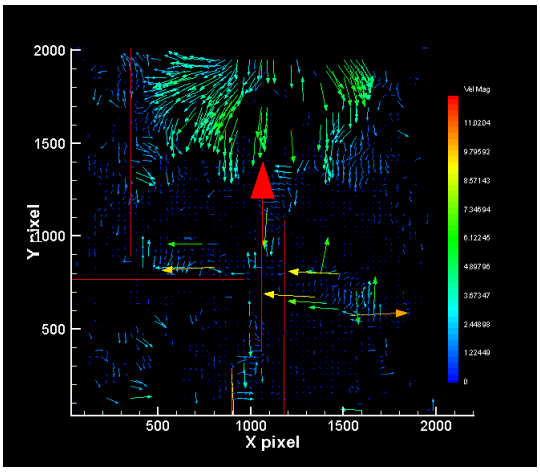

Figure 4.22: Vortex Shedding Series 2 at t5

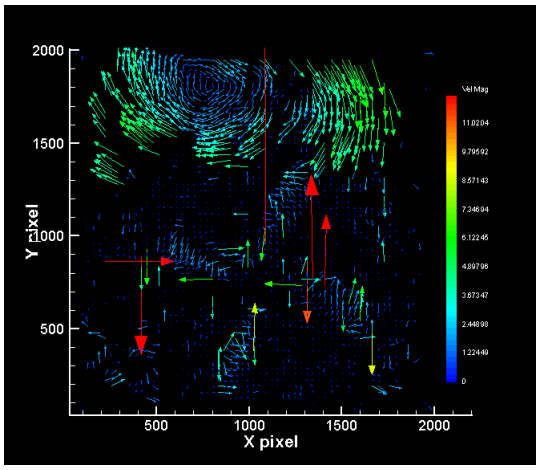

Figure 4.23: Vortex Shedding Series 2 at t6

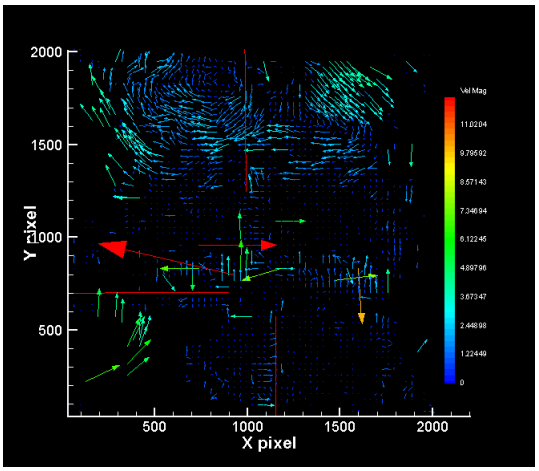

Figure 4.24: Vortex Shedding Series 2 at t7

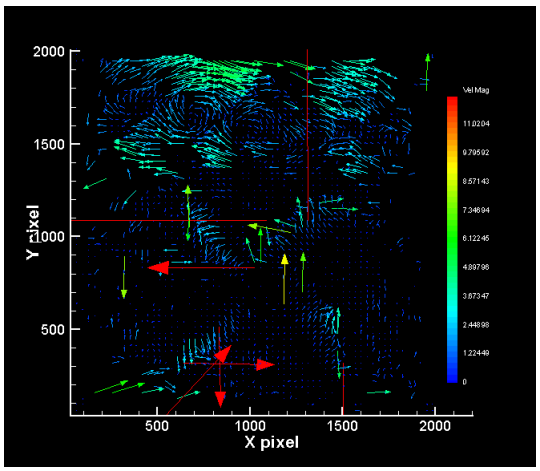

Figure 4.25: Vortex Shedding Series 2 at t8

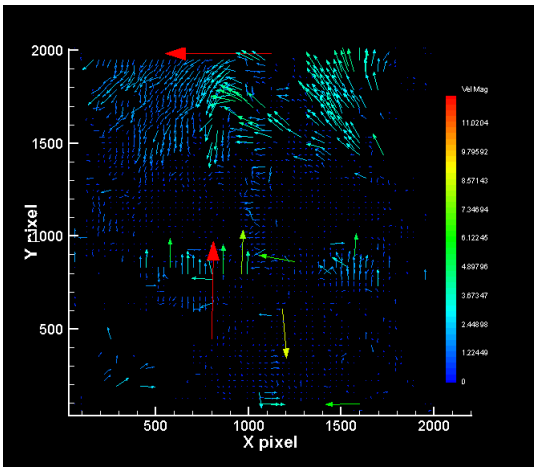

Figure 4.26: Vortex Shedding Series 2 at t9

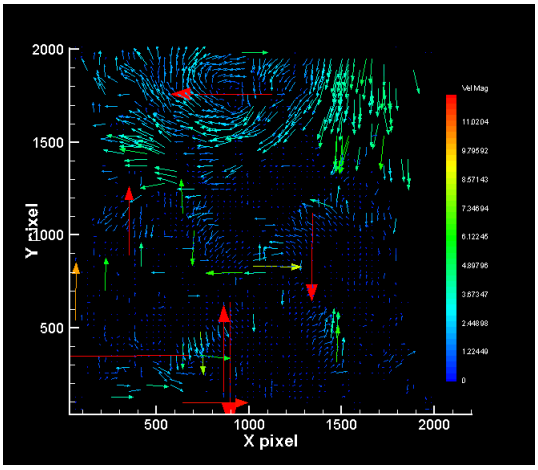

Figure 4.27: Vortex Shedding Series 2 at t10

4.2.2.1 Why are the vortices shedding?

When observing these kinds of flow behavior, the question 'Why are the vortices shedding?' is asked. A study from Xing Zhang and Blair Perot states that there occurs vortex shedding behind a triangular cylinder at a Reynolds Number of Re=45000. This suggests that The Reynolds Number in this specif systems is also relatively high and probably close to Re=45000. The Reynolds Number is calculated as follows.

$$Re = \frac{uL}{v}, \tag{4.1}$$

where:

$$u = velocity\,of\,the\,fluid\,[m/s]$$

$$L = characteristic\,length\,of\,an\,airfoil\,[m]$$

$$v = kinematic\,viscosity\,of\,the\,fluid\,[m^2/s]$$

In this case the we have 2 velocities, 10 m/s and 5 m/s. The characteristic length of the airfoil, in our case the obstacle width is 12 cm or 0.12 m. The kinematic viscosity of air at a temperature of 20 °C is $1.516 * 10^{-5} m^2/s$. The calculated Reynolds numbers for the two cases are presented in Table 4.2

Table 4.2: Reynolds Number for different Wind Speeds

Wind Speed	Reynolds Number
10 [m/s]	79155.67
5 [m/s]	39577.84

It is observed that the Reynolds Number for both cases, 10 m/s and 5 m/s, is relatively high. In the case of 10 m/s even higher than the studied case from Zhang and

Perot. Earlier, it was stated, the ideal Reynolds Number for symmetrical vortices to appear is Re=20.8. Clearly, the Reynolds Number in the studied cases appears to be significantly higher. This can be part of the reason why the vortices are shedding. The mentioned flow from Zhang and Perot clearly lies in the laminar flow regime region. A study from Sercan et. al. suggests that there is also perfect vortex forming at higher Reynolds Numbers. This would be in the highly turbulent flow regime region. [15] Therefore, another possible reason is, the flow studied in this thesis lays in the the region in between the laminar and turbulent regions.

4.3 Energy Generation

The last step in this study was to test for energy generation. More specially, this means how the generated energy varies with different wind speeds, different turbine positions, and different wind turbines. Therefore this section is divided into two subsections which both focus on one wind turbine type.

4.3.1 Energy Generation SIVCT

First, the turbine speeds are studied. Table 4.3 and Table 4.4 show the recorded turbine speeds in rpm for the SIVCT. It can be seen, the turbine has difficulties rotating at low speeds. It does not start spinning until the wind speed inside the wind tunnel reaches 18 mph. As seen, it spins faster in position 1. For position 2 the turbine spins with 700 rpm compared to the 800 measured in position 1. Once the turbine starts spinning, the speed increases gradually with the increase of wind speed for both turbines. It can also be seen, that the maximum speed at 22 mph is higher at position 1 than it is at position 2. There is a tremendous difference from 20 mph to 21 mph. the wind turbine speed is almost twice as much as before. It has to be noted, all speeds are averages over a longer time span.

Table 4.3: SIVCT Average Speed at Position 1

Wind Speed [mph]	**Turbine Speed [rpm]**
18	800
19	900
20	1100
21	2000
22	2300

Table 4.4: SIVCT Average Speed at Position 2

Wind Speed [mph]	**Turbine Speed [rpm]**
18	700
19	900
20	1000
21	1200
22	1300

The next Figures, Figure 4.28 to Figure 4.37 show the Voltage, Current, and Power generated with the SIVCT at speeds ranging from 18 mph to 22 mph in Position 1 and Position 2. Those plots represent the same findings seen in Table 4.3 and Table 4.4. More power gets generated with higher wind speed. From Figure 4.29 to 4.30, which represent the data collected at 19 mph and 20 mph, it looks like less power gets generated. But if observed closely, the mean power production is higher for 20 mph with 0.0049 W compared to 0.0046 W at 19 mph over the same time span. This data can be found in Figure 4.5 Even though, the big jump in wind turbine speed from 20 mph to 21 mph wind speed is not as severely seen in the mean data, there is still a jump. This can be because the generator is not designed to generate a huge amount of power and limits itself from generating more power.

Table 4.5: Mean Voltage, Current & Power for SIVCT Position 1

Wind Speed [mph]	Mean Voltage [V]	Mean Current [A]	Mean Power [W]
18	1.0767	0.0018	0.0019
19	1.6747	0.0028	0.0046
20	1.7200	0.0029	0.0049
21	1.8362	0.0031	0.0056
22	1.9872	0.0033	0.0065

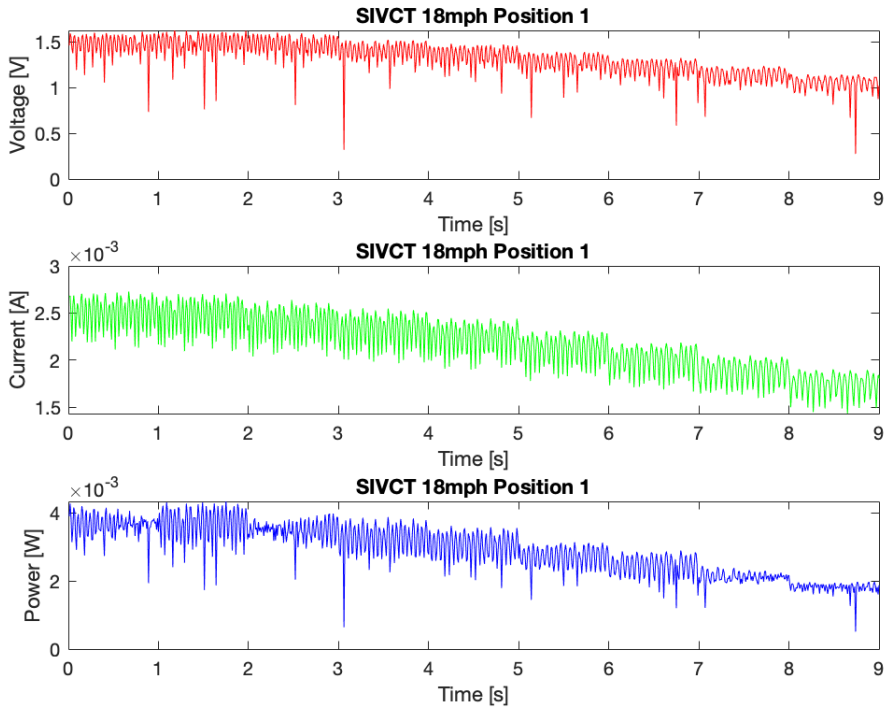

Figure 4.28: Voltage, Current, Power SIVCT at Position 1 & 18 mph

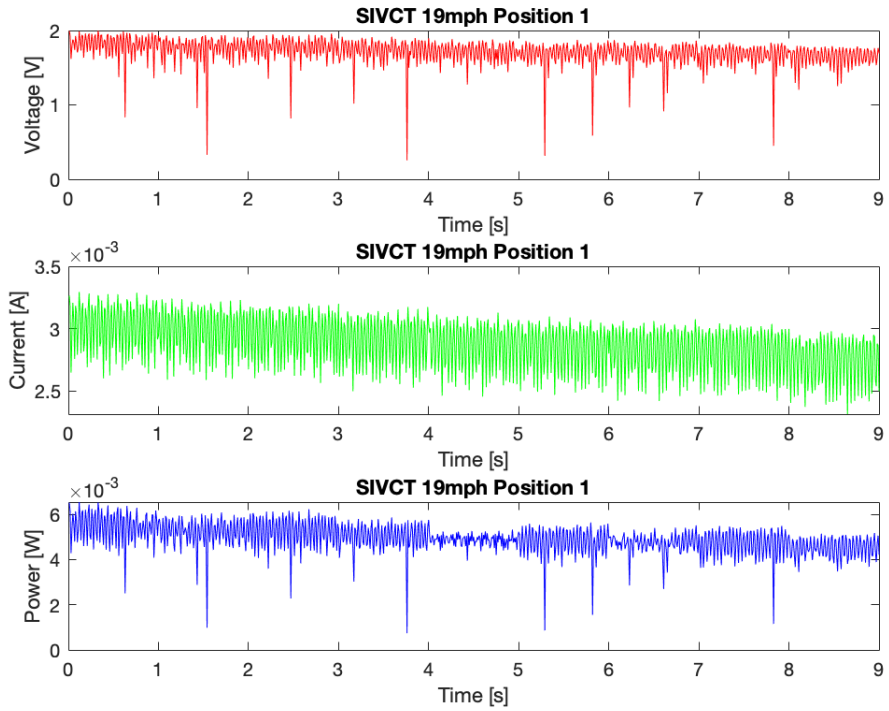

Figure 4.29: Voltage, Current, Power SIVCT at Position 1 & 19 mph

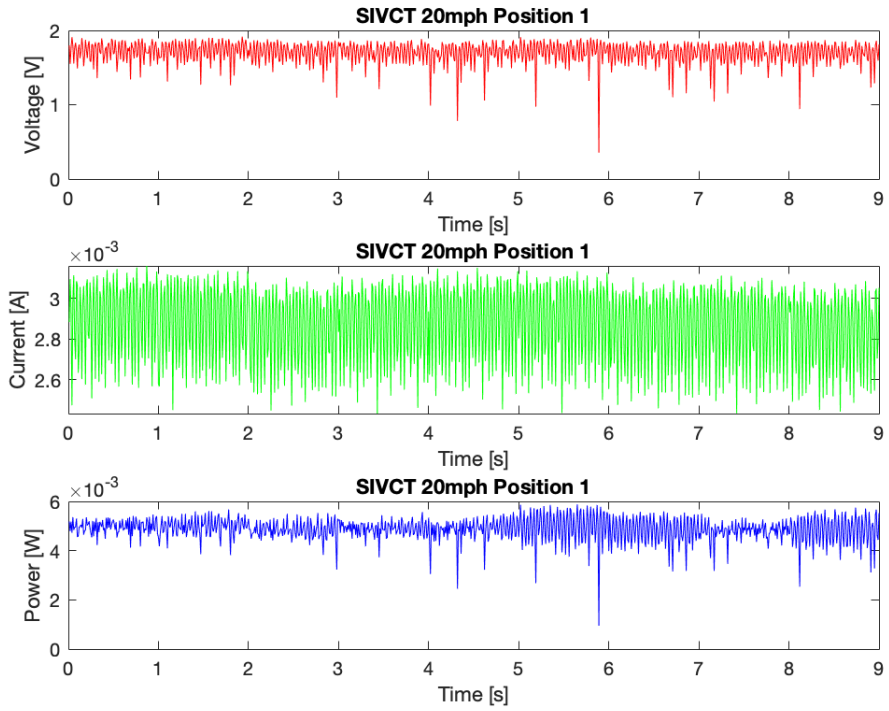

Figure 4.30: Voltage, Current, Power SIVCT at Position 1 & 20 mph

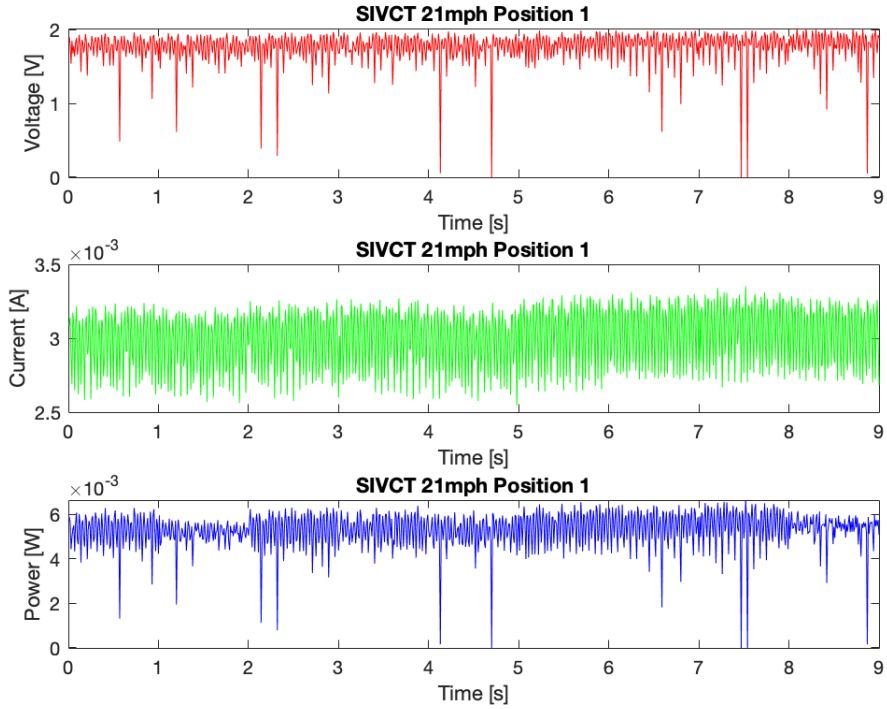

Figure 4.31: Voltage, Current, Power SIVCT at Position 1 & 21 mph

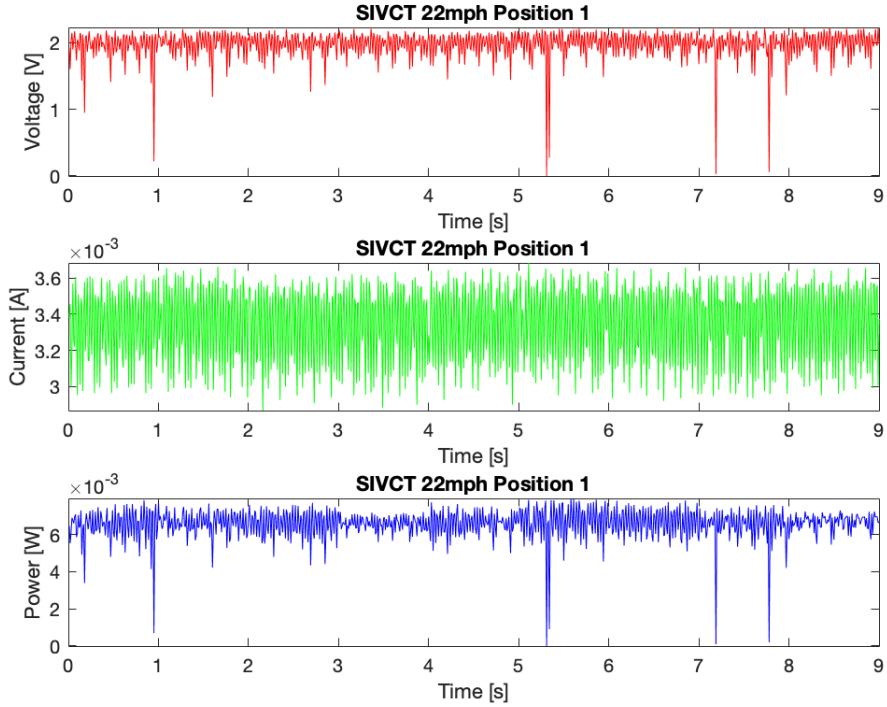

Figure 4.32: Voltage, Current, Power SIVCT at Position 1 & 22 mph

The same correlation can be seen when placing the turbine in position 2. The higher the wind speed, the higher the power production. It is unclear why the power generated at 21 mph is less than it was at 20 mph. Table 4.6 clearly shows the mean voltage, mean current, and mean power generated. The mean voltage rises with wind speed besides from 20 mph to 21 mph. It is possible, that the vortices have a big impact on the behavior of the turbine at that speed since the measured average speed does not show any significant jumps or drops over the 10 seconds. It can clearly be seen, the intensity of the sinusoidal fluctuation of the voltage, current, and power is not as frequent as it was the case when studying the data for the turbine in position 1.

Table 4.6: Mean Voltage, Current & Power for SIVCT Position 2

Wind Speed [mph]	Mean Voltage [V]	Mean Current [A]	Mean Power [W]
18	0.2968	0.000511	0.000159
19	0.3216	0.000493	0.000154
20	0.5072	0.0007825	0.000401
21	0.2835	0.0004875	0.0001435
22	0.6257	0.001	0.0006545

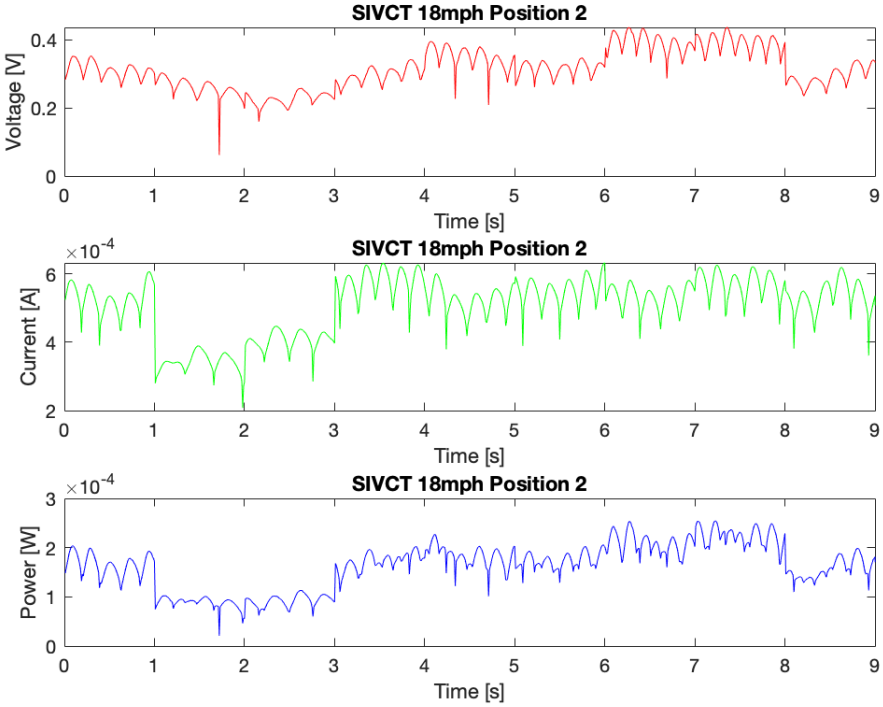

Figure 4.33: Voltage, Current, Power SIVCT at Position 2 & 18 mph

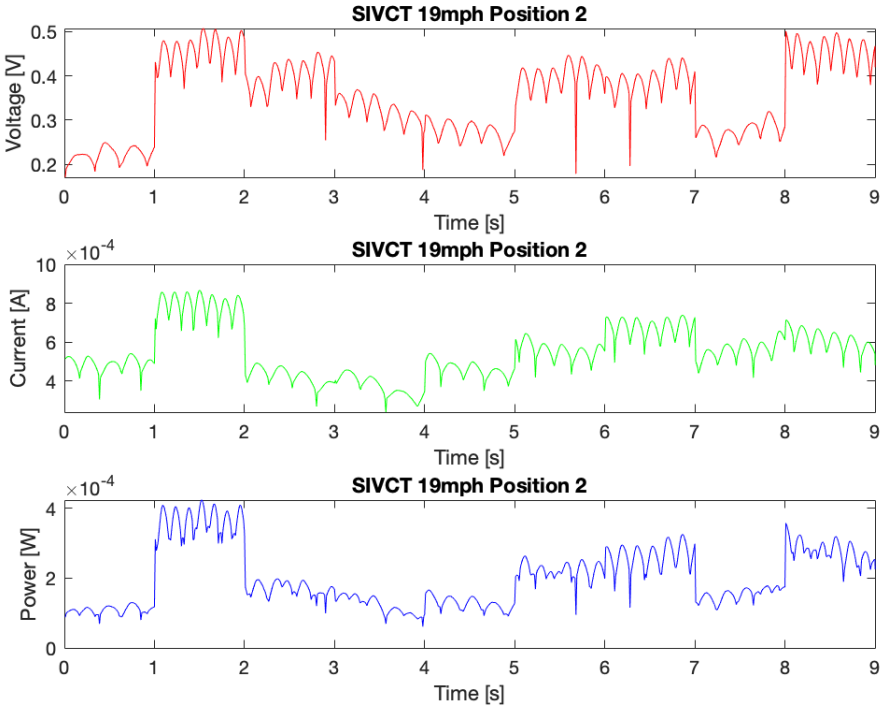

Figure 4.34: Voltage, Current, Power SIVCT at Position 2 & 19 mph

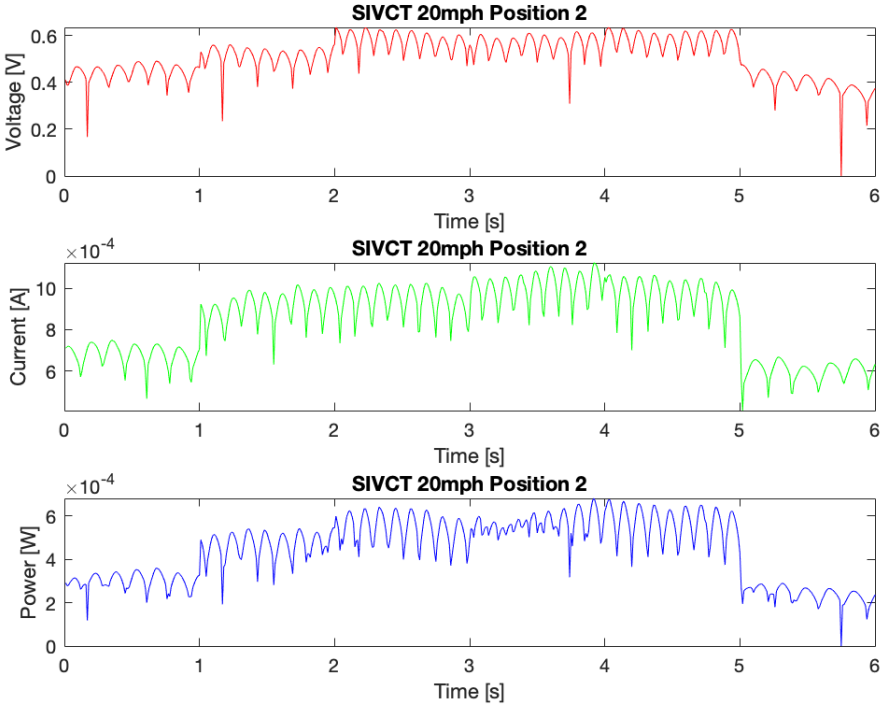

Figure 4.35: Voltage, Current, Power SIVCT at Position 2 & 20 mph

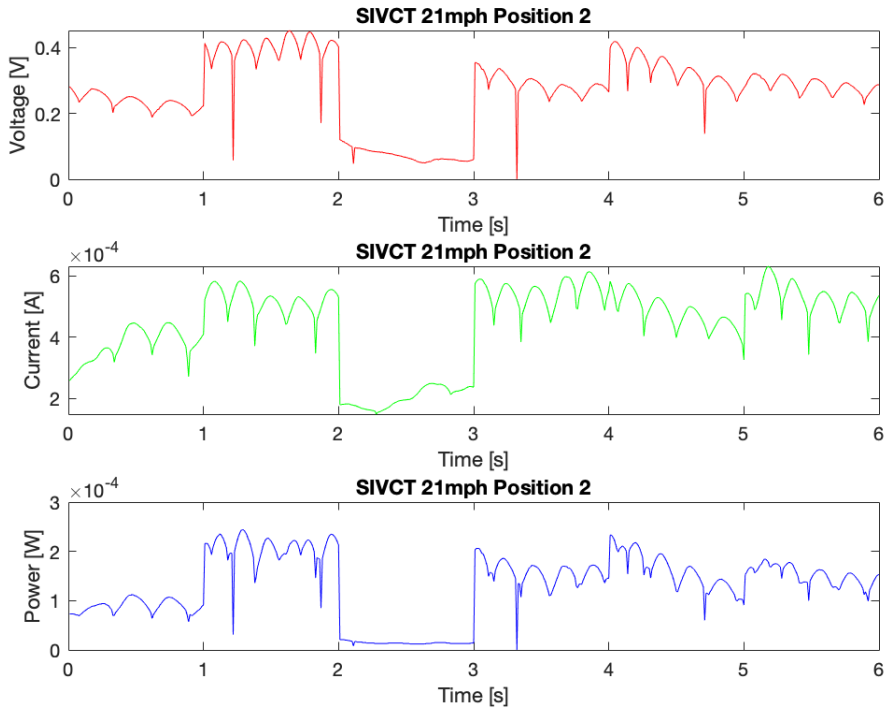

Figure 4.36: Voltage, Current, Power SIVCT at Position 2 & 21 mph

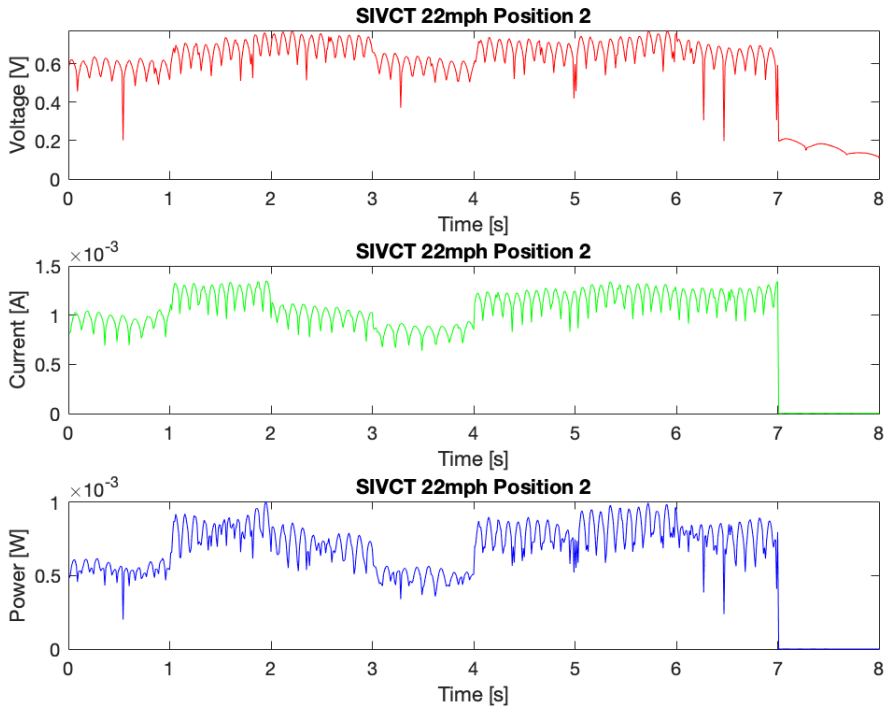

Figure 4.37: Voltage, Current, Power SIVCT at Position 2 & 22 mph

When placing the turbine in position 3, it did not spin. Several tries have lead to the same result. One possibility is that the turbine gets hit from both sides in opposite directions and the forces that act on the turbine cancel each other out. It was seen earlier, the two vortices, that rotate in opposite directions, can be found in almost the same location which lies centrally behind the obstacle.

4.3.2 Energy Generation NPVT

Again, first the turbine speeds are studied for the NPVT. It is clearly seen, this type of turbine reacts faster to the giving conditions. Starting at 15 mph, the turbine starts spinning in position 1 and 2. In position 1 it starts with 1000 rpm and at position 2 it starts with 750 rpm. For both positions, the speed gradually increases with the increase in wind speed. However, again, a tremendous difference can be seen between position 1 and position 2. The wind turbine produces significantly higher speeds in position 1 than it does in position 2. The peaks differ from 2400 rpm to 1750 rpm. That is close to a 30% decrease from position 1 to position 2. Again, all speeds are averages over a longer time span.

Table 4.7: NPVT Average Speed at Position 1

Wind Speed [mph]	**Turbine Speed [rpm]**
15	1000
16	1200
17	1300
18	1600
19	1800
20	2000
21	2200
22	2400

Table 4.8: NPVT Average Speed at Position 2

Wind Speed [mph]	**Turbine Speed [rpm]**
15	750
16	950
17	1100
18	1200
19	1400
20	1550
21	1650
22	1750

Figure 4.38 to Figure 4.55 show the voltage, current, and power generated with the NPVT in position 1 and position 2 at various wind speeds. A few new findings can be made compared to the SIVCT. The NPVT is more sensitive. Even at low speeds as 13 mph, the turbine rotates and creates a small amount of power. It

produces small amounts of power until the wind tunnel reaches a speed of 20 mph. As seen in Table 4.9, from 19 mph to 20 mph an increase from 0.000185 V to 0.0053 is recorded. The same can be seen in Figure 4.44 and Figure 4.45. The speed of the turbine spikes and therefore creates a significant higher amount of power. As seen before when studying the SIVCT, the highest power production is recorded at a wind speed of 22 mph. The produced power is 0.0066 W and therefore slightly higher than the 0.0065 W recorded with the SIVCT at position 1. It can be said, the NPVT is sightly more suitable in position 1. It is more sensitive to slow wind speeds and it also produces more power at high wind speeds.

Table 4.9: Mean Voltage, Current & Power for NPVT Position 1

Wind Speed [mph]	Mean Voltage [V]	Mean Current [A]	Mean Power [W]
13	0.1184	0.000194	0.000023
14	0.1870	0.000315	0.000059
15	0.2066	0.000346	0.000071
16	0.2391	0.000407	0.000096
17	0.2617	0.000440	0.000114
18	0.2922	0.000495	0.000142
19	0.3323	0.000565	0.000185
20	1.7871	0.0030	0.0053
21	1.8922	0.0032	0.0059
22	2.0031	0.0034	0.0066

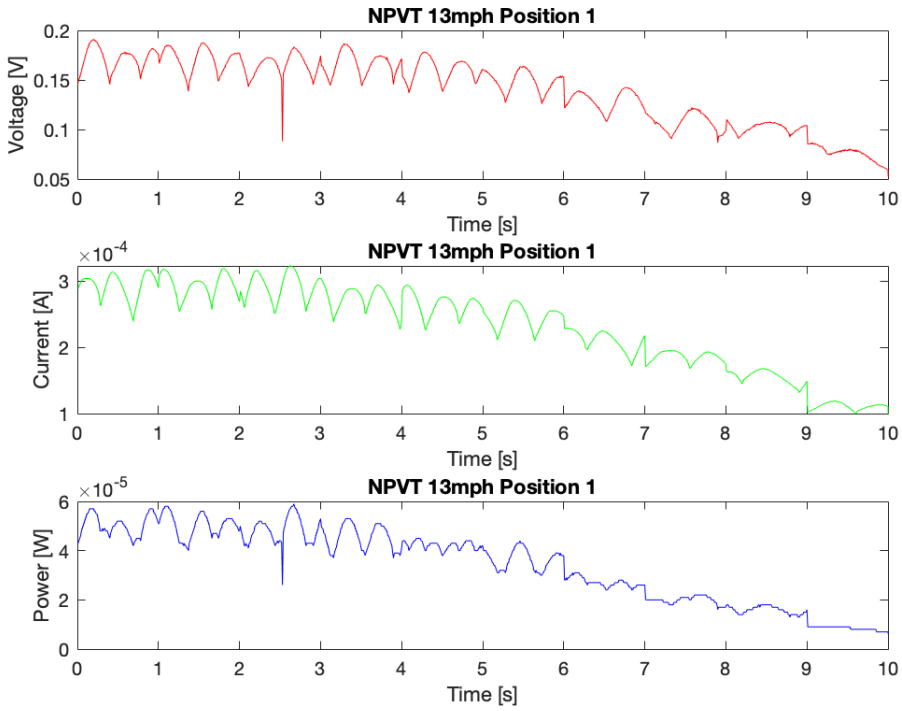

Figure 4.38: Voltage, Current, Power NPVT at Position 1 & 13 mph

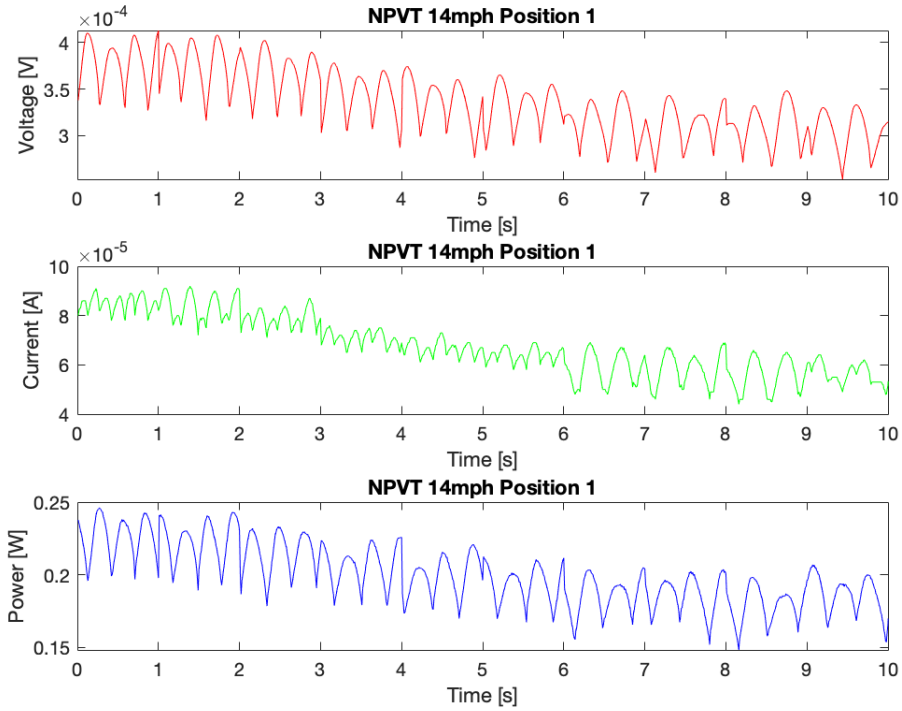

Figure 4.39: Voltage, Current, Power NPVT at Position 1 & 14 mph

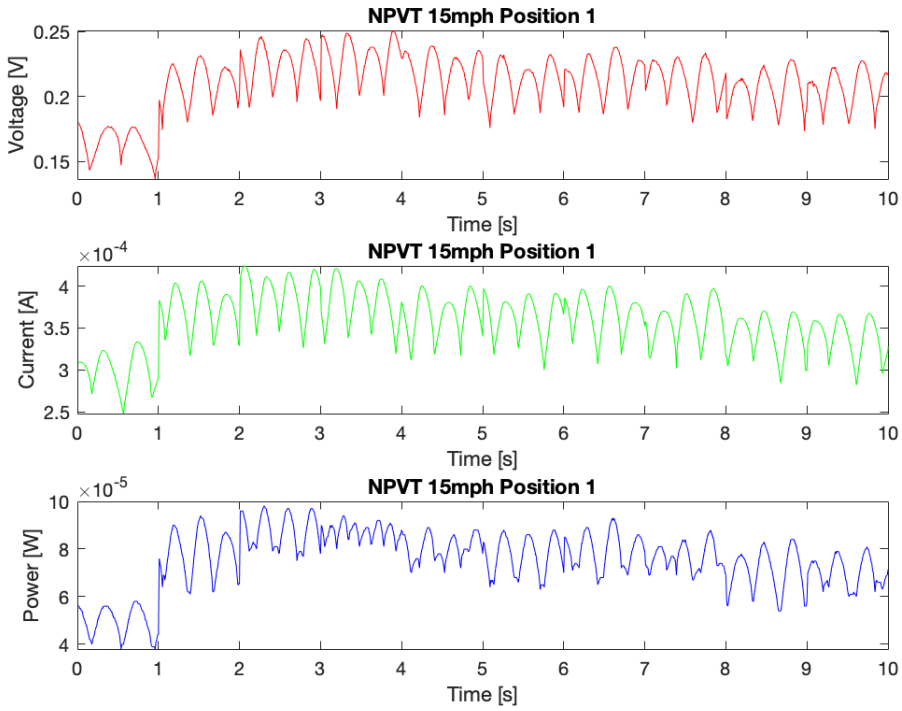

Figure 4.40: Voltage, Current, Power NPVT at Position 1 & 15 mph

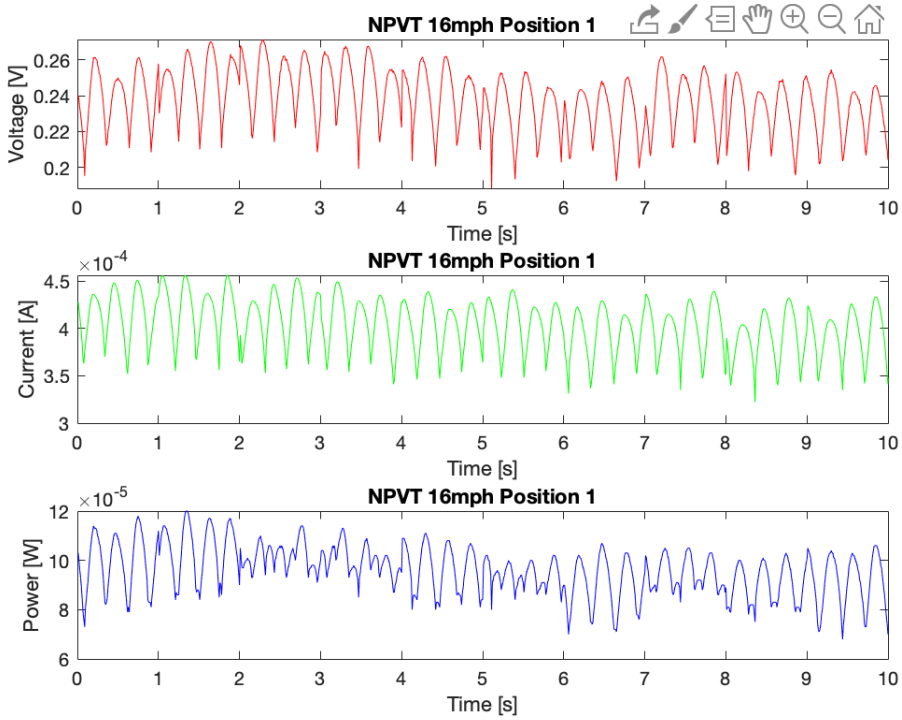

Figure 4.41: Voltage, Current, Power NPVT at Position 1 & 16 mph

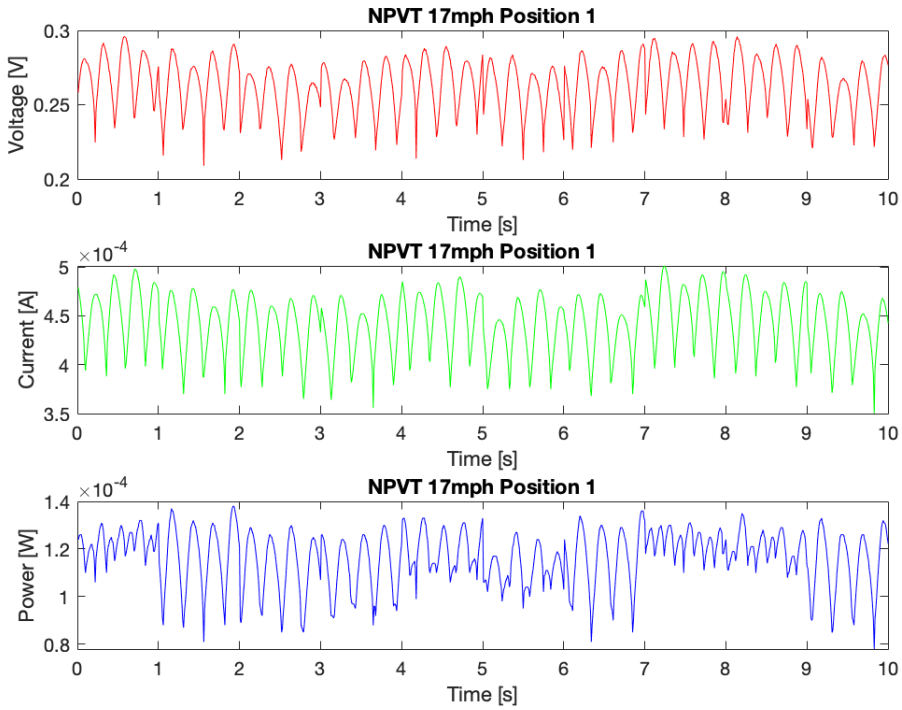

Figure 4.42: Voltage, Current, Power NPVT at Position 1 & 17 mph

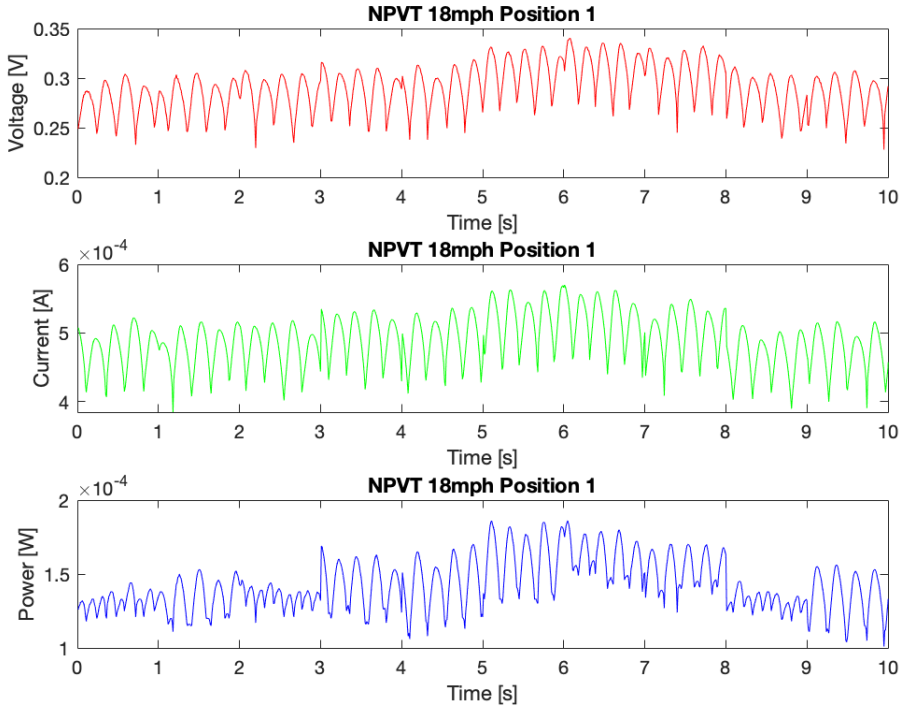

Figure 4.43: Voltage, Current, Power NPVT at Position 1 & 18 mph

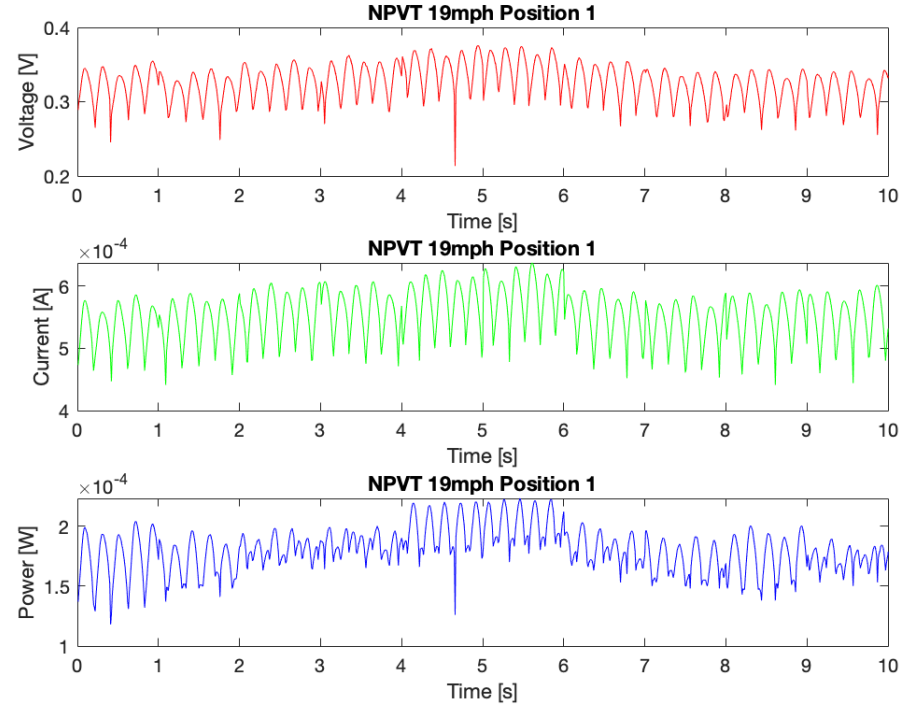

Figure 4.44: Voltage, Current, Power NPVT at Position 1 & 19 mph

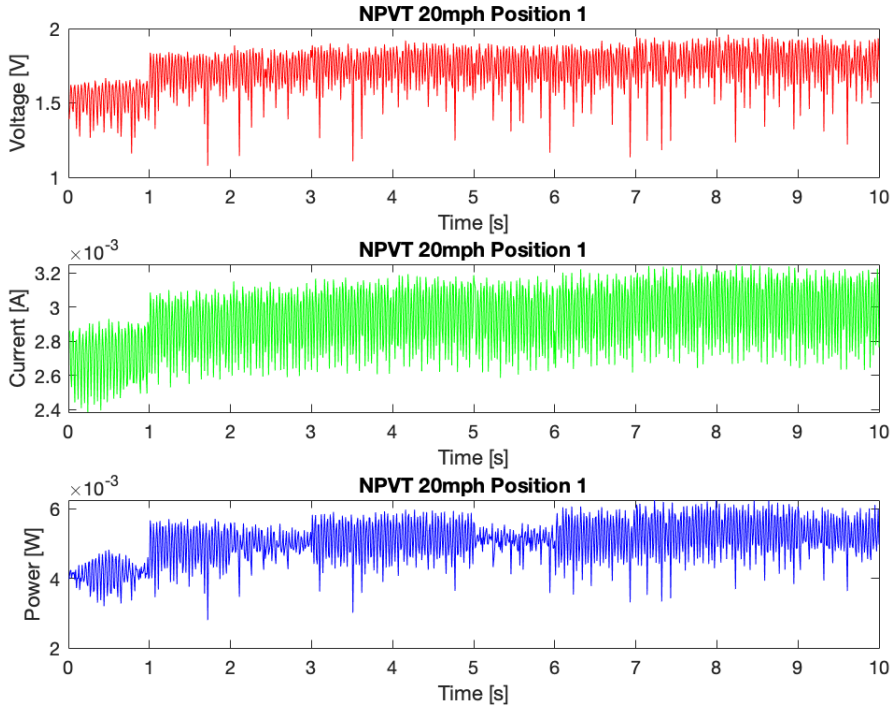

Figure 4.45: Voltage, Current, Power NPVT at Position 1 & 20 mph

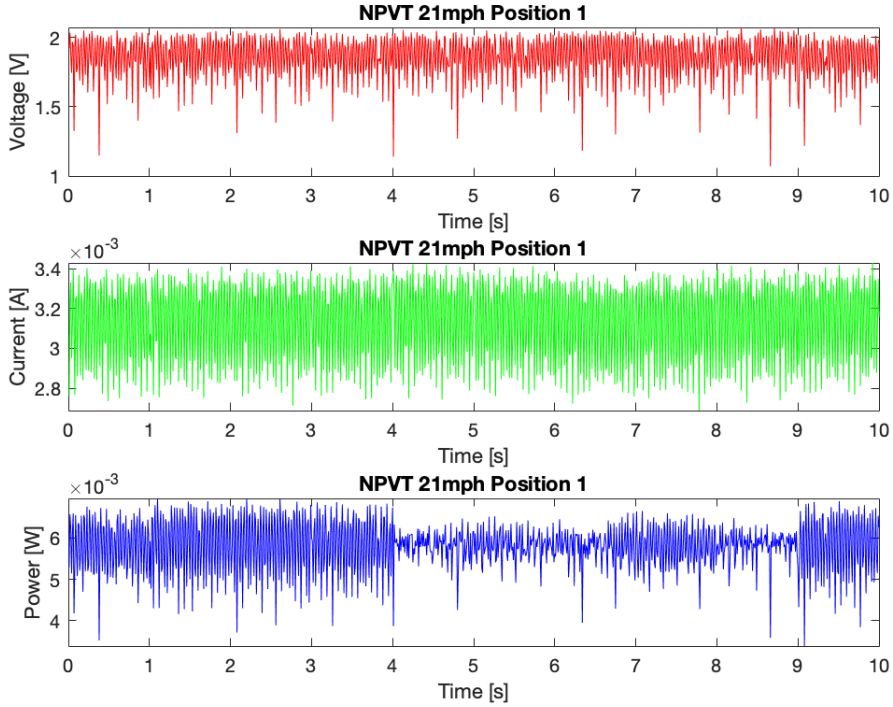

Figure 4.46: Voltage, Current, Power NPVT at Position 1 & 21 mph

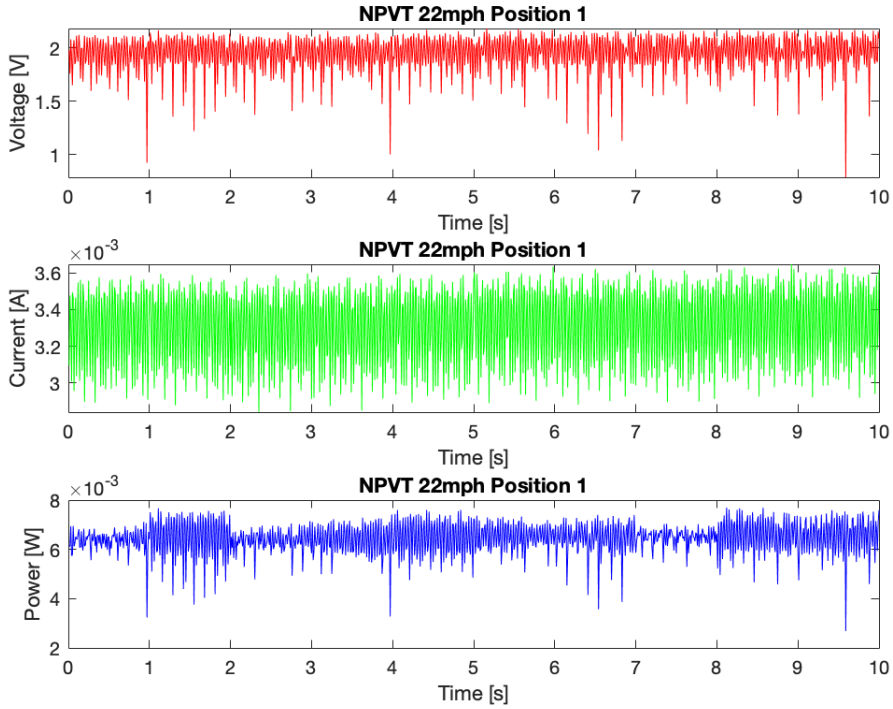

Figure 4.47: Voltage, Current, Power NPVT at Position 1 & 21 mph

Table 4.10: Mean Voltage, Current & Power for NPVT Position 2

Wind Speed [mph]	Mean Voltage [V]	Mean Current [A]	Mean Power [W]
15	0.3418	0.000597	0.00021
16	0.2197	0.000288	0.000062
17	0.4801	0.000790	0.000371
18	0.6447	0.0011	0.000692
19	0.6141	0.0010	0.0006255
20	0.7316	0.0012	0.00089
21	0.6969	0.0012	0.000813
22	0.8438	0.0014	0.0012

In position 2, the same phenomena as seen with the SIVCT in position 2 can be observed here as well. The power production increases with wind speed but there is a few speeds when the power drops. This decrease can be seen from 15 mph to 16 mph, from 18 mph to 19 mph , and from 20 mph to 21 mph. The exact values are displayed in Table 4.10. The drops are not significant besides the one from 15 mph to 16 mph. As mentioned before, position 2 lays right in the designated vortex position and the vortices can have a beneficial or harmful effect on the turbine behavior. At times, the graphs show very low values for voltage, current, and power which can be affiliated with the the turbine rotating slower at times.

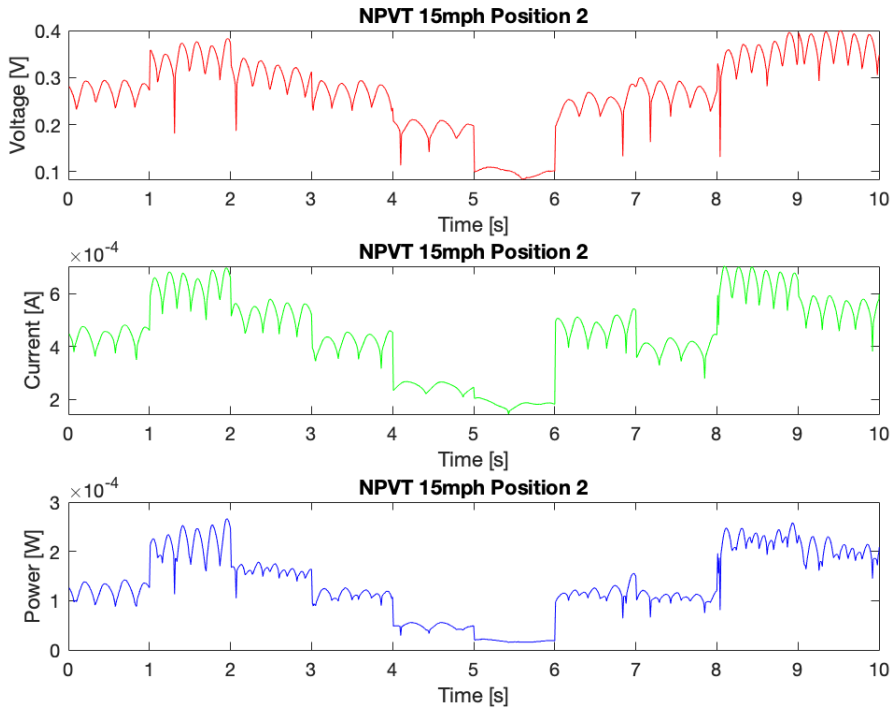

Figure 4.48: Voltage, Current, Power NPVT at Position 2 & 15 mph

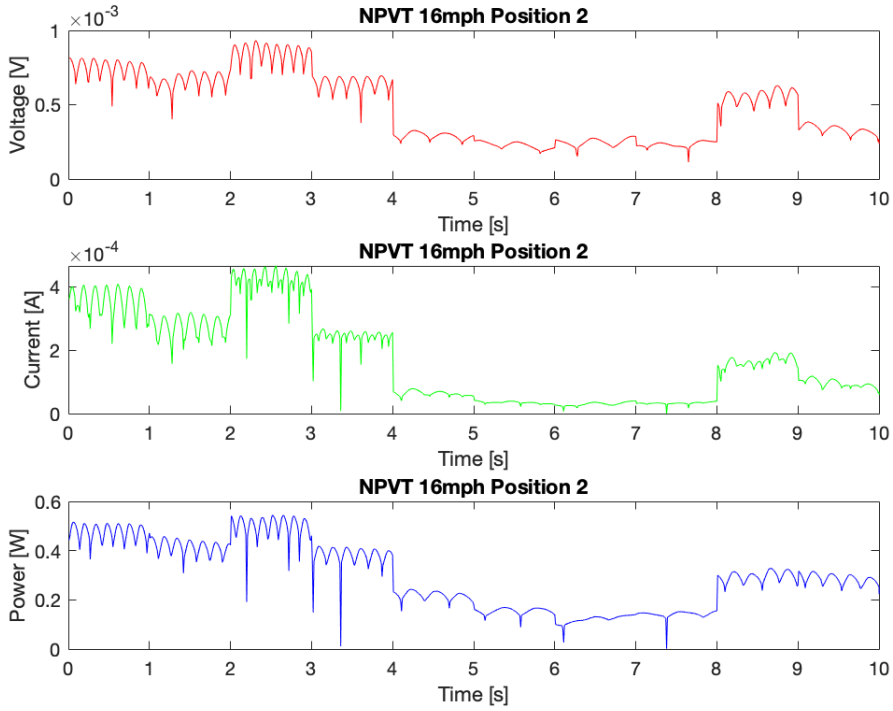

Figure 4.49: Voltage, Current, Power NPVT at Position 2 & 16 mph

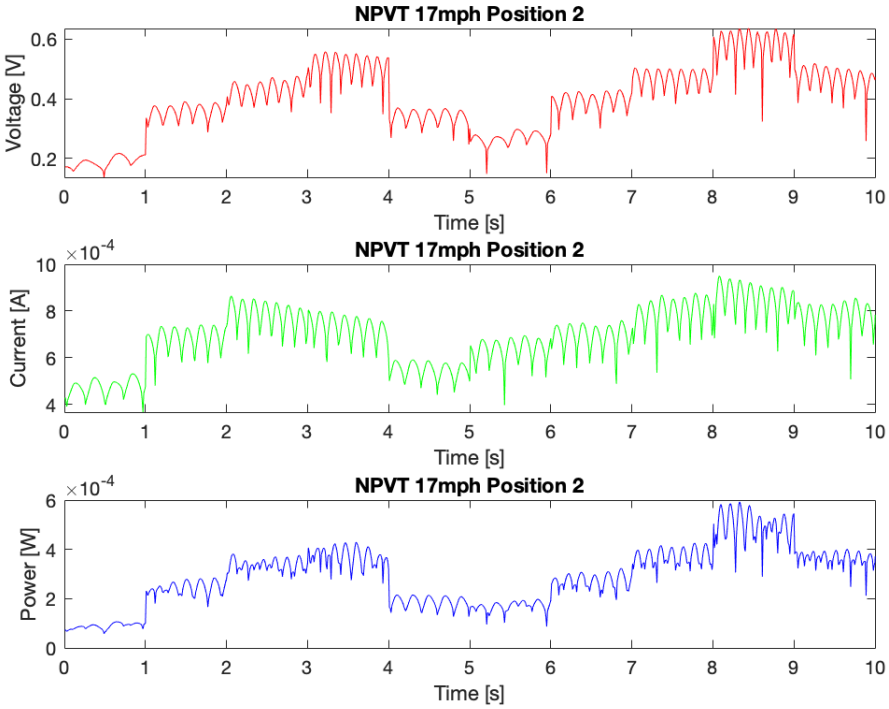

Figure 4.50: Voltage, Current, Power NPVT at Position 2 & 17 mph

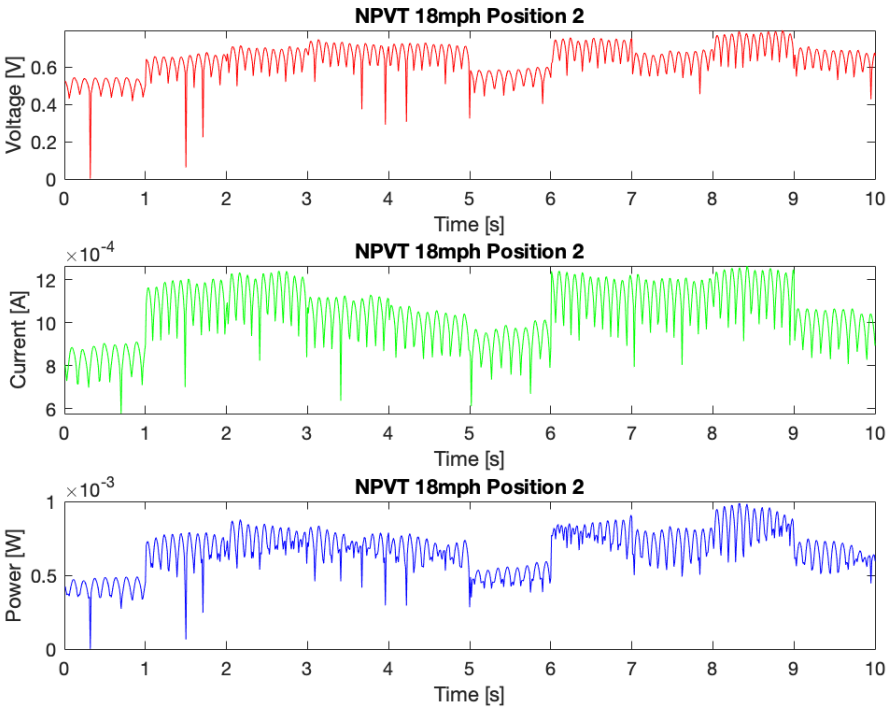

Figure 4.51: Voltage, Current, Power NPVT at Position 2 & 18 mph

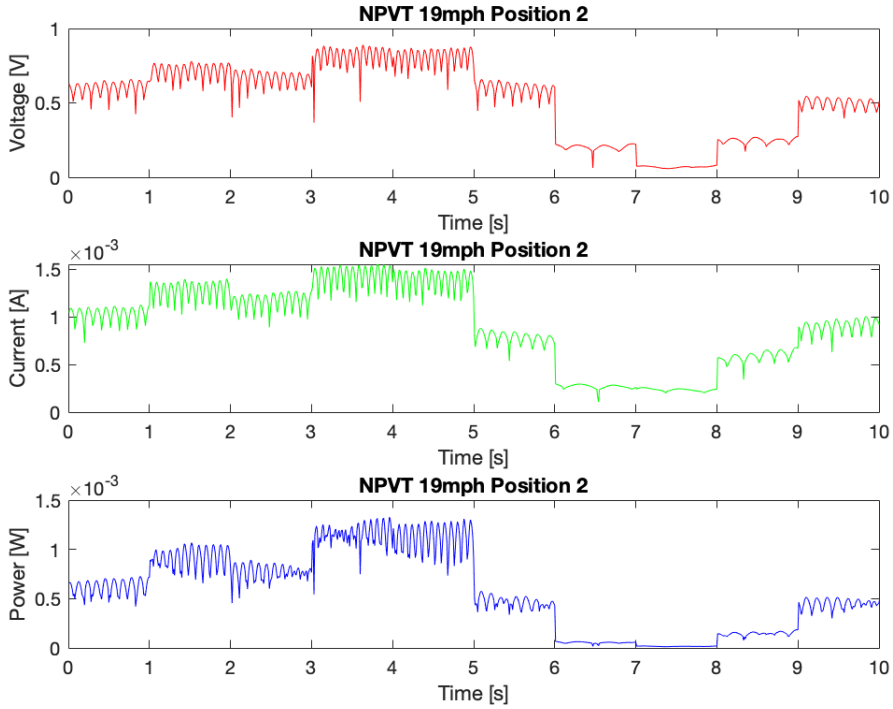

Figure 4.52: Voltage, Current, Power NPVT at Position 2 & 19 mph

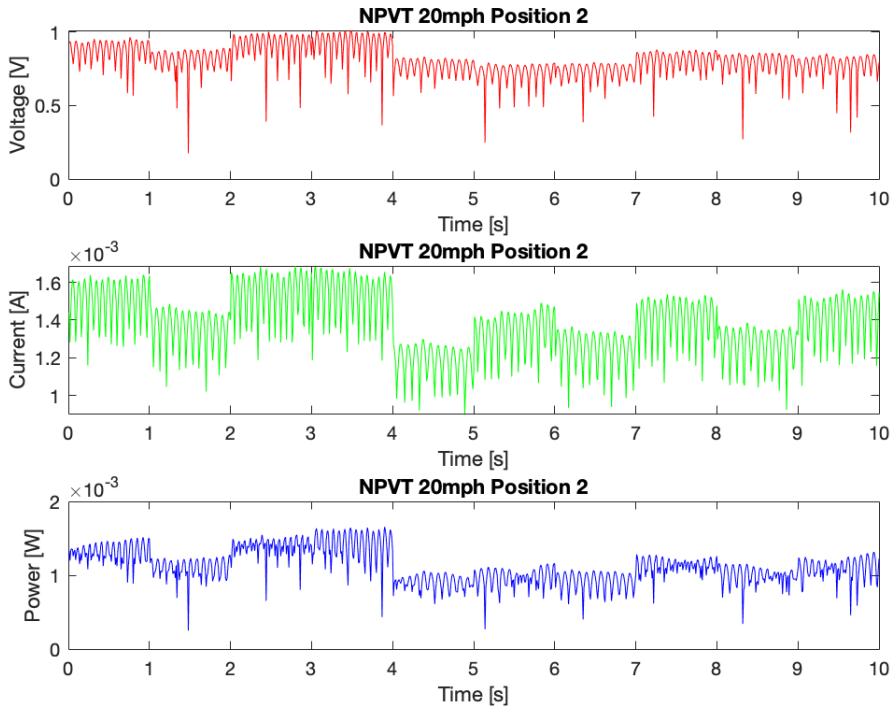

Figure 4.53: Voltage, Current, Power NPVT at Position 2 & 20 mph

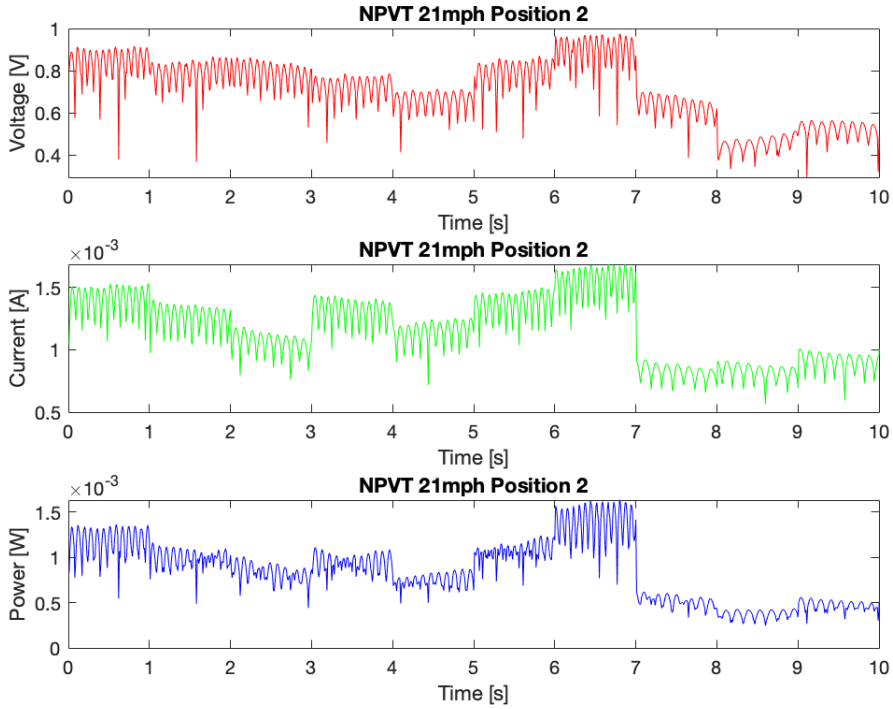

Figure 4.54: Voltage, Current, Power NPVT at Position 2 & 21 mph

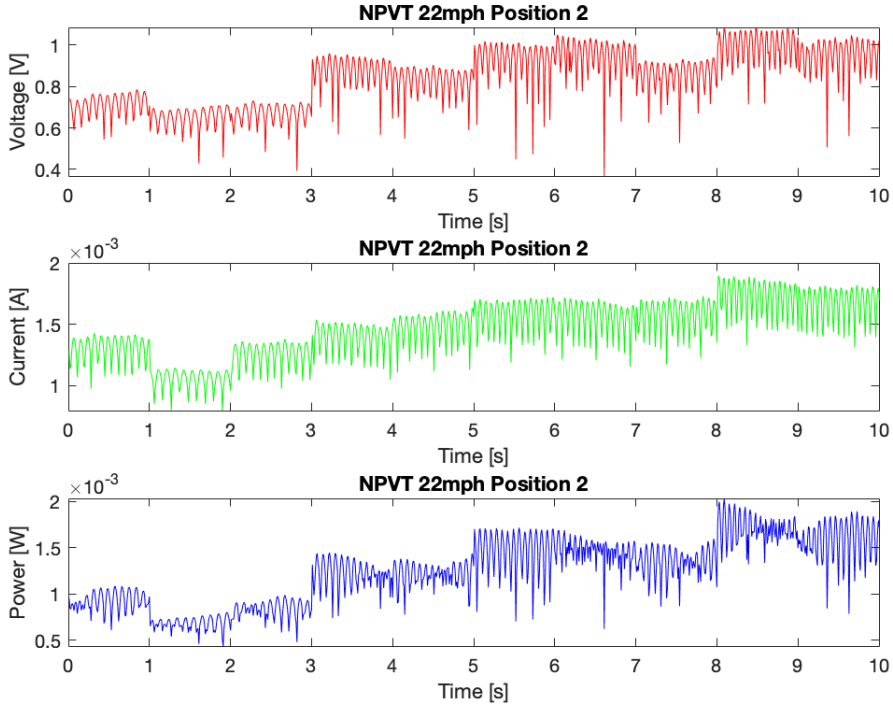

Figure 4.55: Voltage, Current, Power NPVT at Position 2 & 22 mph

Overall, the NPVT has, again, a better performance in terms of maximum power produced in position 2 compared to the SIVCT. At 22 mph the NPVT in position 2 produces a mean power output of 0.0012 W. The SIVCT produces at the same position and at the same wind speed only 0.0006545 W. Although, both turbines are quite similar in performance. Position 3, again, did not produce any significant spinning. It was possible to observe random spinning and a few singular rotations at high speeds. It is likely, this happens for the same reason the SIVCT Turbine does not rotate in position 3.

4.3.3 Power Spectral Density

The Power Spectral Density (PSD) is used to determine the frequency at which the turbine rotates and at what frequency the vortices possibly affect the flow and performance of the turbines. Figure 4.56 to Figure 4.83 show the visualized PSD for cases over the normalized frequency. The frequency is divided by the number of samples per second. With the following equations, the frequency for a given RPM can be determined.

$$\omega T = 2\pi \tag{4.2}$$

$$\omega = 2\pi \frac{1}{T} \tag{4.3}$$

$$\omega = 2\pi f, \tag{4.4}$$

where w is the speed of the wind turbine in rad/s and f is the frequency in Hz. Since the measured turbine speed is in RPM, the RPM has to be converted to rad/s. To convert the following applies:

$$rad/s = \frac{RPM}{60} * 2\pi. \tag{4.5}$$

So at a wind turbine speed of 800 RPM the frequency f equals to 131.6 Hz. At 2000 RPM the frequency f equals to 328.9 Hz. Those are relatively low frequencies. In Figure 4.57 the PSD for the SIVCT in position 1 at a wind speed of 19 mph is shown. Clearly, there is one very dominant frequency at which the wind interferes with the turbine. This is in position 1 where the vortices are not as prominent as in position 2. Figure 4.65 displays the same turbine in position 2 at 22 mph. This time, two dominant frequencies can be observed. One represents the normal flow acting on the wind turbine and the other one represents the vortices acting on the wind turbine. A pattern can be observed. The wind turbines most likely accelerate when a vortex directly acts on the turbine.

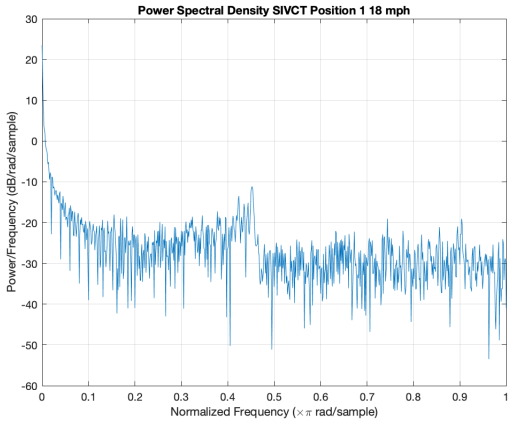

Figure 4.56: Power Spectral Density SIVCT at Position 1 & 18 mph

Figure 4.57: Power Spectral Density SIVCT at Position 1 & 19 mph

Figure 4.58: Power Spectral Density SIVCT at Position 1 & 20 mph

Figure 4.59: Power Spectral Density SIVCT at Position 1 & 21 mph

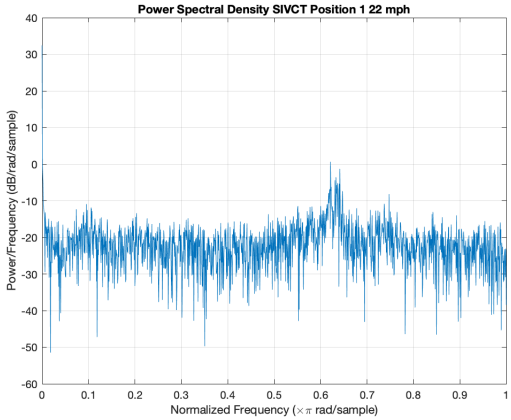

Figure 4.60: Power Spectral Density SIVCT at Position 1 & 22 mph

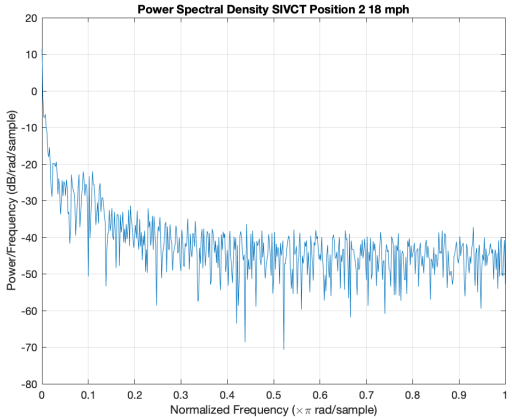

Figure 4.61: Power Spectral Density SIVCT at Position 2 & 18 mph

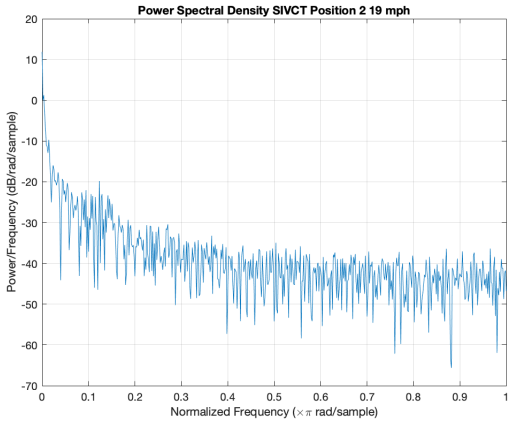

Figure 4.62: Power Spectral Density SIVCT at Position 2 & 19 mph

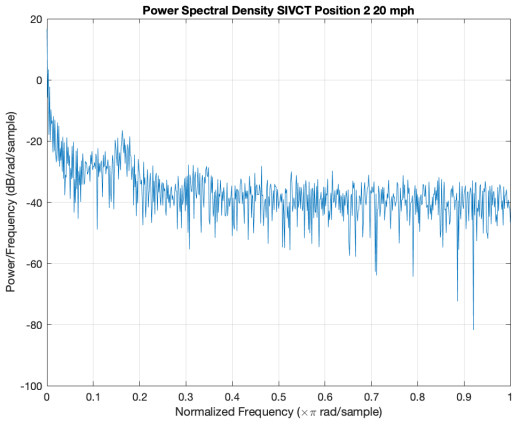

Figure 4.63: Power Spectral Density SIVCT at Position 2 & 20 mph

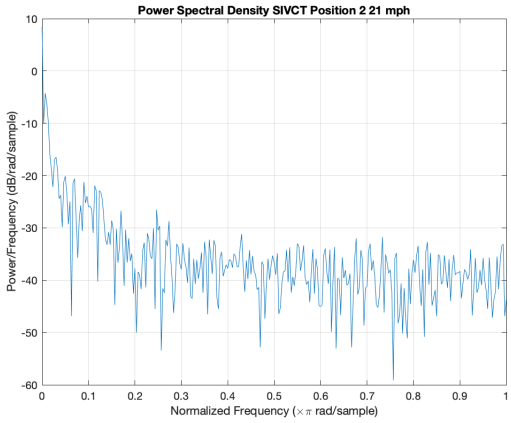

Figure 4.64: Power Spectral Density SIVCT at Position 2 & 21 mph

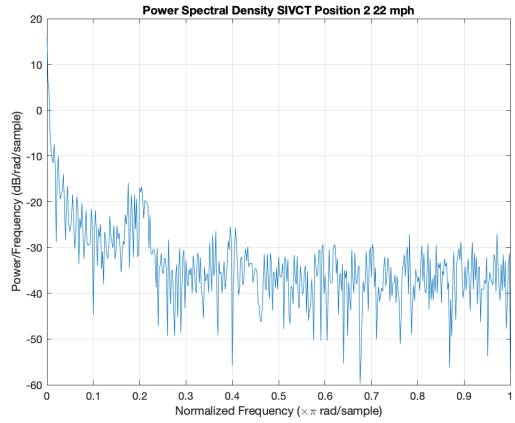

Figure 4.65: Power Spectral Density SIVCT at Position 2 & 22 mph

The same can be observed with the NPVT. Looking at Figure 4.71, where the PSD for the NPVT in position 1 at 18 mph is shown, one dominant frequency can be seen. Figure 4.79 shows the PSD for the same Turbine in position 2 at 18 mph. Again, 2 dominant frequencies can be observed, one representing the normal flow and the other one representing the vortices. In some cases there can be observed two frequencies when the turbine is located in position 1 as well. It cannot clearly be said, that the vortices have no impact on the flow in that position.

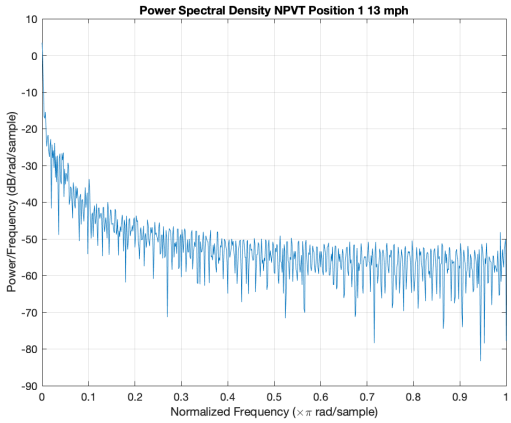

Figure 4.66: Power Spectral Density NPVT at Position 1 & 13 mph

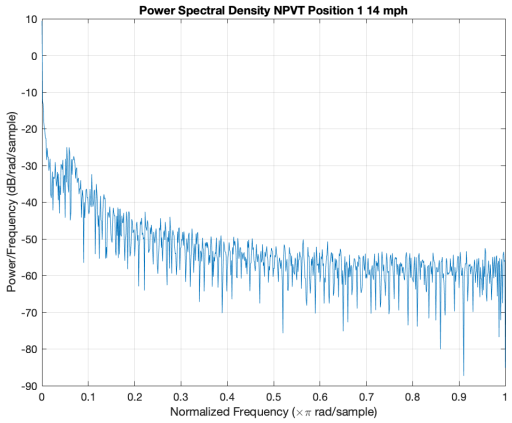

Figure 4.67: Power Spectral Density NPVT at Position 1 & 14 mph

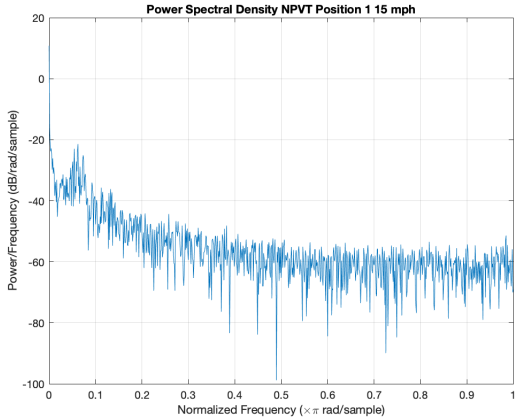

Figure 4.68: Power Spectral Density NPVT at Position 1 & 15 mph

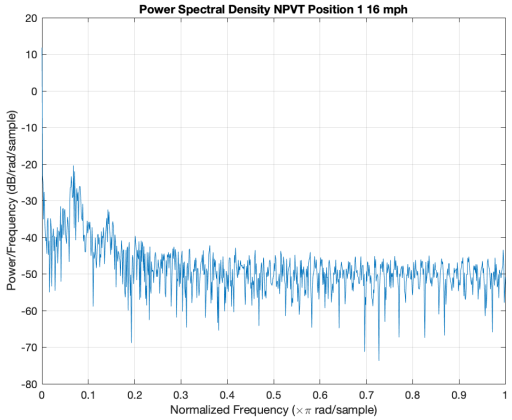

Figure 4.69: Power Spectral Density NPVT at Position 1 & 16 mph

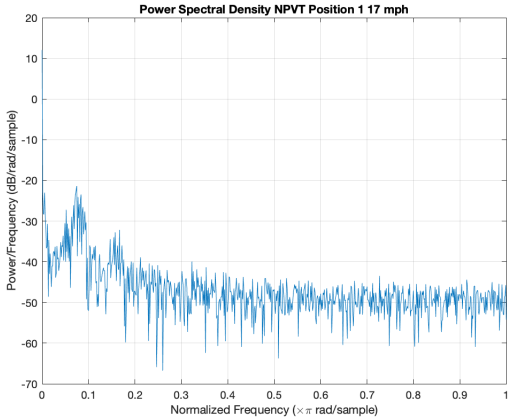

Figure 4.70: Power Spectral Density NPVT at Position 1 & 17 mph

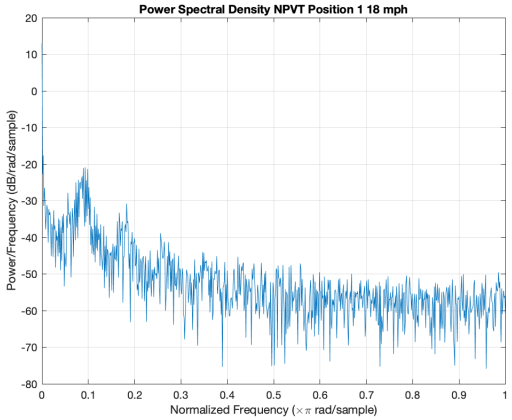

Figure 4.71: Power Spectral Density NPVT at Position 1 & 18 mph

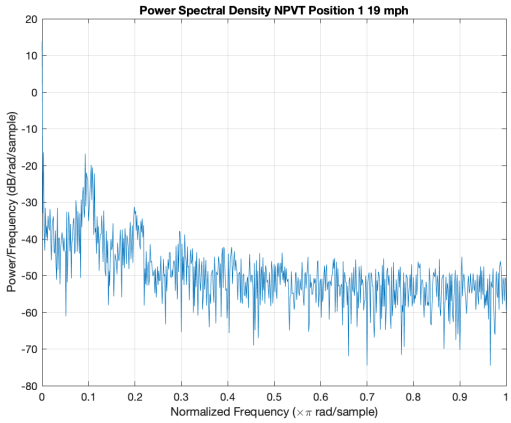

Figure 4.72: Power Spectral Density NPVT at Position 1 & 19 mph

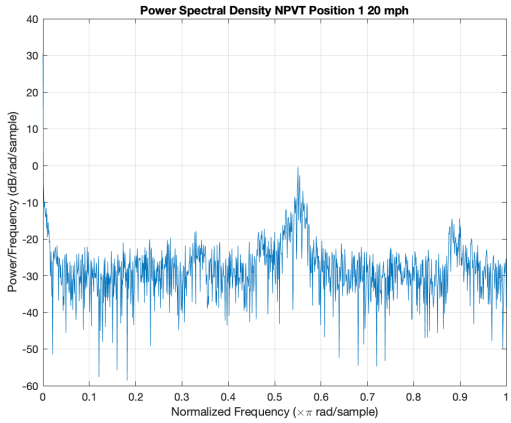

Figure 4.73: Power Spectral Density NPVT at Position 1 & 20 mph

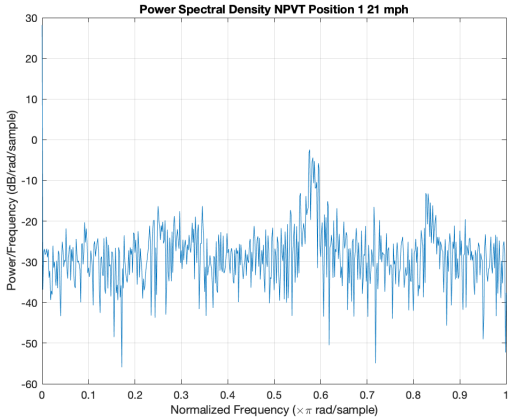

Figure 4.74: Power Spectral Density NPVT at Position 1 & 21 mph

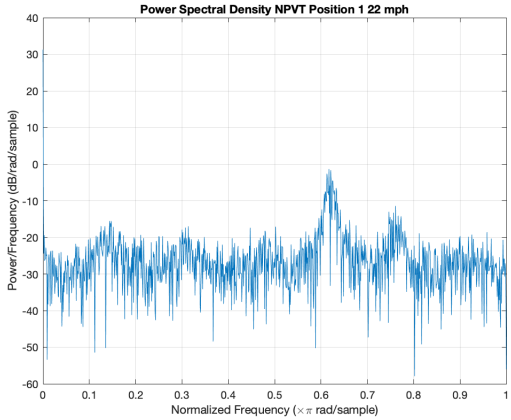

Figure 4.75: Power Spectral Density NPVT at Position 1 & 22 mph

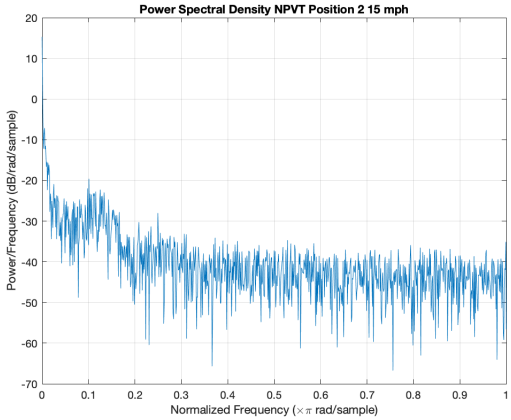

Figure 4.76: Power Spectral Density NPVT at Position 2 & 15 mph

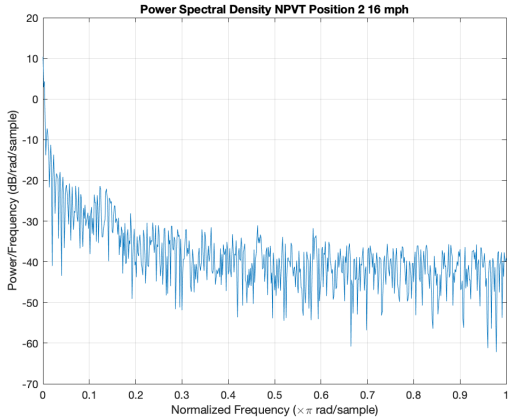

Figure 4.77: Power Spectral Density NPVT at Position 2 & 16 mph

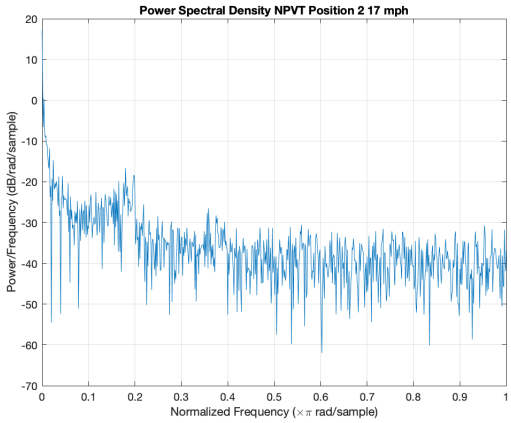

Figure 4.78: Power Spectral Density NPVT at Position 2 & 17 mph

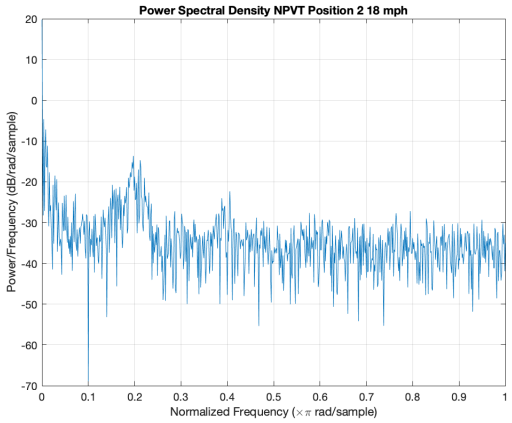

Figure 4.79: Power Spectral Density NPVT at Position 2 & 18 mph

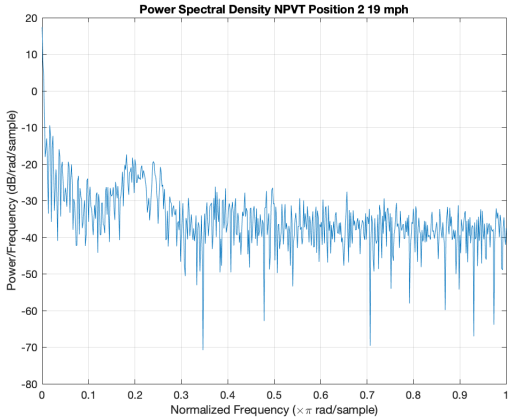

Figure 4.80: Power Spectral Density NPVT at Position 2 & 19 mph

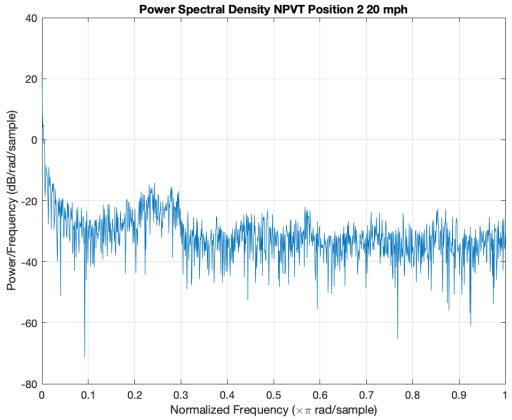

Figure 4.81: Power Spectral Density NPVT at Position 2 & 20 mph

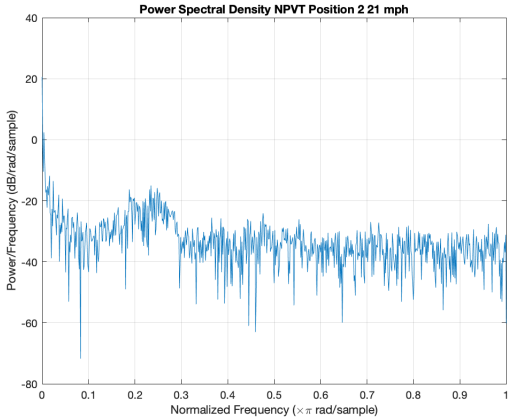

Figure 4.82: Power Spectral Density NPVT at Position 2 & 21 mph

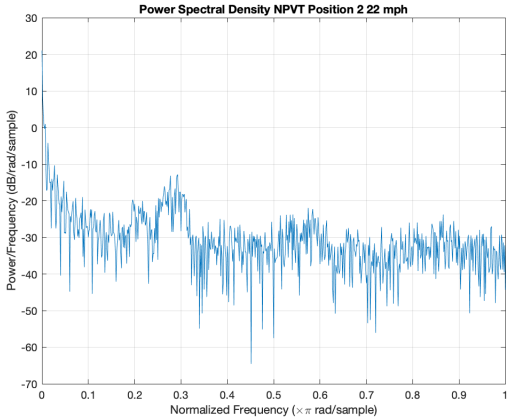

Figure 4.83: Power Spectral Density NPVT at Position 2 & 22 mph

4.3.4 Tip Speed Ratio

The Tip Speed Ratio (TSR) is calculated for both turbines at the tested conditions. The following Table displays the results for the TSR calculation. Table 2.1 gives the theoretical optimum TSR for a certain number of blades. For 2 blades the optimum TSR is 6. It is seen, this number does not get reached with the SIVCT. The design limitations and the wind tunnel limitations did not make it possible to generate higher wind speed and therefore a higher rotational speed which would, considering the results displayed in Table 4.11 and Table 4.12, lead to a higher TSR. For a turbine with 4 blades, the optimum TSR is 4. As shown in Table 4.13, this number is reached with the NPVT in position 1 at a speed of 9.8 m/s or 22 mph. This means, the NPVT created the optimum power output at that speed. Locating the turbine in position 2, the optimum number is not reached.

Table 4.11: Calculated TSR for SIVCT Position 1

Wind Speed [m/s]	Turbine Speed [RPS]	TSR
8	13.3	1.6
8.4	15	1.8
8.9	18.3	2.1
9.4	33.3	3.5
9.8	38.3	3.9

Table 4.12: Calculated TSR for SIVCT Position 2

Wind Speed [m/s]	Turbine Speed [RPS]	TSR
8	11.6	1.5
8.4	15	1.8
8.9	16.6	1.9
9.4	20	2.1
9.8	21.6	2.2

Table 4.13: Calculated TSR for NPVT Position 1

Wind Speed [m/s]	Turbine Speed [RPS]	TSR
6.7	16.6	2.5
7.2	20	2.7
7.6	21.6	2.8
8	26.6	3.3
8.4	30	3.6
8.9	33.3	3.7
9.4	36.3	3.9
9.8	40	4.1

Table 4.14: Calculated TSR for NPVT Position 2

Wind Speed [m/s]	**Turbine Speed [RPS]**	**TSR**
6.7	12.5	1.9
7.2	15.8	2.2
7.6	18.3	2.4
8	20	2.5
8.4	23.3	2.8
8.9	25.8	2.9
9.4	27.5	2.9
9.8	29.2	3

5

Conclusion

This Thesis was designed to investigate the power production with small scale vertical wind turbines, placed behind an obstacle that creates vortices. Ideally, the vortices increase the productivity and efficiency of the vertical axis wind turbines (VAWT). The results obtained in the performed experiments show, vortices have the potential of improving the energy production with VAWT. Vortices can occur naturally when wind blows past buildings or behind driving cars and trucks. As seen, the NPVT has a TSR of 4.1 when the wind speed is 9.8 m/s. This can well be a real scenario. Throughout all experimantal runs, it can be said that the vortices have a positive impact on the power generation. In some cases more than in others. For example, the power production is greater, when the turbines are placed outside of the area right behind the obstacle in position 1. In those cases, most vortices only partly cross the turbine. Based on the power production plots and the sinusoidal behavior, the turbine rotating speed increases with every vortex interference. However, the impact is more prominent in position 2. In the power spectral density plots, two clear and dominant frequencies can be observed. In this position the vortices interfere with the turbines more often in the same time span. Such a scenario, where the turbine is placed behind an obstacle can also be created at a driving car. Small energy production can be used to power the air conditioning. When the two turbines are compared, the NPVT comes out on top over the SIVCT. It creates a higher power output and reaches the optimum Tip Speed Ratio well before the SIVCT would. This is continuous throughout both turbine positions. Since the SIVCT has not reached its full potential at the highest tested speed of 22 mph or 11 m/s, it would be interesting to see how it behaves at very high speeds that, for example, can be created with a driving car. This method of VAWT can be highly productive and lucrative. The drive for more efficient and competitive techniques for energy production will not stop in the near future. The electrification is a very important factor in today's world and especially today's automotive field. Almost all governments and automotive companies have one common goal. They have the aspiration of decreasing harmful emissions like CO_2, NO_x, and particle matter (PM). Electric vehicles almost produce non of the names emissions and also operate significantly quieter than conventional combustion engine operated cars. The harmful emissions can cause health, physical, and physiological problems, sleep and behavioral disorders, and memory and concentration losses to residents, pedestrians, and drivers. National, state, and local governments ban certain vehicles from certain zones inside cities to reduce emissions in those zones. Wind energy is one of the renewable energy sources and therefore widely supported when serving additional electricity demands. With the increase of electrified vehicles and the resulting higher

overall electricity consumption new and innovative forms of power production are needed. Wind turbine energy is extensively used for powering electric cars. This research can have a tremendous impact on the energy production in the near future and therefore assist in reaching the common goal of a more sustainable future.

Bibliography

[1] Gustaver, M. (2020) A Chalmers University of Technology Master's thesis template for LaTeX. Unpublished.

[2] Hau, E. *Wind Turbines.* Springer. Berlin, Heidelberg. (2013)

[3] Golding, E.W. *The Generation of Electricity by Wind Power.* E. & F.N. Spon Ltd. New York. (1977)

[4] vortex
https://www.merriam-webster.com/dictionary/vortex

[5] tornado
https://www.noaa.gov/education/resource-collections/weather-atmosphere/tornadoes

[6] Freymuth, Peter, et al. *Vortices around Airfoils: The Flow around an Airfoil in Unsteady Wind Provides Insight into a Difficult Realm of Aerodynamics.* American Scientist, vol. 72, no. 3, 1984, pp. 242–248. JSTOR, www.jstor.org/stable/27852644.

[7] Sunden, Bengt *Tubes, Crossflow over DOI* : $10.1615/AtoZ.t.tubes_crossflow_over$. https://thermopedia.com/content/1216/. 2011.

[8] Shademani, Roya and Ghadimi, et. al., *Assessment of Air Flow over an Equilateral Triangular Obstacle in a Horizontal Channel Using FVM.* Journal of Mathematical Sciences and Applications. vol 1. pages 12-16. 2013.

[9] Energy use in Sweden
https://sweden.se/nature/energy-use-in-sweden/

[10] flec01
https://davis68.github.io/me498cf-fa16/resources/flec01.html

[11] Sunden, Bengt *Vortex Shedding* https://thermopedia.com/content/1247/. 2011.

[12] Zhang, Xing and Perot, Blair. *TURBULENT VORTEX SHEDDING FROM TRIANGLE CYLINDER USING THE TURBULENT BODY FORCE POTENTIAL MODEL.* 2000

[13] https://www.vertogen.eu/wind-turbine-history/

[14] https://tsi.com/produktbestandteile/insight-4g-version-11-2-global-imaging,-acquisition,-analysis-and-display-software/

[15] Yagmur, Sercan. et. al., Comparrison of flow characteristics around an equilateral triangular cylinder via PIV and Large Eddy Simulation methods. 2016.

[16] Quaschning, Volker. Understanding Renewable Energy Systems. 2005. Earthscan Publications Ltd.

[17] *https://mmpa.org/wp-content/uploads/2015/09/Tip-Speed-Ratio-Provided-by-Kid-Wind-PDF.pdf*
[18] Andersson, Bengt. et. al., CFD for Engineers. 2012.
[19] Ponce, Genaro. What Is CAD? – Simply Explained. 2020 *https://all3dp.com/2/what-is-cad-design-simply-explained/*
[20] Westerweel, Jerry. Fundamentals of digital particle image velocimetry. 1997

A

Appendix A

This Appendix A shows multiple additional series of visible vortex shedding. Again, $t1 < t2$.

A.1 Additional Vortex Shedding Series 1

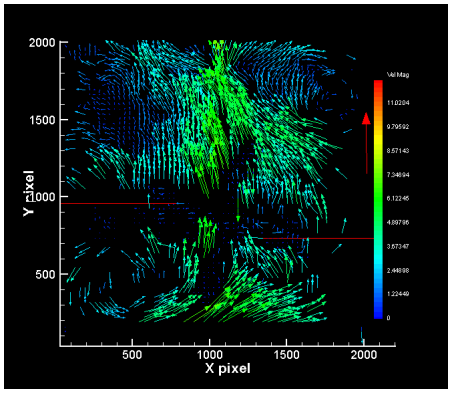

Figure A.1: Additional Vortex Shedding Series 1 at t1

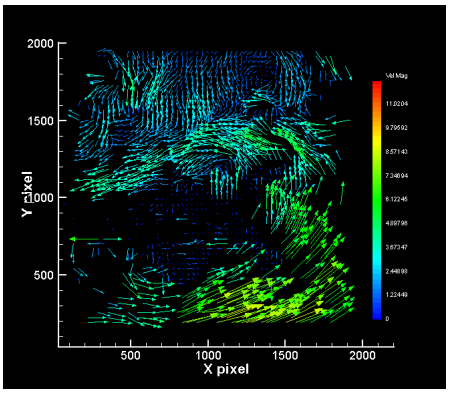

Figure A.2: Additional Vortex Shedding Series 1 at t2

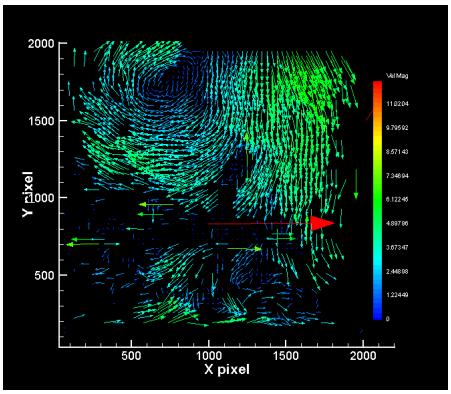

Figure A.3: Additional Vortex Shedding Series 1 at t3

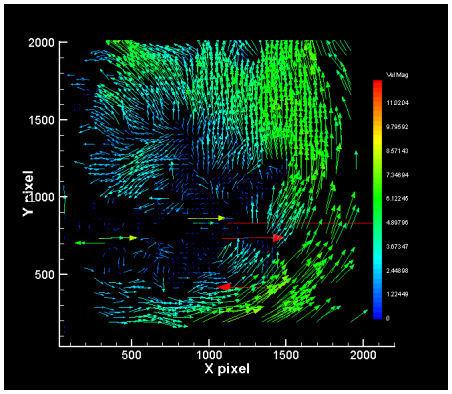

Figure A.4: Additional Vortex Shedding Series 1 at t4

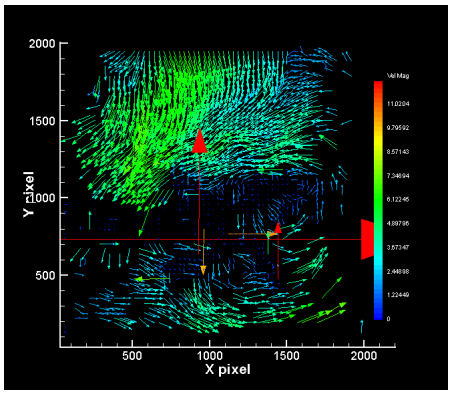

Figure A.5: Additional Vortex Shedding Series 1 at t5

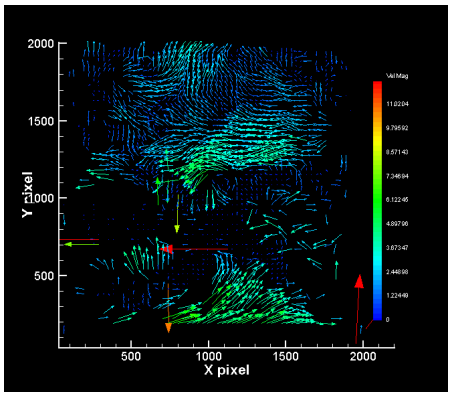

Figure A.6: Additional Vortex Shedding Series 1 at t6

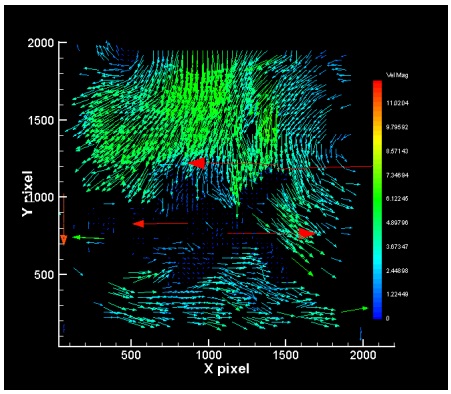

Figure A.7: Additional Vortex Shedding Series 1 at t7

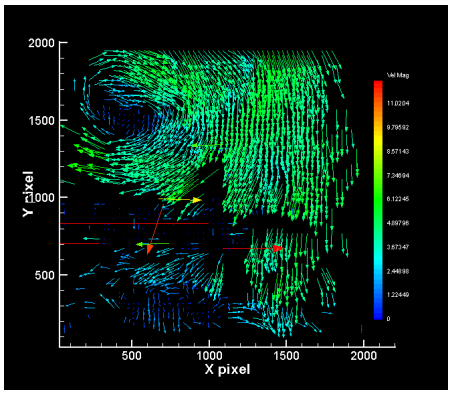

Figure A.8: Additional Vortex Shedding Series 1 at t8

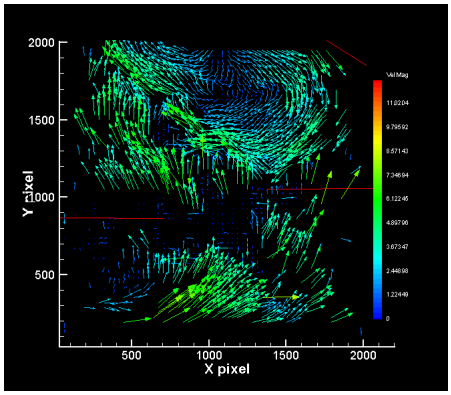

Figure A.9: Additional Vortex Shedding Series 1 at t9

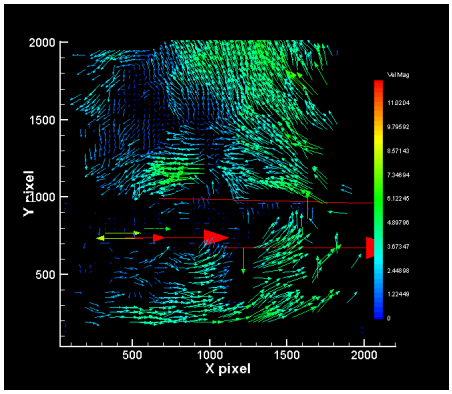

Figure A.10: Additional Vortex Shedding Series 1 at t10

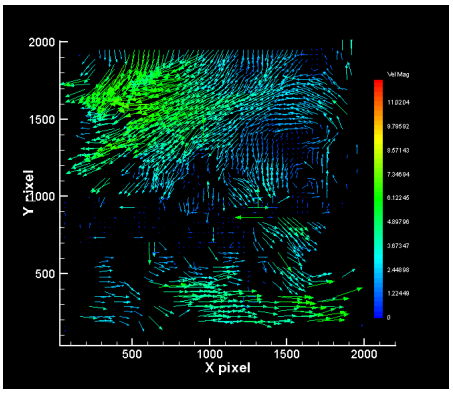

Figure A.11: Additional Vortex Shedding Series 1 at t11

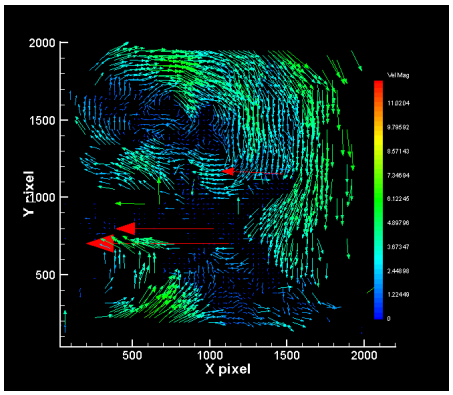

Figure A.12: Additional Vortex Shedding Series 1 at t12

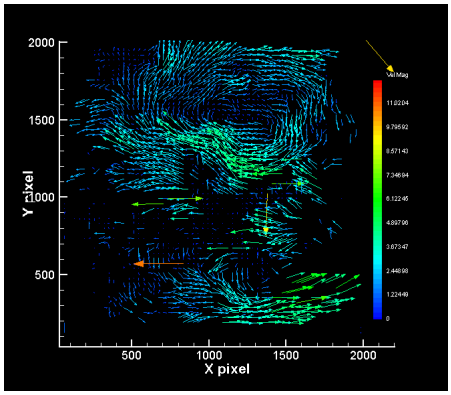

Figure A.13: Additional Vortex Shedding Series 1 at t13

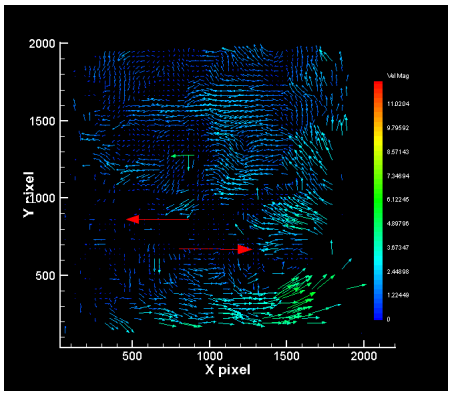

Figure A.14: Additional Vortex Shedding Series 1 at t14

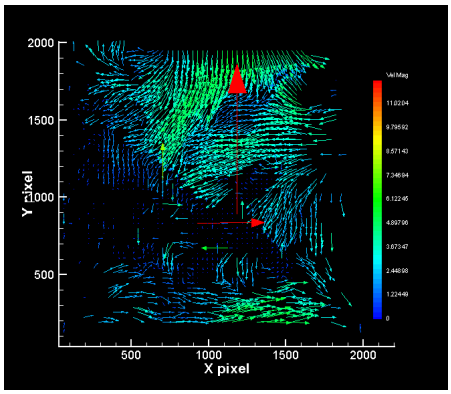

Figure A.15: Additional Vortex Shedding Series 1 at t15

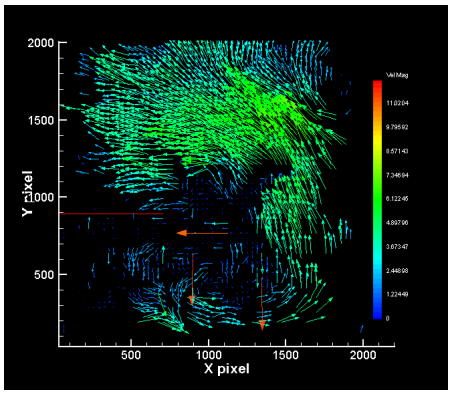

Figure A.16: Additional Vortex Shedding Series 1 at t16

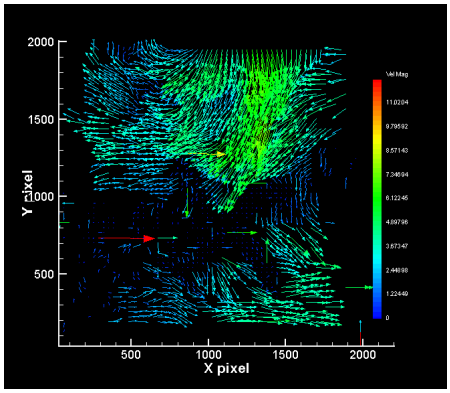

Figure A.17: Additional Vortex Shedding Series 1 at t17

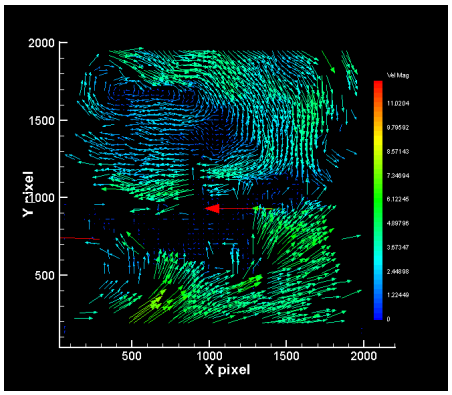

Figure A.18: Additional Vortex Shedding Series 1 at t18

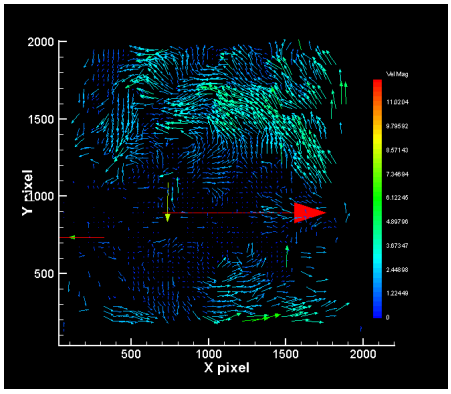

Figure A.19: Additional Vortex Shedding Series 1 at t19

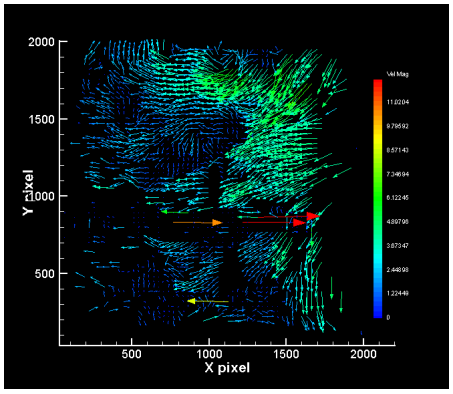

Figure A.20: Additional Vortex Shedding Series 1 at t20

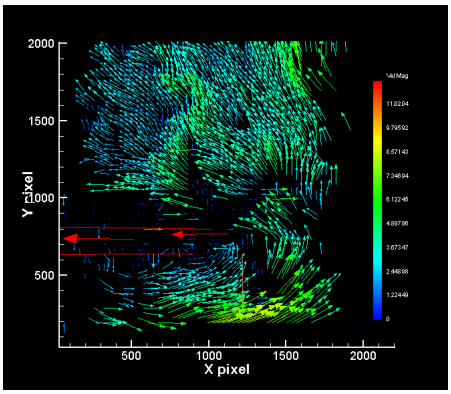

Figure A.21: Additional Vortex Shedding Series 1 at t21

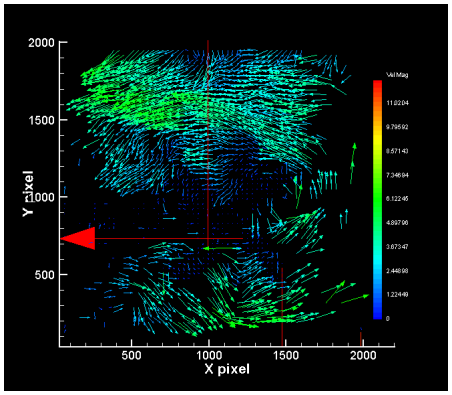

Figure A.22: Additional Vortex Shedding Series 1 at t22

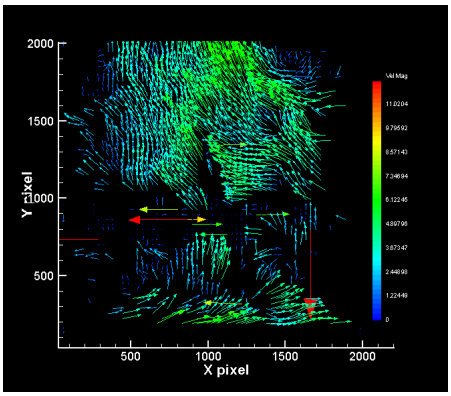

Figure A.23: Additional Vortex Shedding Series 1 at t23

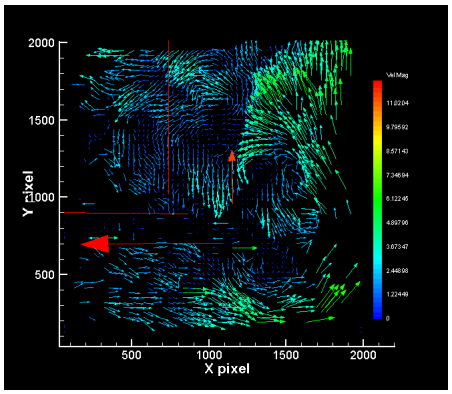

Figure A.24: Additional Vortex Shedding Series 1 at t24

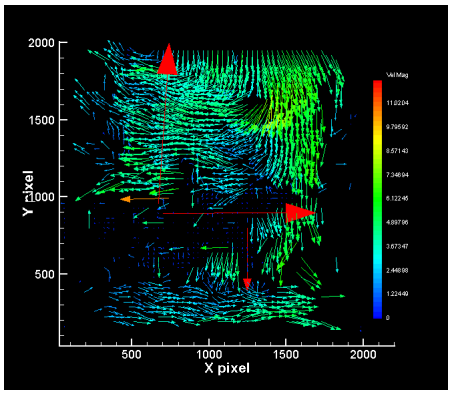

Figure A.25: Additional Vortex Shedding Series 1 at t25

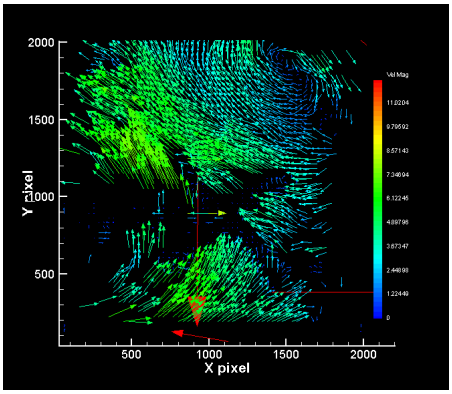

Figure A.26: Additional Vortex Shedding Series 1 at t26

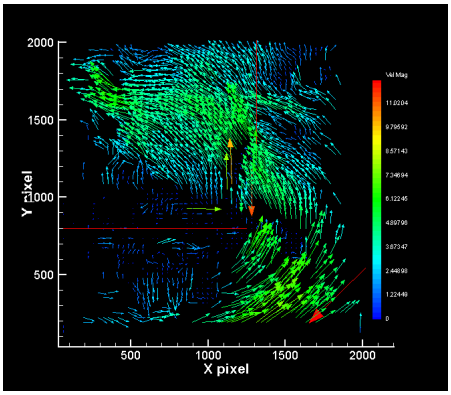

Figure A.27: Additional Vortex Shedding Series 1 at t27

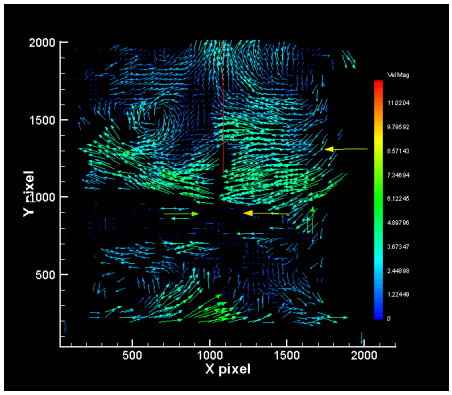

Figure A.28: Additional Vortex Shedding Series 1 at t28

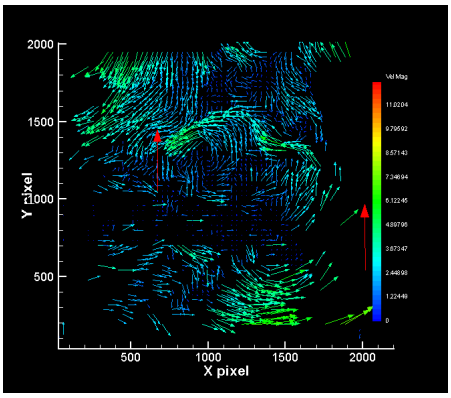

Figure A.29: Additional Vortex Shedding Series 1 at t29

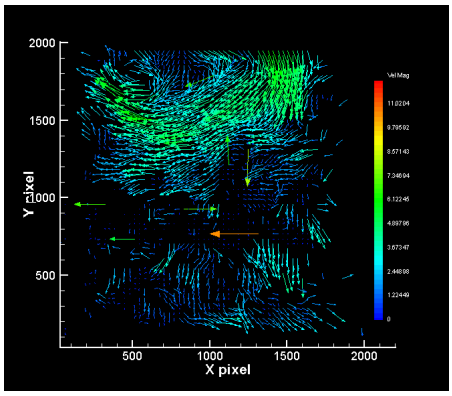

Figure A.30: Additional Vortex Shedding Series 1 at t30

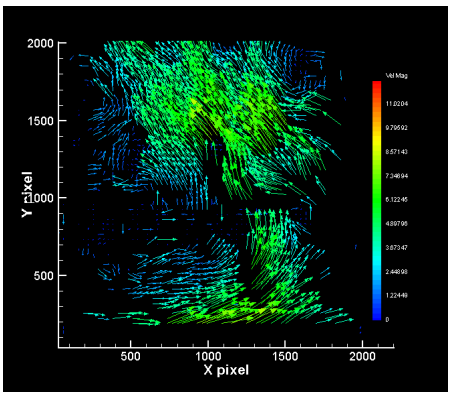

Figure A.31: Additional Vortex Shedding Series 1 at t31

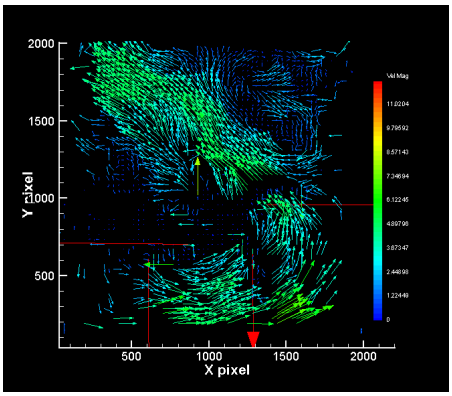

Figure A.32: Additional Vortex Shedding Series 1 at t32

A.2 Additional Vortex Shedding Series 2

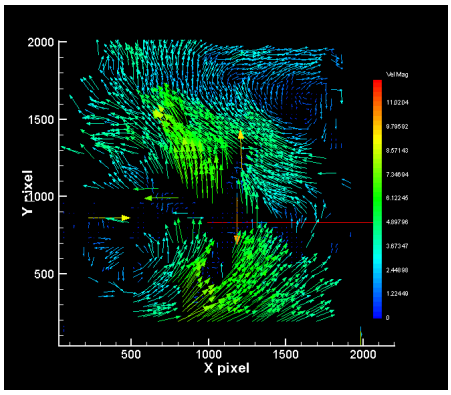

Figure A.33: Additional Vortex Shedding Series 2 at t1

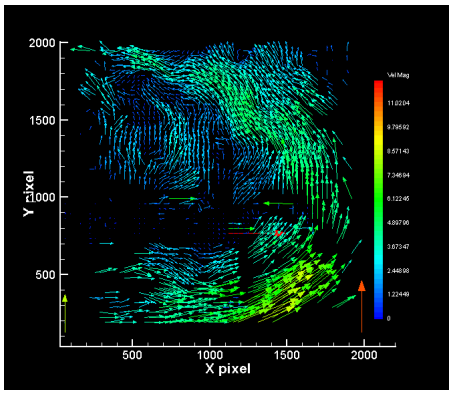

Figure A.34: Additional Vortex Shedding Series 2 at t2

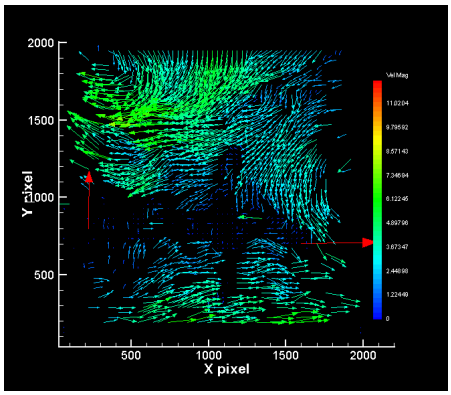

Figure A.35: Additional Vortex Shedding Series 2 at t3

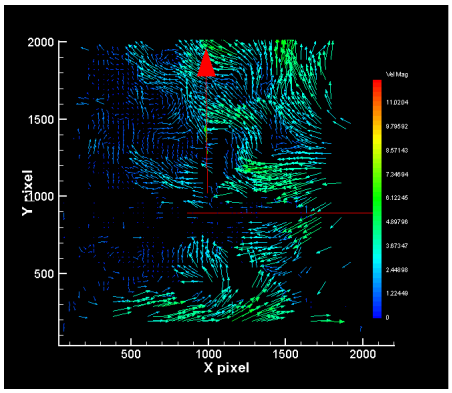

Figure A.36: Additional Vortex Shedding Series 2 at t4

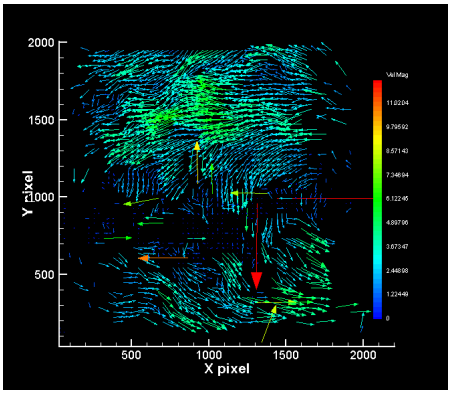

Figure A.37: Additional Vortex Shedding Series 2 at t5

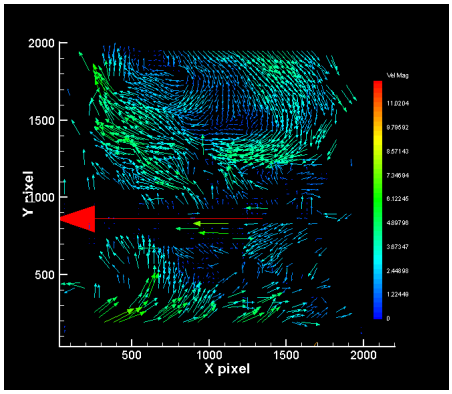

Figure A.38: Additional Vortex Shedding Series 2 at t6

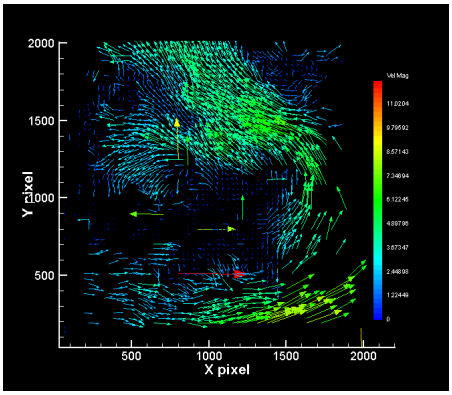

Figure A.39: Additional Vortex Shedding Series 2 at t7

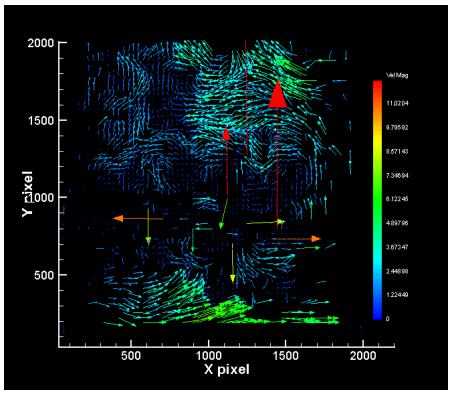

Figure A.40: Additional Vortex Shedding Series 2 at t8

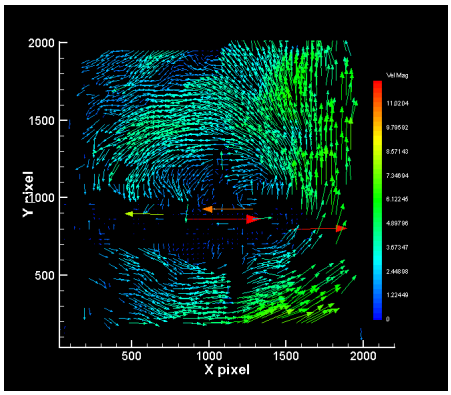

Figure A.41: Additional Vortex Shedding Series 2 at t9

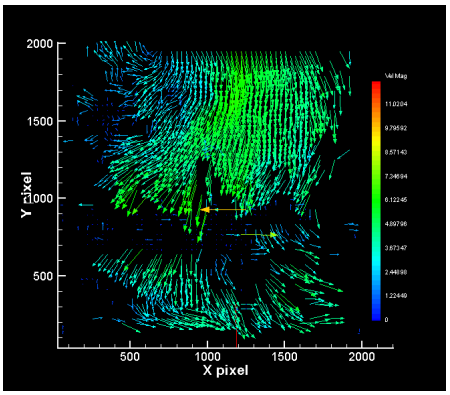

Figure A.42: Additional Vortex Shedding Series 2 at t10

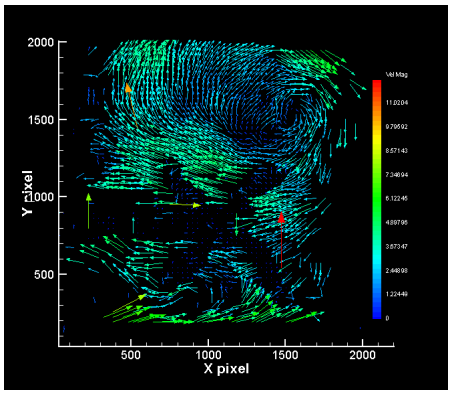

Figure A.43: Additional Vortex Shedding Series 2 at t11

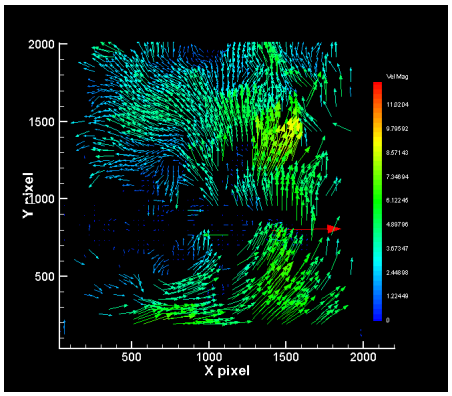

Figure A.44: Additional Vortex Shedding Series 2 at t12

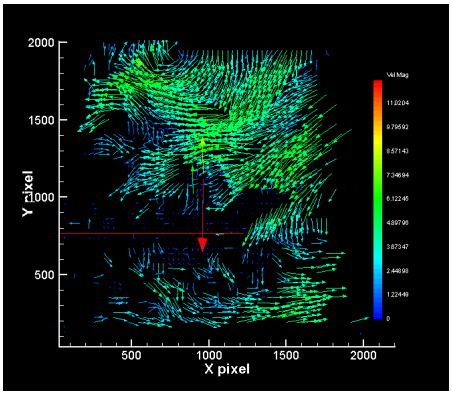

Figure A.45: Additional Vortex Shedding Series 2 at t13

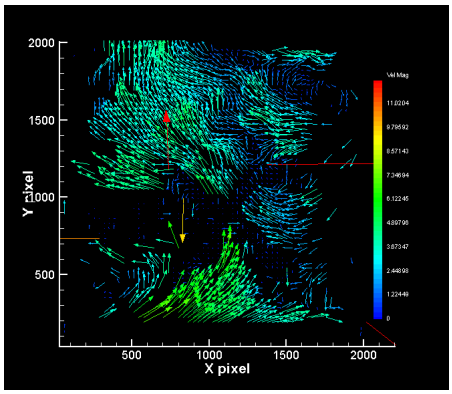

Figure A.46: Additional Vortex Shedding Series 2 at t14

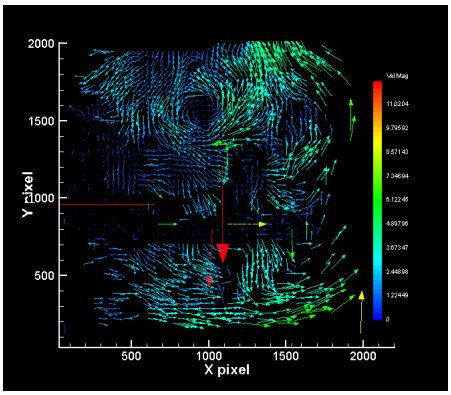

Figure A.47: Additional Vortex Shedding Series 2 at t15

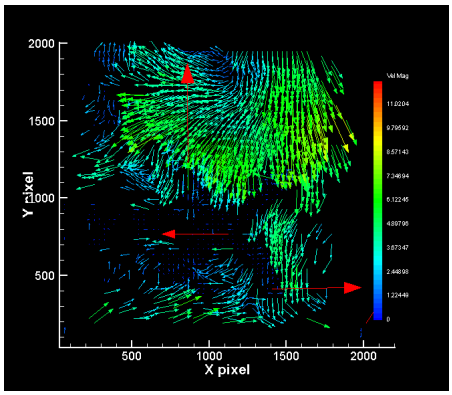

Figure A.48: Additional Vortex Shedding Series 2 at t16

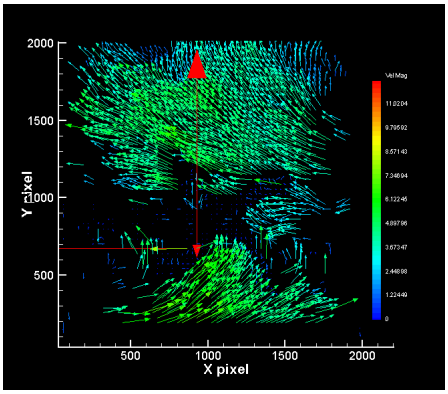

Figure A.49: Additional Vortex Shedding Series 2 at t17

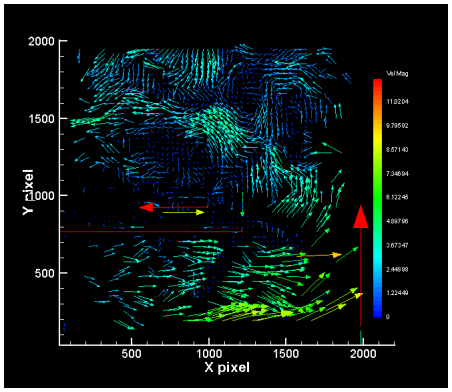

Figure A.50: Additional Vortex Shedding Series 2 at t18

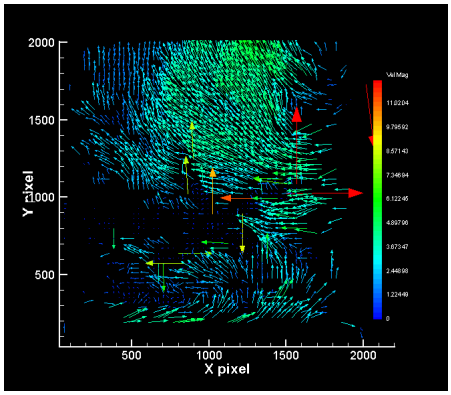

Figure A.51: Additional Vortex Shedding Series 2 at t19

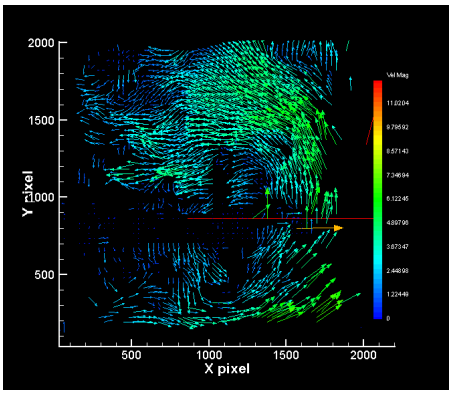

Figure A.52: Additional Vortex Shedding Series 2 at t20

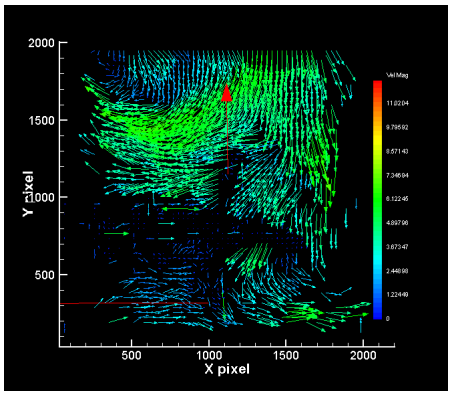

Figure A.53: Additional Vortex Shedding Series 2 at t21

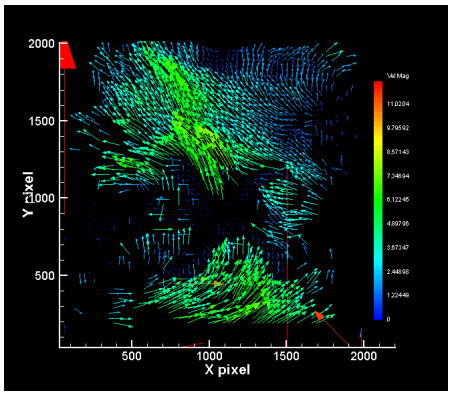

Figure A.54: Additional Vortex Shedding Series 2 at t22

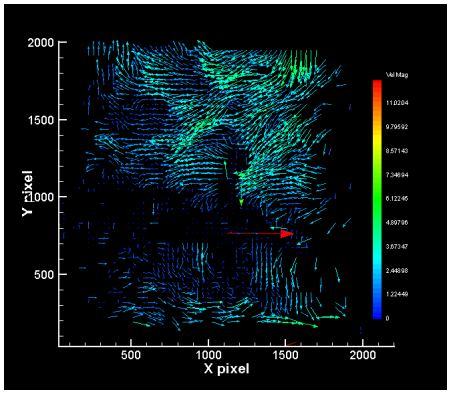

Figure A.55: Additional Vortex Shedding Series 2 at t23

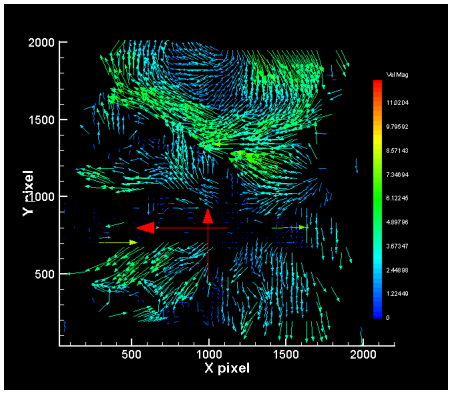

Figure A.56: Additional Vortex Shedding Series 2 at t24

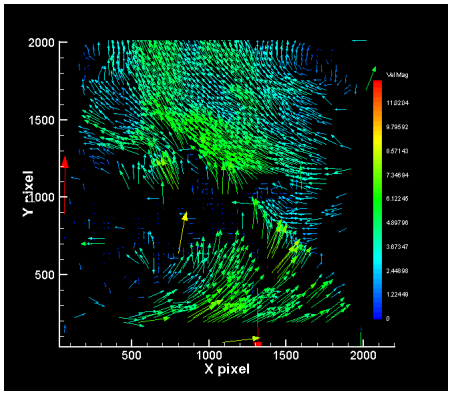

Figure A.57: Additional Vortex Shedding Series 2 at t25

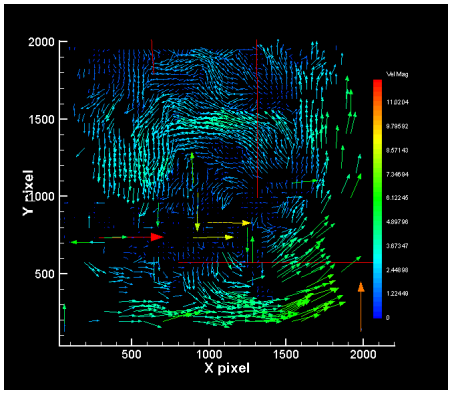

Figure A.58: Additional Vortex Shedding Series 2 at t26

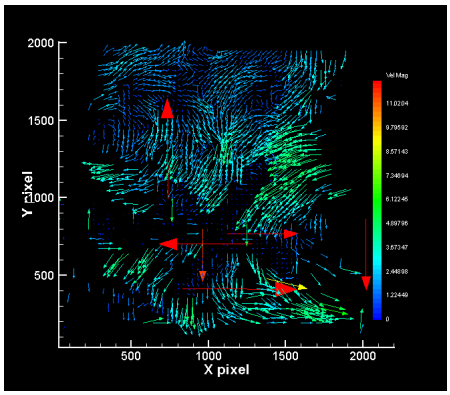

Figure A.59: Additional Vortex Shedding Series 2 at t27

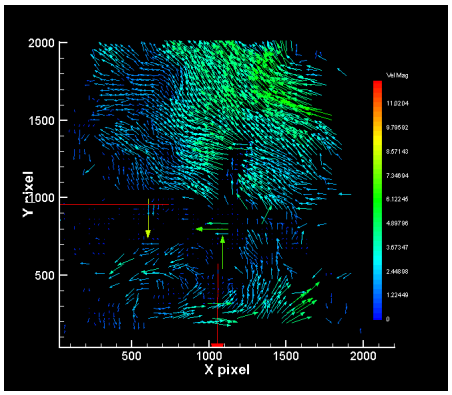

Figure A.60: Additional Vortex Shedding Series 2 at t28

A.3 Additional Vortex Shedding Series 3

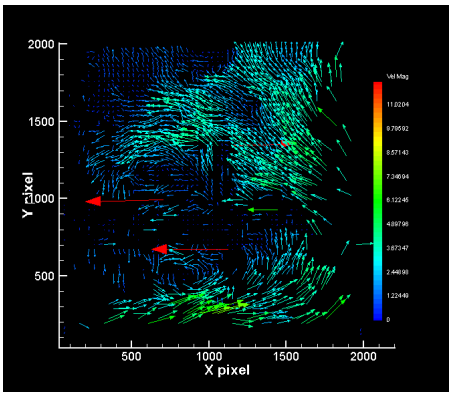

Figure A.61: Additional Vortex Shedding Series 3 at t1

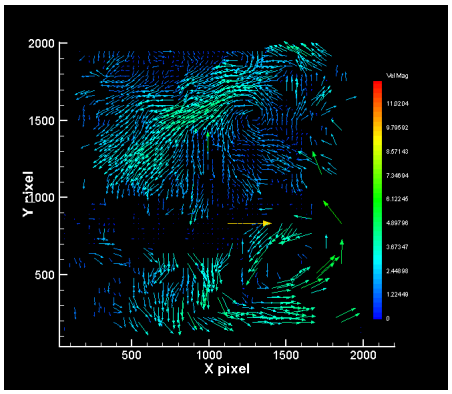

Figure A.62: Additional Vortex Shedding Series 3 at t2

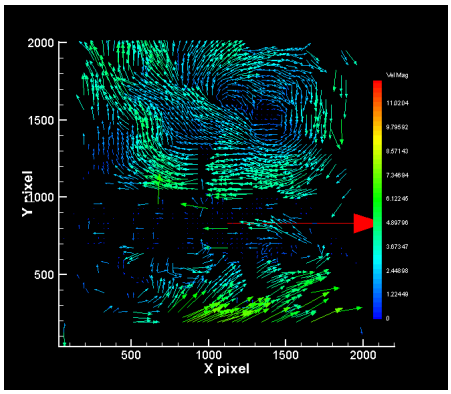

Figure A.63: Additional Vortex Shedding Series 3 at t3

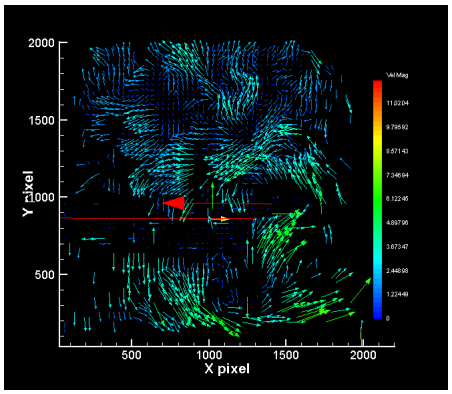

Figure A.64: Additional Vortex Shedding Series 3 at t4

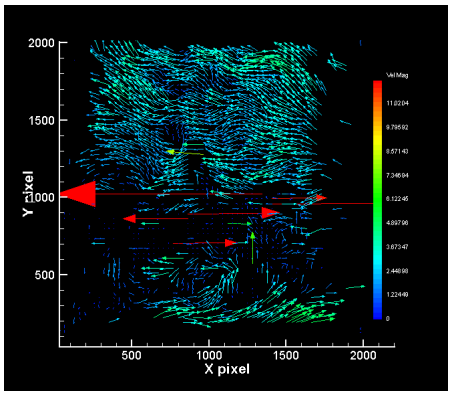

Figure A.65: Additional Vortex Shedding Series 3 at t5

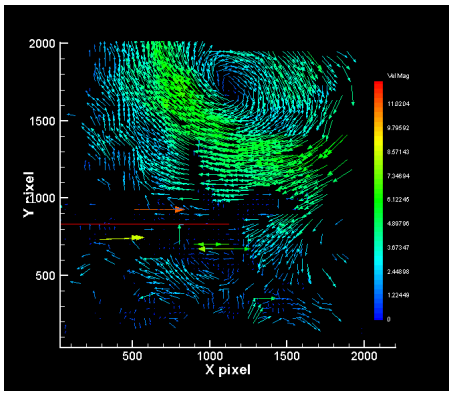

Figure A.66: Additional Vortex Shedding Series 3 at t6

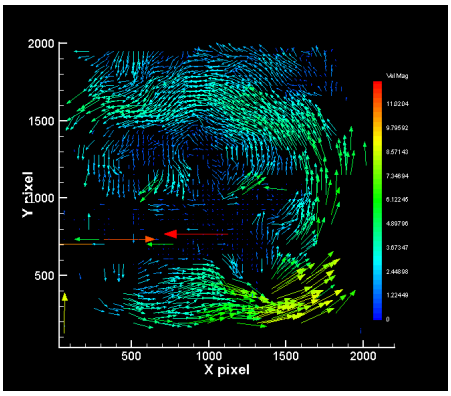

Figure A.67: Additional Vortex Shedding Series 3 at t7

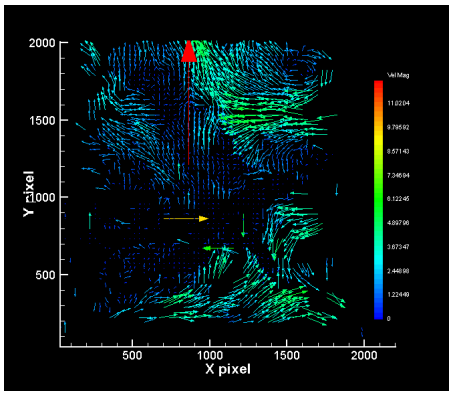

Figure A.68: Additional Vortex Shedding Series 3 at t8

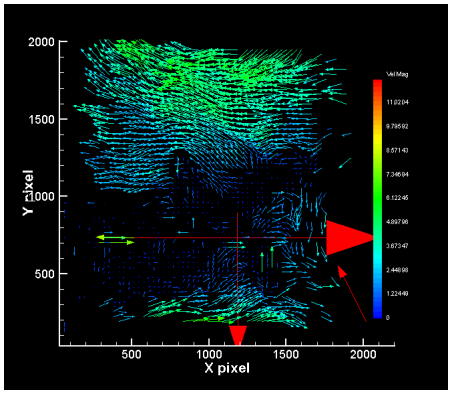

Figure A.69: Additional Vortex Shedding Series 3 at t9

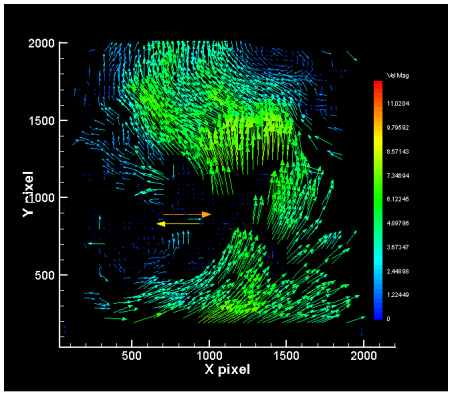

Figure A.70: Additional Vortex Shedding Series 3 at t10

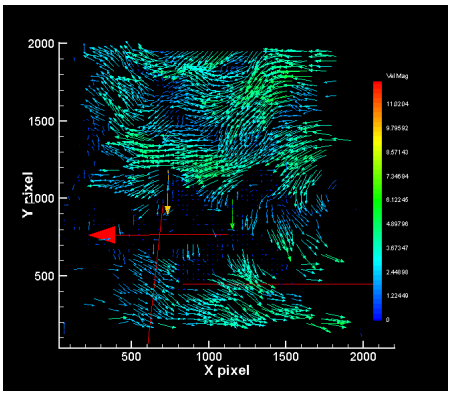

Figure A.71: Additional Vortex Shedding Series 3 at t11

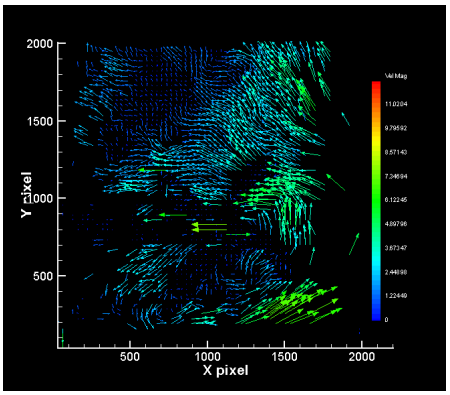

Figure A.72: Additional Vortex Shedding Series 3 at t12

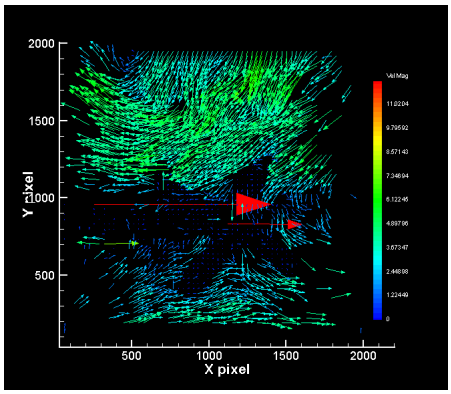

Figure A.73: Additional Vortex Shedding Series 3 at t13

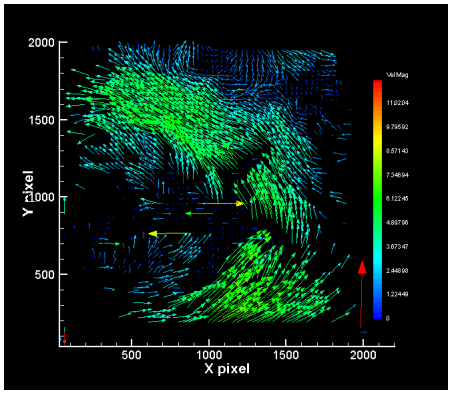

Figure A.74: Additional Vortex Shedding Series 3 at t14

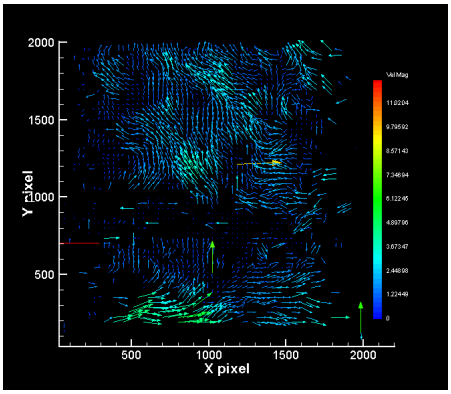

Figure A.75: Additional Vortex Shedding Series 3 at t15

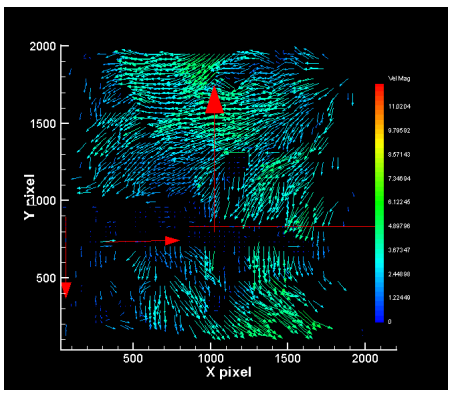

Figure A.76: Additional Vortex Shedding Series 3 at t16

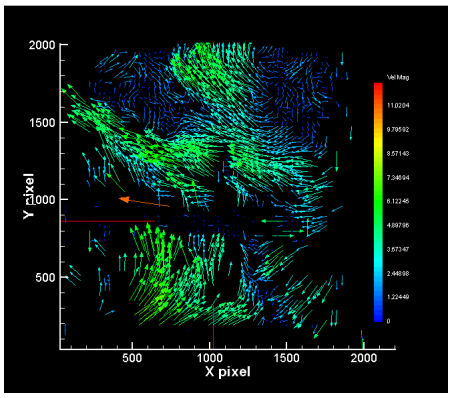

Figure A.77: Additional Vortex Shedding Series 3 at t17

A.4 Additional Vortex Shedding Series 4

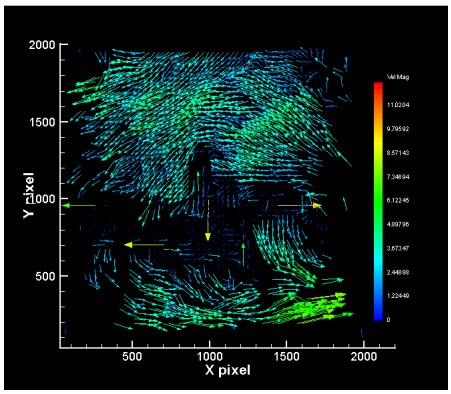

Figure A.78: Additional Vortex Shedding Series 4 at t1

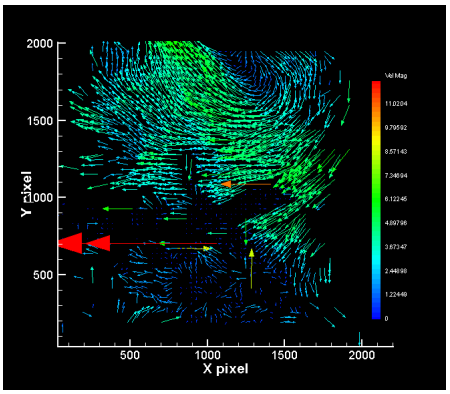

Figure A.79: Additional Vortex Shedding Series 4 at t2

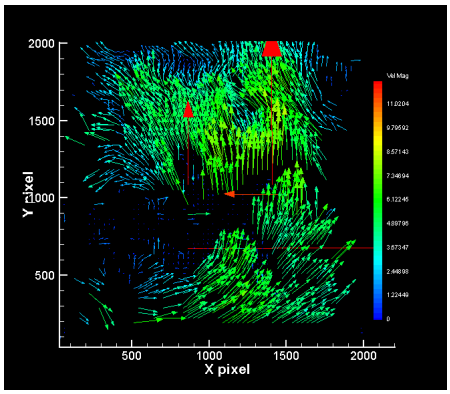

Figure A.80: Additional Vortex Shedding Series 4 at t3

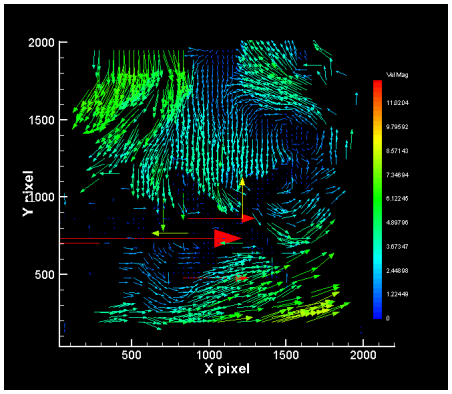

Figure A.81: Additional Vortex Shedding Series 4 at t4

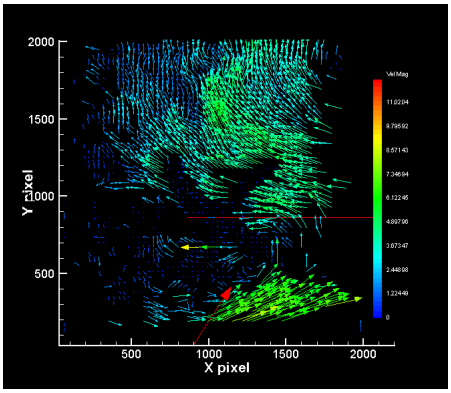

Figure A.82: Additional Vortex Shedding Series 4 at t5

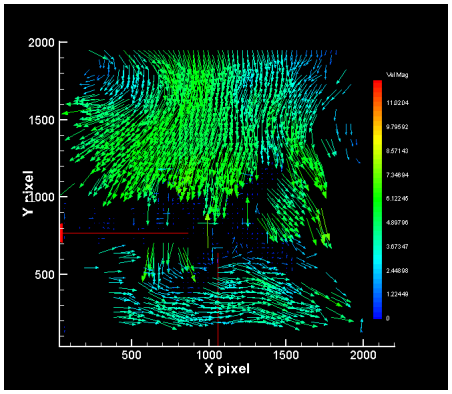

Figure A.83: Additional Vortex Shedding Series 4 at t6

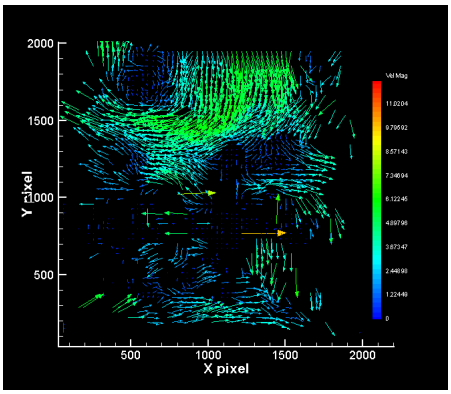

Figure A.84: Additional Vortex Shedding Series 4 at t7

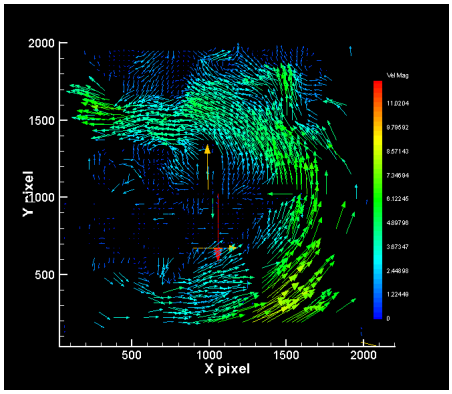

Figure A.85: Additional Vortex Shedding Series 4 at t8

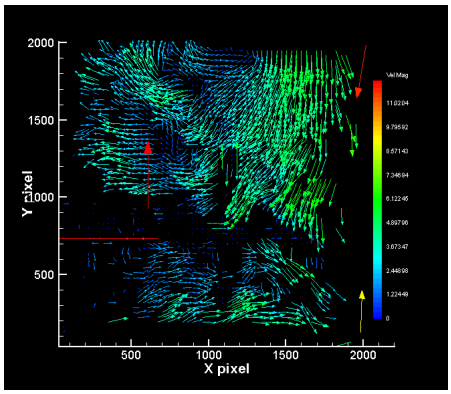

Figure A.86: Additional Vortex Shedding Series 4 at t9

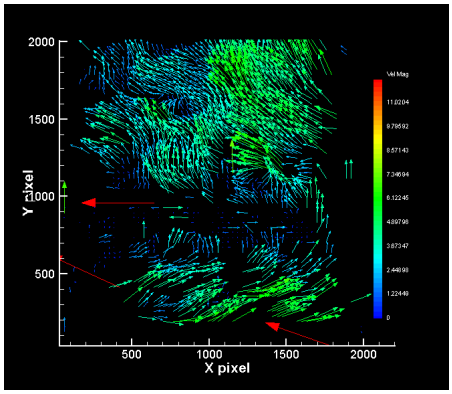

Figure A.87: Additional Vortex Shedding Series 4 at t10

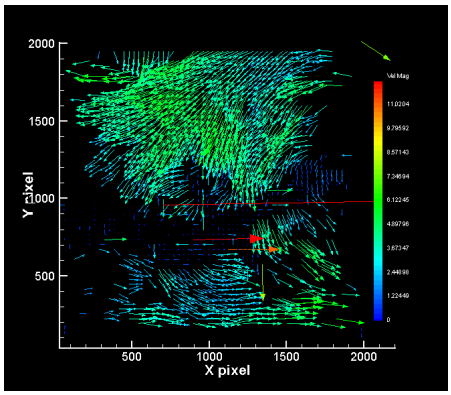

Figure A.88: Additional Vortex Shedding Series 4 at t11

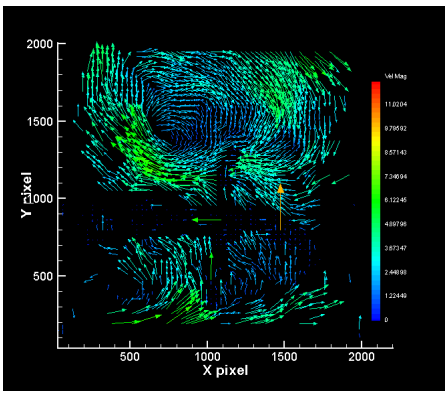

Figure A.89: Additional Vortex Shedding Series 4 at t12

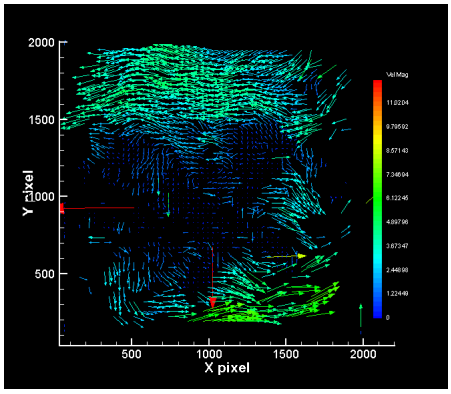

Figure A.90: Additional Vortex Shedding Series 4 at t13

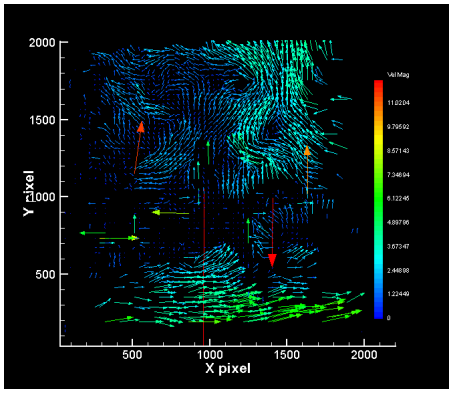

Figure A.91: Additional Vortex Shedding Series 4 at t14

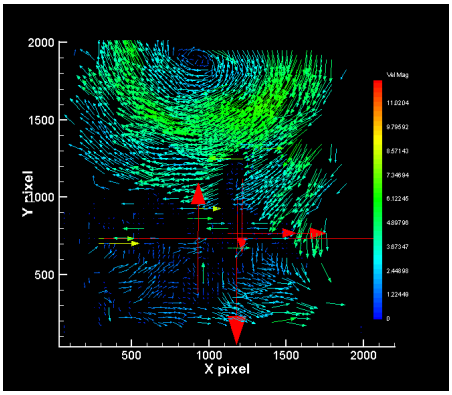

Figure A.92: Additional Vortex Shedding Series 4 at t15

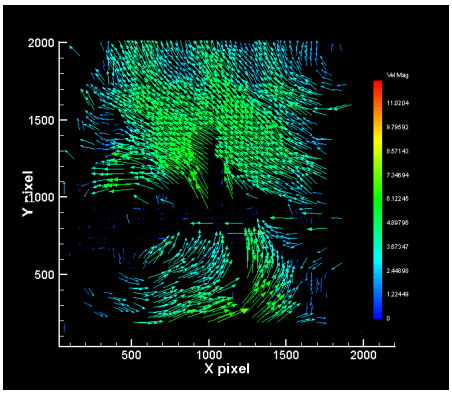

Figure A.93: Additional Vortex Shedding Series 4 at t16

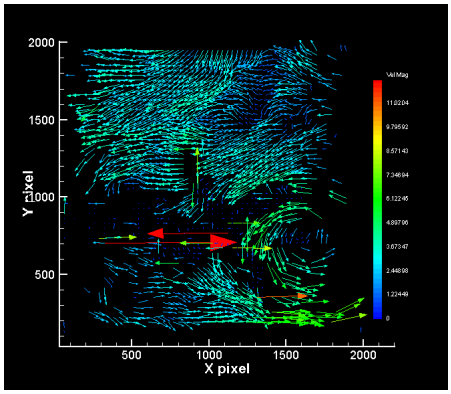

Figure A.94: Additional Vortex Shedding Series 4 at t17

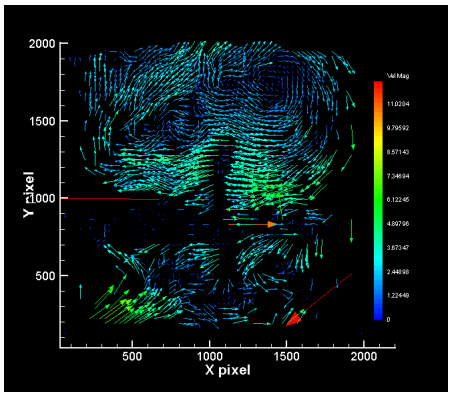

Figure A.95: Additional Vortex Shedding Series 4 at t18

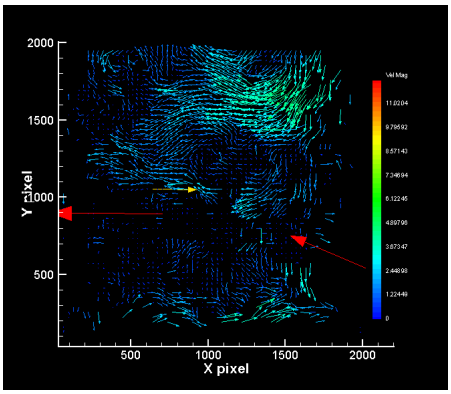

Figure A.96: Additional Vortex Shedding Series 4 at t19

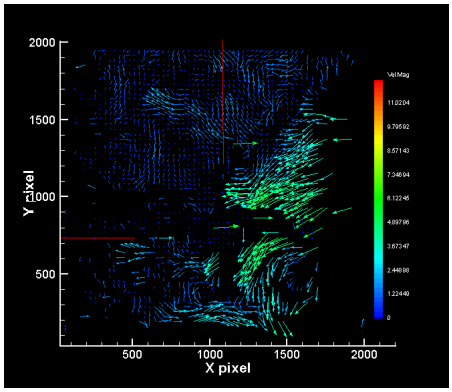

Figure A.97: Additional Vortex Shedding Series 4 at t20

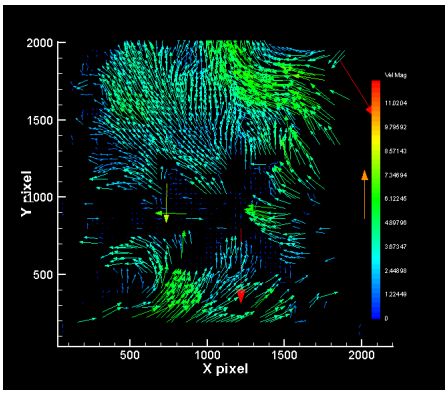

Figure A.98: Additional Vortex Shedding Series 4 at t21

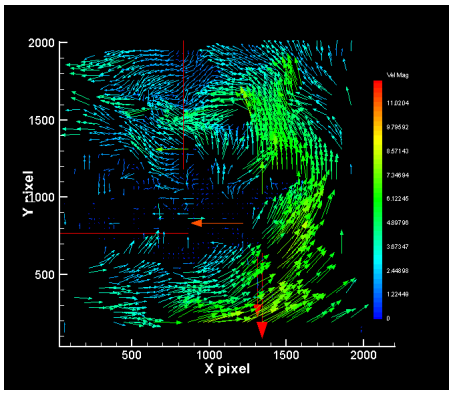

Figure A.99: Additional Vortex Shedding Series 4 at t22

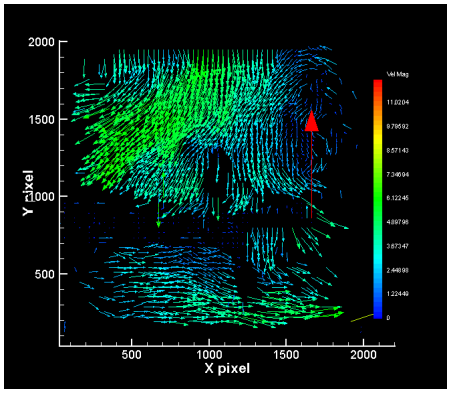

Figure A.100: Additional Vortex Shedding Series 4 at t23

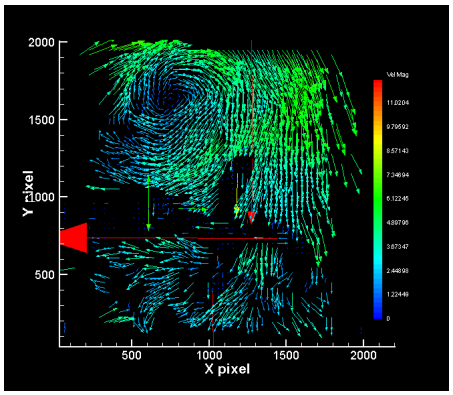

Figure A.101: Additional Vortex Shedding Series 4 at t24

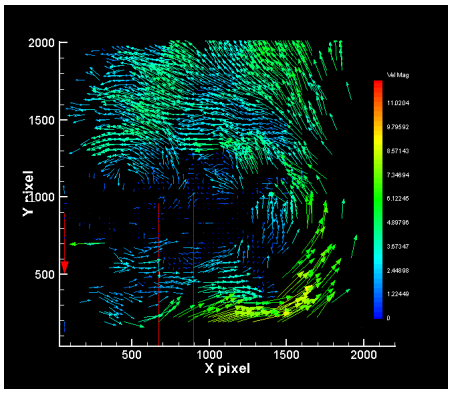

Figure A.102: Additional Vortex Shedding Series 4 at t25

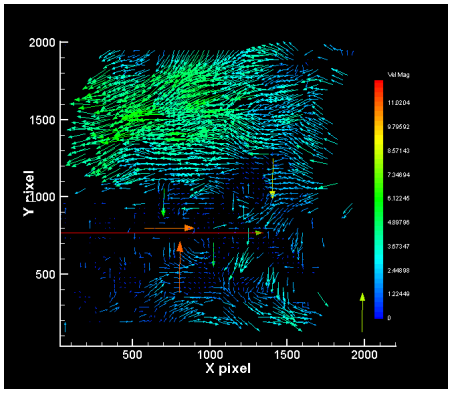

Figure A.103: Additional Vortex Shedding Series 4 at t26

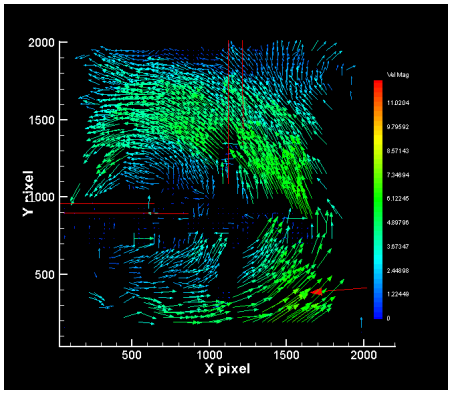

Figure A.104: Additional Vortex Shedding Series 4 at t27

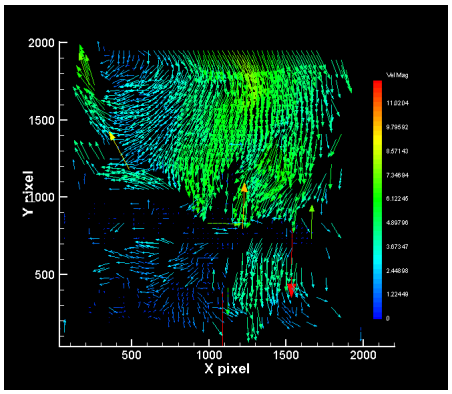

Figure A.105: Additional Vortex Shedding Series 4 at t28

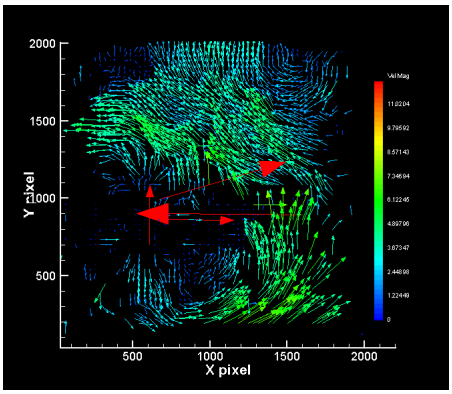

Figure A.106: Additional Vortex Shedding Series 3 at t29

A.5 Additional Vortex Shedding Series 5

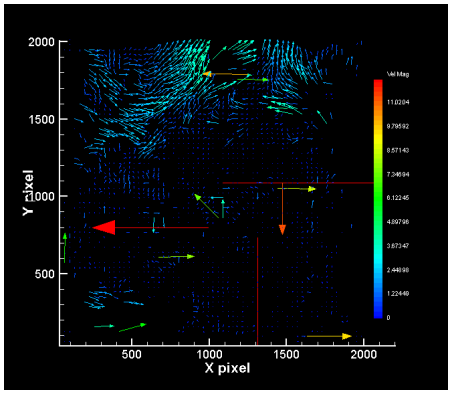

Figure A.107: Additional Vortex Shedding Series 5 at t1

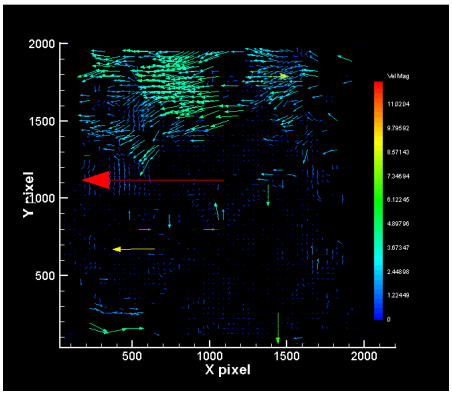

Figure A.108: Additional Vortex Shedding Series 5 at t2

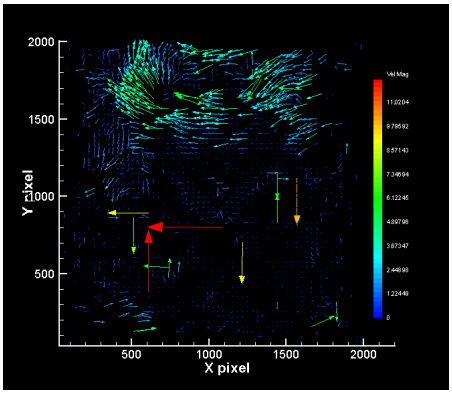

Figure A.109: Additional Vortex Shedding Series 5 at t3

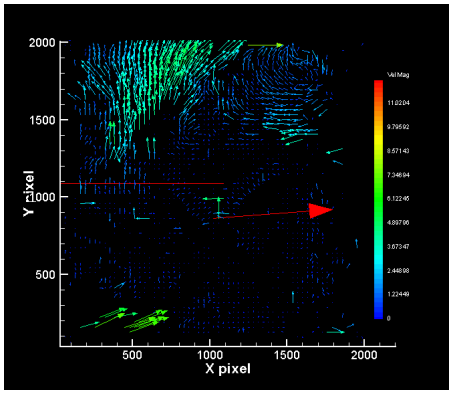

Figure A.110: Additional Vortex Shedding Series 5 at t4

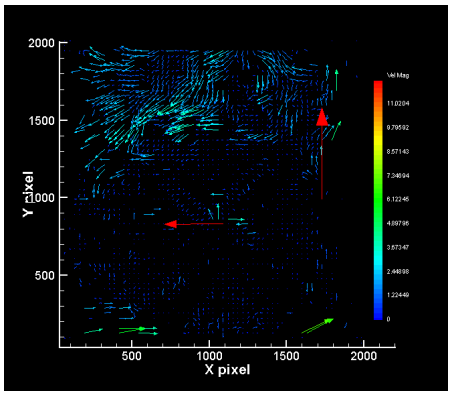

Figure A.111: Additional Vortex Shedding Series 5 at t5

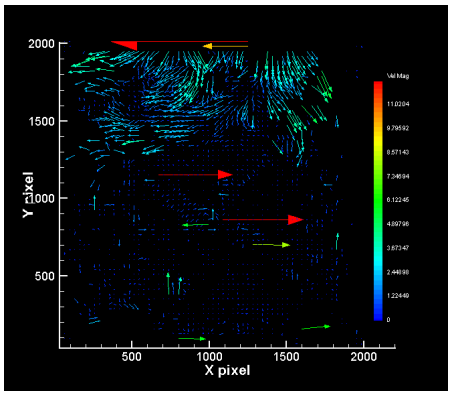

Figure A.112: Additional Vortex Shedding Series 5 at t6

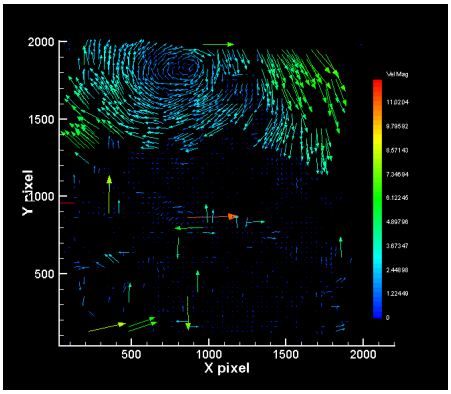

Figure A.113: Additional Vortex Shedding Series 5 at t7

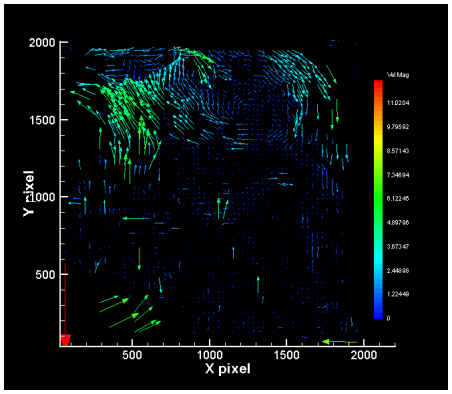

Figure A.114: Additional Vortex Shedding Series 5 at t8

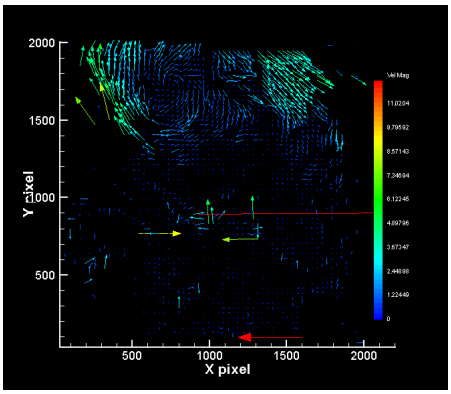

Figure A.115: Additional Vortex Shedding Series 5 at t9

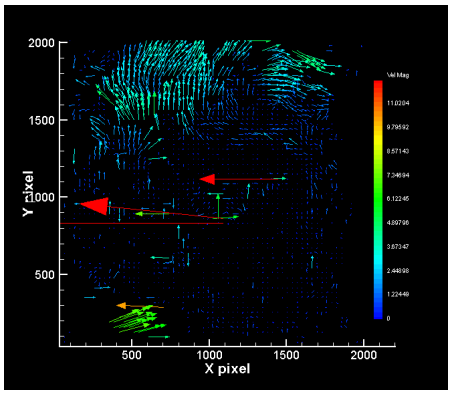

Figure A.116: Additional Vortex Shedding Series 5 at t10

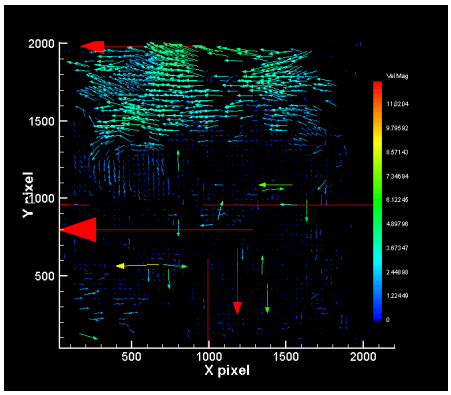

Figure A.117: Additional Vortex Shedding Series 5 at t11

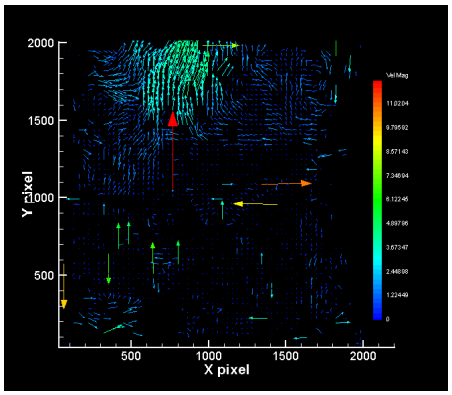

Figure A.118: Additional Vortex Shedding Series 5 at t12

A.6 Additional Vortex Shedding Series 6

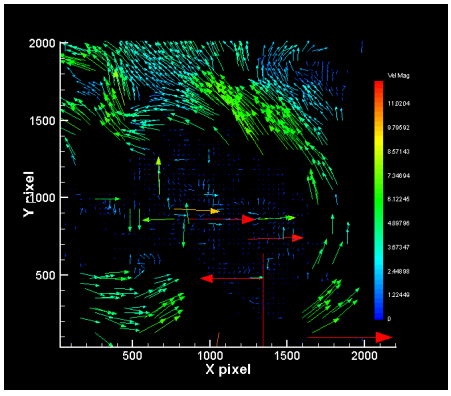

Figure A.119: Additional Vortex Shedding Series 6 at t1

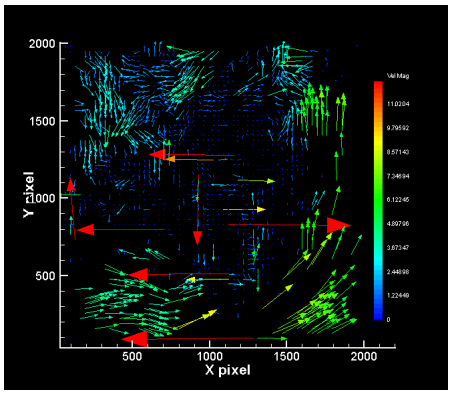

Figure A.120: Additional Vortex Shedding Series 6 at t2

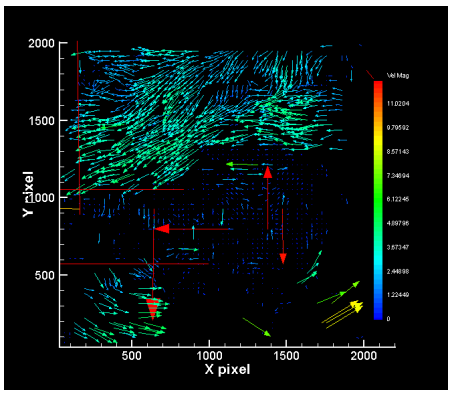

Figure A.121: Additional Vortex Shedding Series 6 at t3

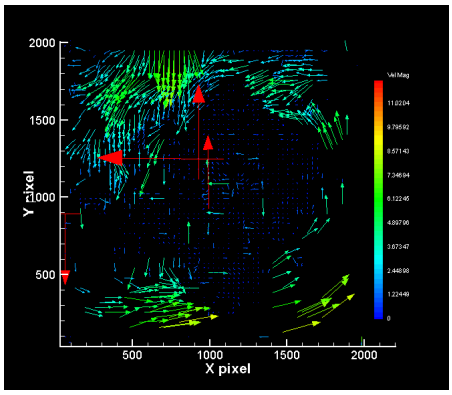

Figure A.122: Additional Vortex Shedding Series 6 at t4

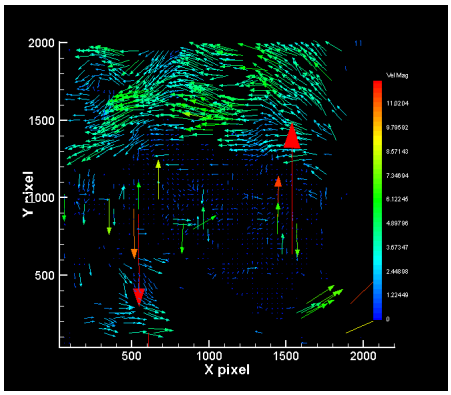

Figure A.123: Additional Vortex Shedding Series 6 at t5

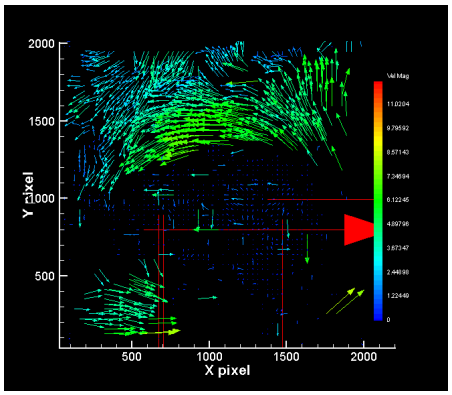

Figure A.124: Additional Vortex Shedding Series 6 at t6

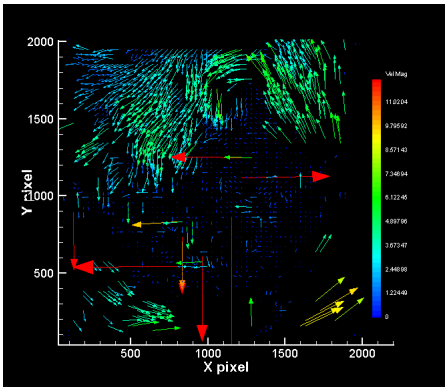

Figure A.125: Additional Vortex Shedding Series 6 at t7

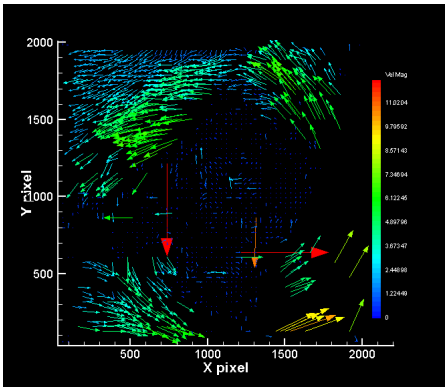

Figure A.126: Additional Vortex Shedding Series 6 at t8

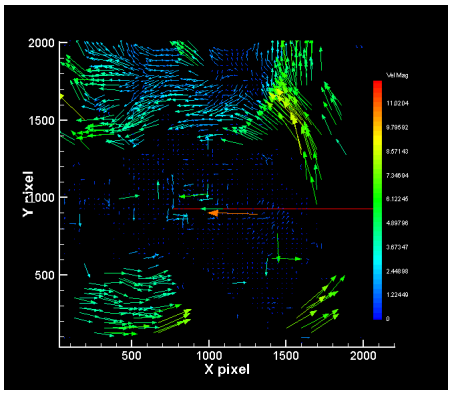

Figure A.127: Additional Vortex Shedding Series 6 at t9

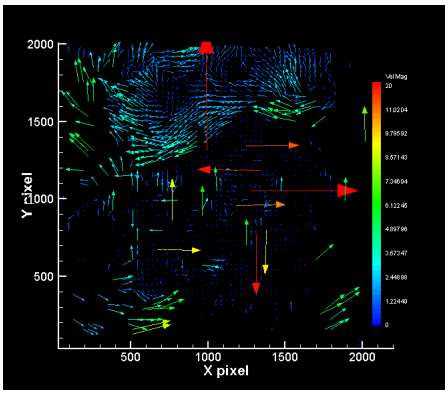

Figure A.128: Additional Vortex Shedding Series 6 at t10

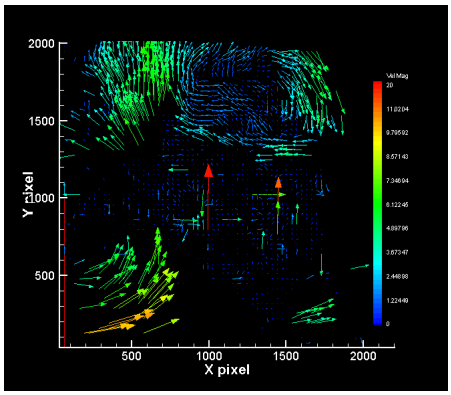

Figure A.129: Additional Vortex Shedding Series 6 at t11

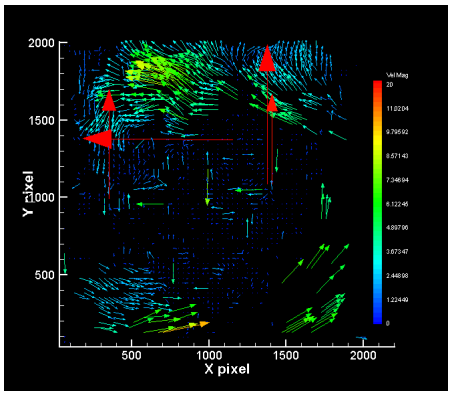

Figure A.130: Additional Vortex Shedding Series 6 at t12

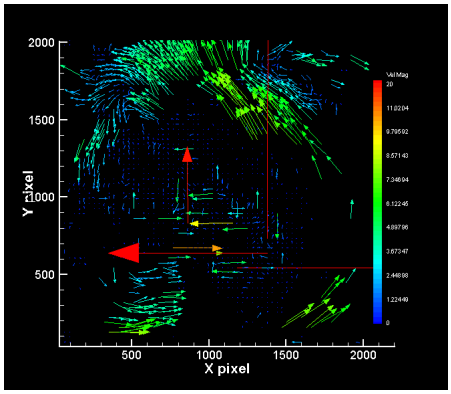

Figure A.131: Additional Vortex Shedding Series 6 at t13

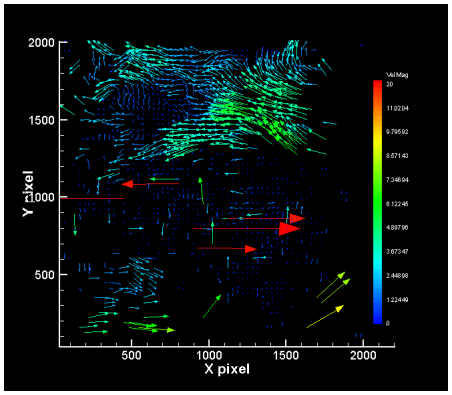

Figure A.132: Additional Vortex Shedding Series 6 at t14

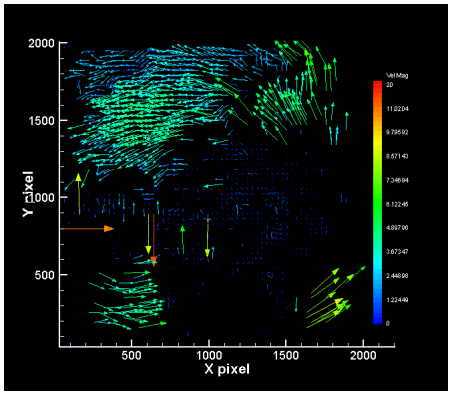

Figure A.133: Additional Vortex Shedding Series 6 at t15

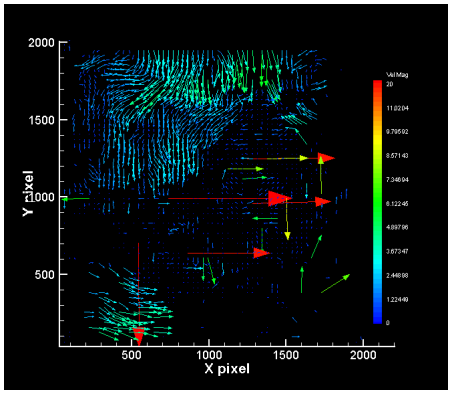

Figure A.134: Additional Vortex Shedding Series 6 at t16

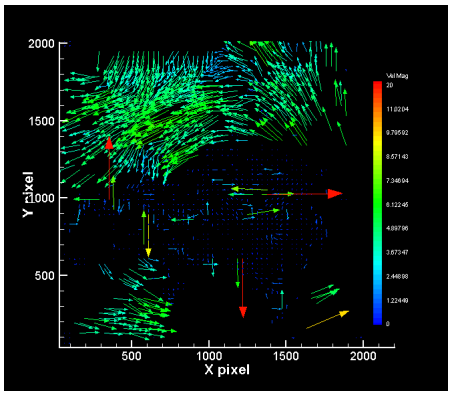

Figure A.135: Additional Vortex Shedding Series 6 at t17

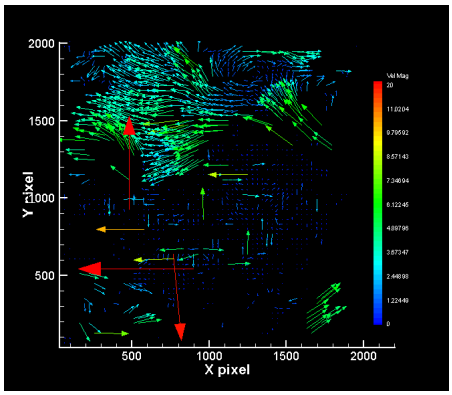

Figure A.136: Additional Vortex Shedding Series 6 at t18

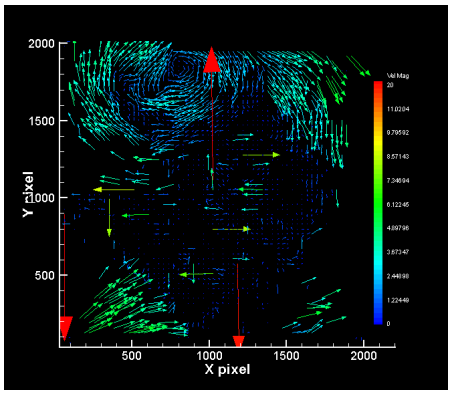

Figure A.137: Additional Vortex Shedding Series 6 at t19

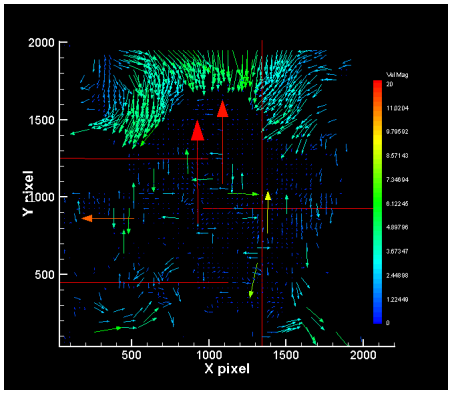

Figure A.138: Additional Vortex Shedding Series 6 at t20

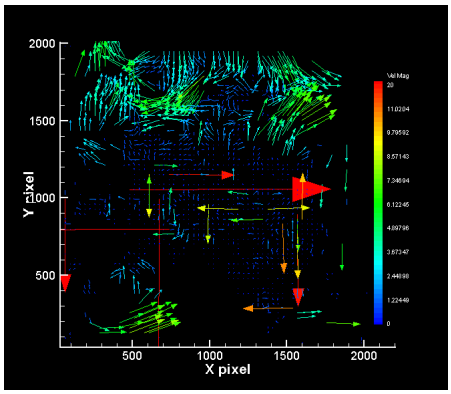

Figure A.139: Additional Vortex Shedding Series 6 at t21

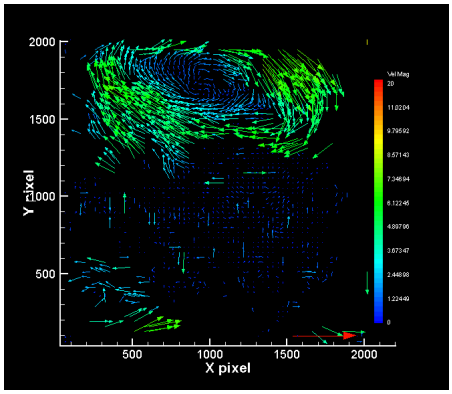

Figure A.140: Additional Vortex Shedding Series 6 at t22

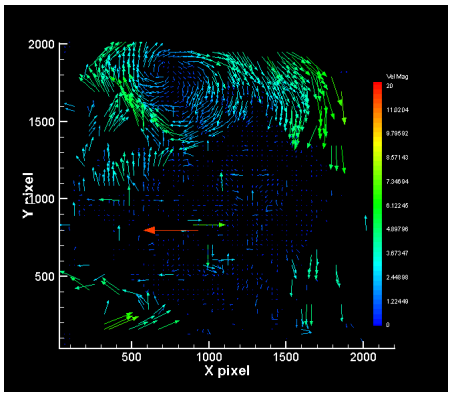

Figure A.141: Additional Vortex Shedding Series 6 at t23

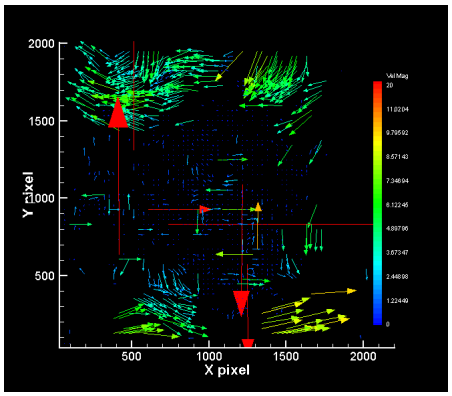

Figure A.142: Additional Vortex Shedding Series 6 at t24

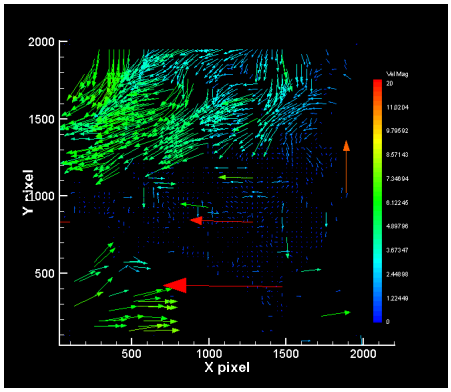

Figure A.143: Additional Vortex Shedding Series 6 at t25

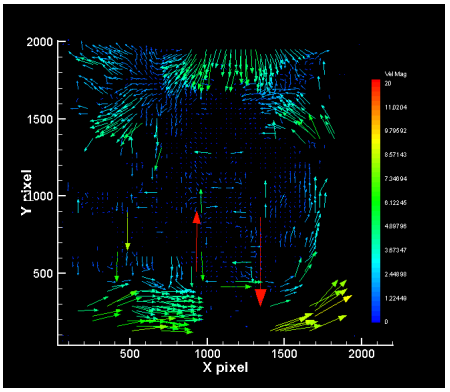

Figure A.144: Additional Vortex Shedding Series 6 at t26

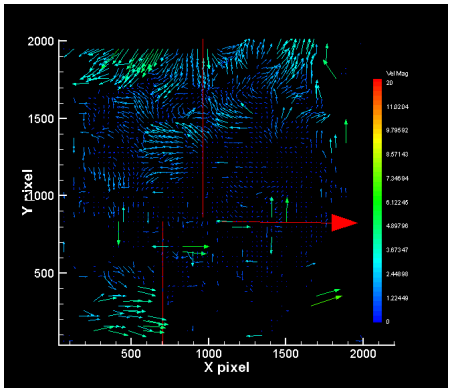

Figure A.145: Additional Vortex Shedding Series 6 at t27

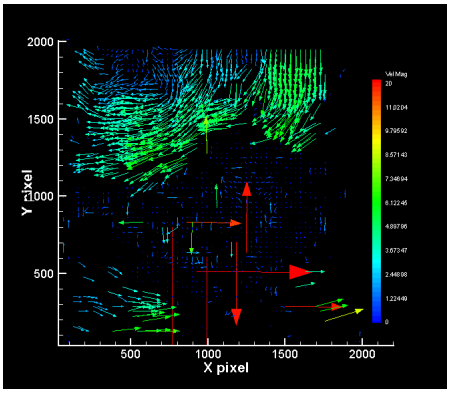

Figure A.146: Additional Vortex Shedding Series 6 at t28

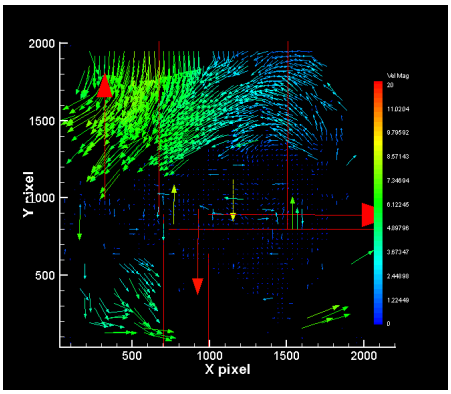

Figure A.147: Additional Vortex Shedding Series 6 at t29

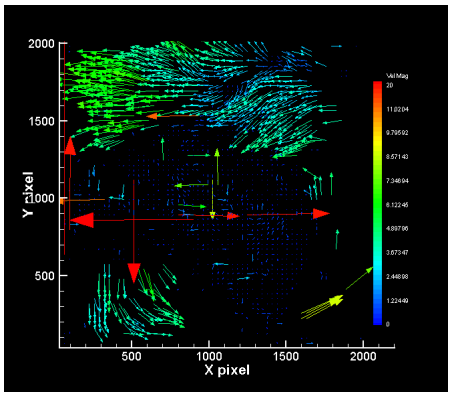

Figure A.148: Additional Vortex Shedding Series 6 at t30

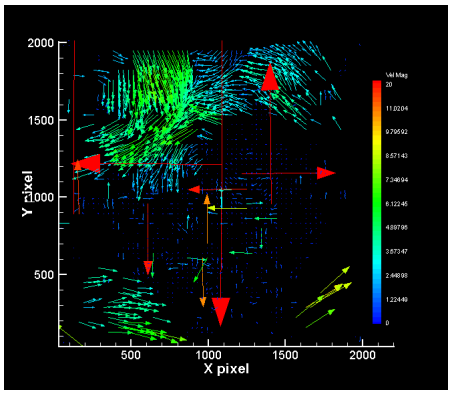

Figure A.149: Additional Vortex Shedding Series 6 at t31

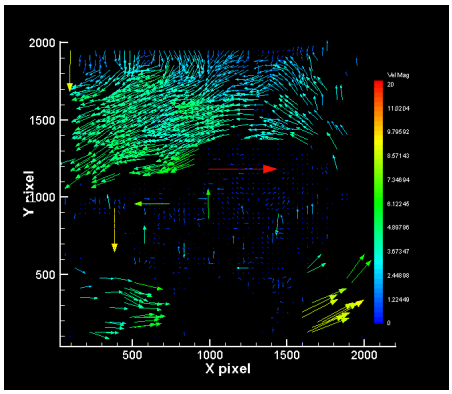

Figure A.150: Additional Vortex Shedding Series 6 at t32

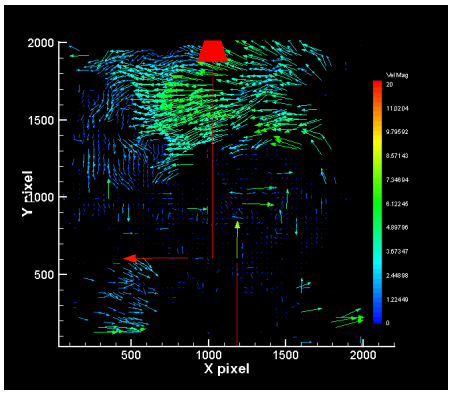

Figure A.151: Additional Vortex Shedding Series 6 at t33

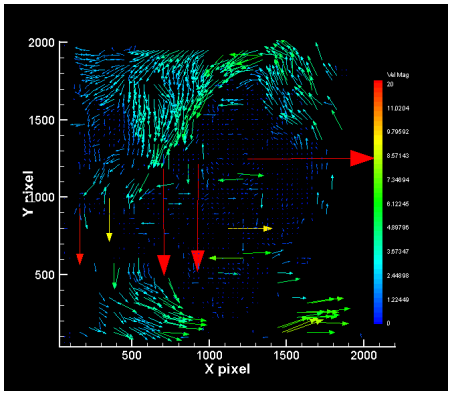

Figure A.152: Additional Vortex Shedding Series 6 at t34

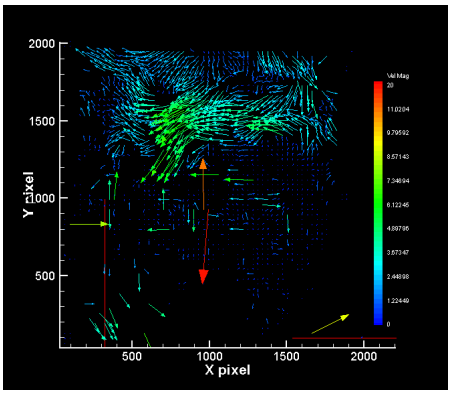

Figure A.153: Additional Vortex Shedding Series 6 at t35

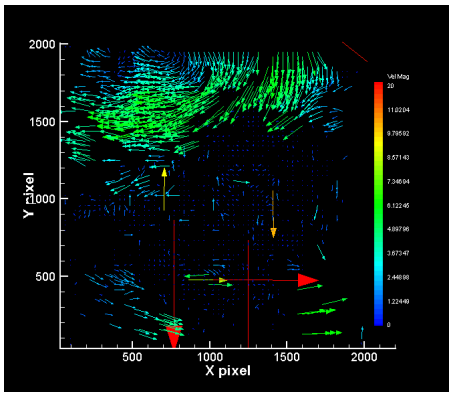

Figure A.154: Additional Vortex Shedding Series 6 at t36

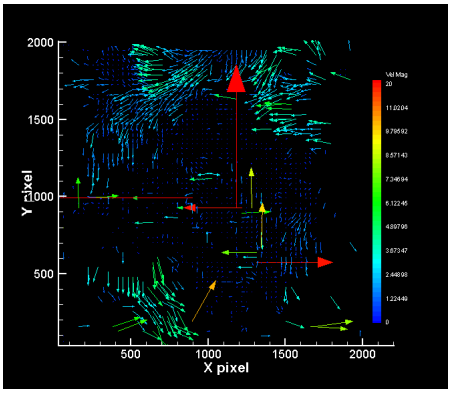

Figure A.155: Additional Vortex Shedding Series 6 at t38

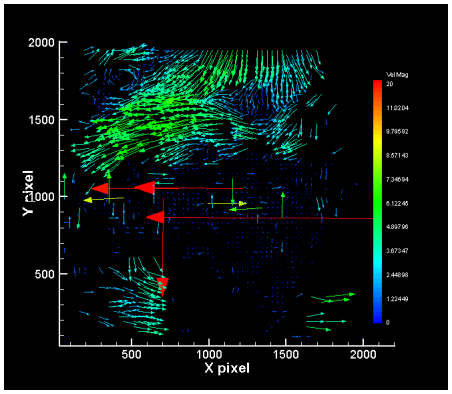

Figure A.156: Additional Vortex Shedding Series 6 at t39

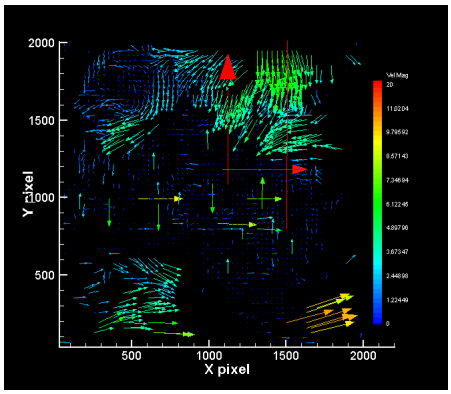

Figure A.157: Additional Vortex Shedding Series 6 at t40

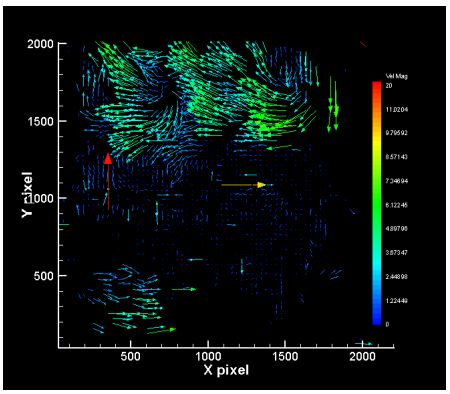

Figure A.158: Additional Vortex Shedding Series 6 at t41

A.7 Additional Vortex Shedding Series 7

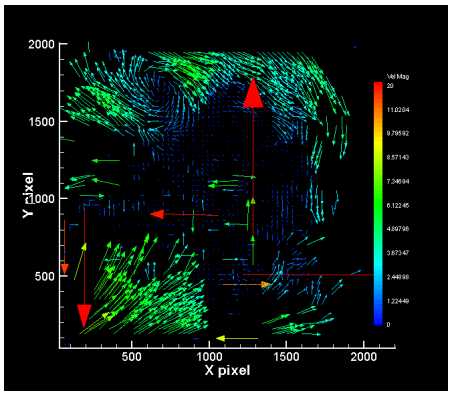

Figure A.159: Additional Vortex Shedding Series 7 at t1

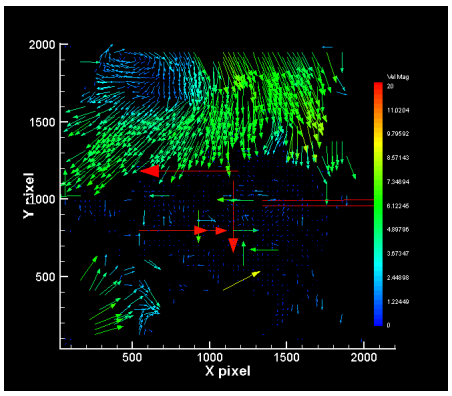

Figure A.160: Additional Vortex Shedding Series 7 at t2

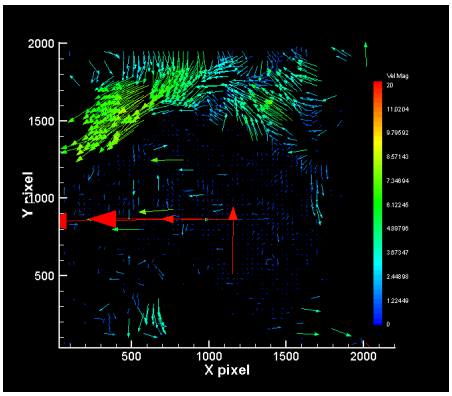

Figure A.161: Additional Vortex Shedding Series 7 at t3

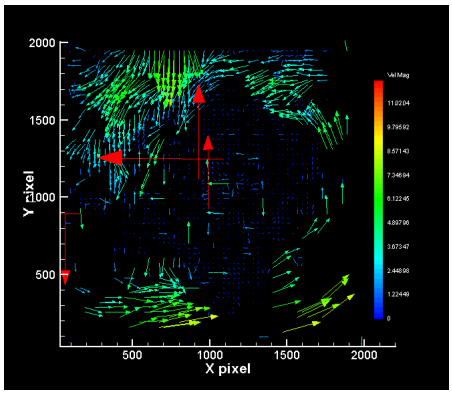

Figure A.162: Additional Vortex Shedding Series 7 at t4

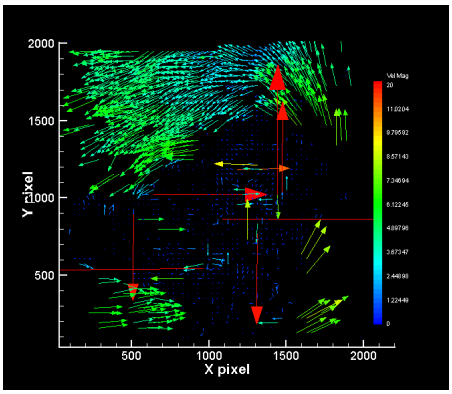

Figure A.163: Additional Vortex Shedding Series 7 at t5

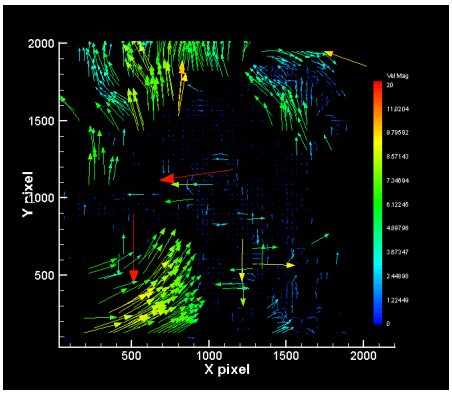

Figure A.164: Additional Vortex Shedding Series 7 at t6

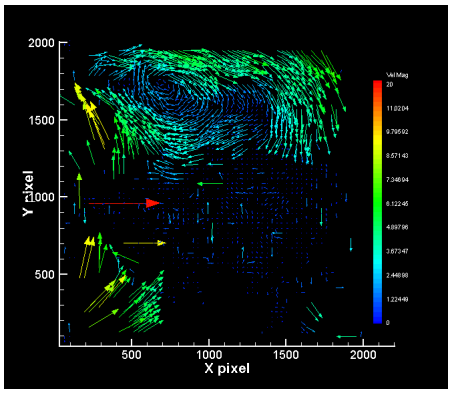

Figure A.165: Additional Vortex Shedding Series 7 at t7

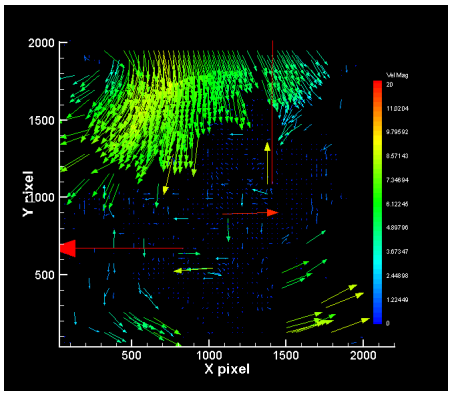

Figure A.166: Additional Vortex Shedding Series 7 at t8

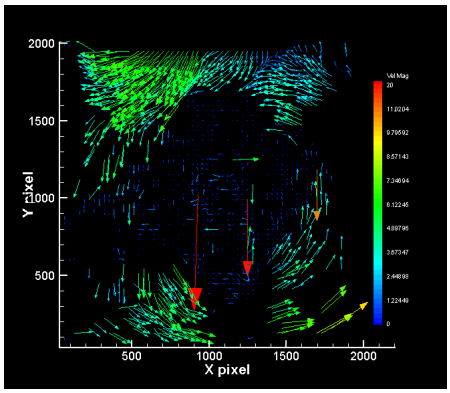

Figure A.167: Additional Vortex Shedding Series 7 at t9

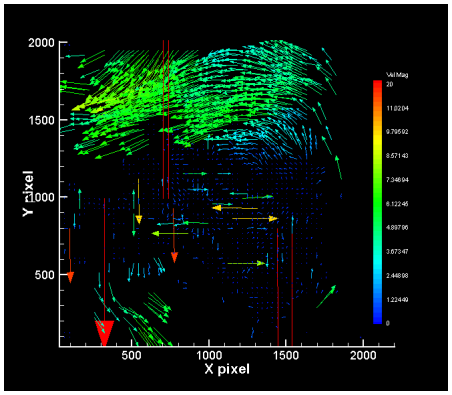

Figure A.168: Additional Vortex Shedding Series 7 at t10

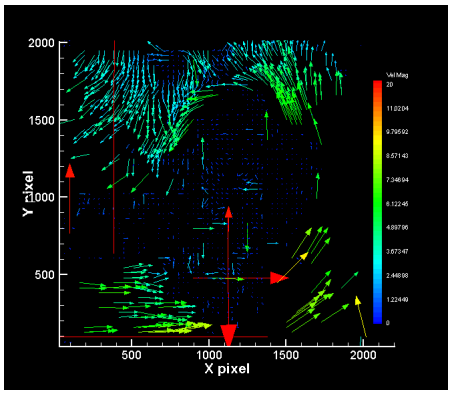

Figure A.169: Additional Vortex Shedding Series 7 at t11

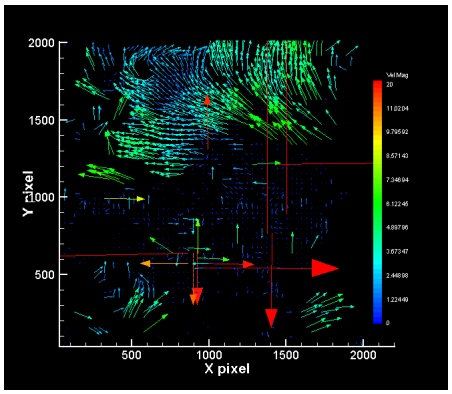

Figure A.170: Additional Vortex Shedding Series 7 at t12

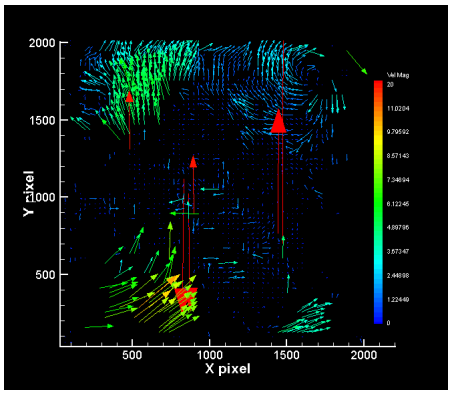

Figure A.171: Additional Vortex Shedding Series 7 at t13

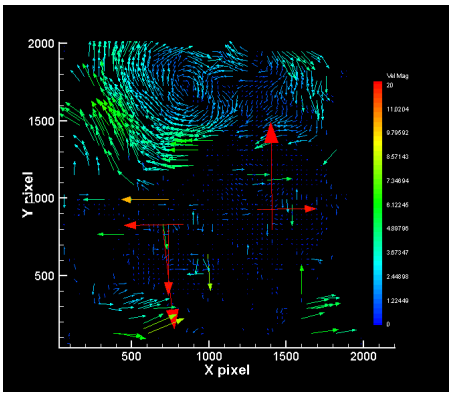

Figure A.172: Additional Vortex Shedding Series 7 at t14

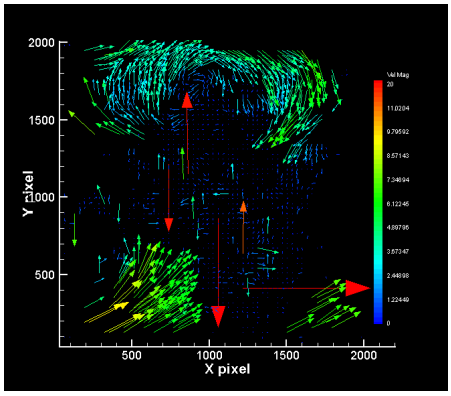

Figure A.173: Additional Vortex Shedding Series 7 at t15

A.8 Additional Vortex Shedding Series 8

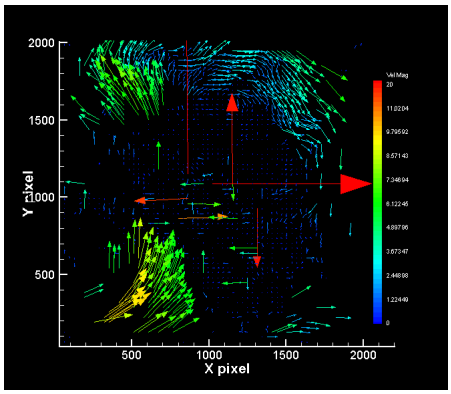

Figure A.174: Additional Vortex Shedding Series 8 at t1

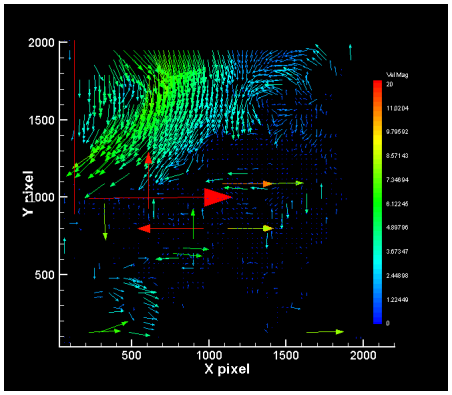

Figure A.175: Additional Vortex Shedding Series 8 at t2

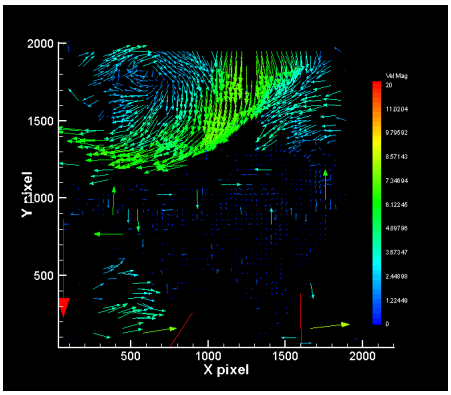

Figure A.176: Additional Vortex Shedding Series 8 at t3

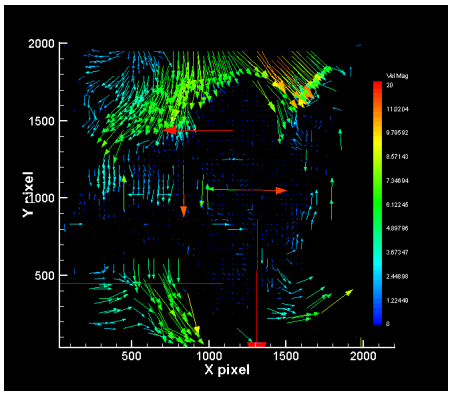

Figure A.177: Additional Vortex Shedding Series 8 at t4

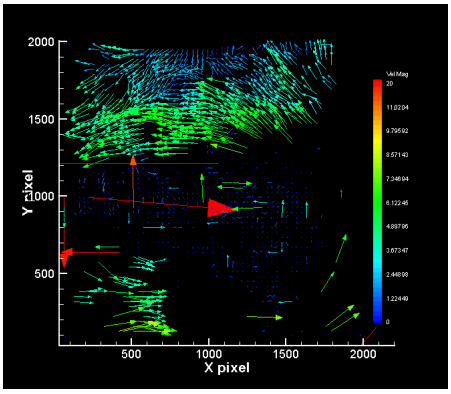

Figure A.178: Additional Vortex Shedding Series 8 at t5

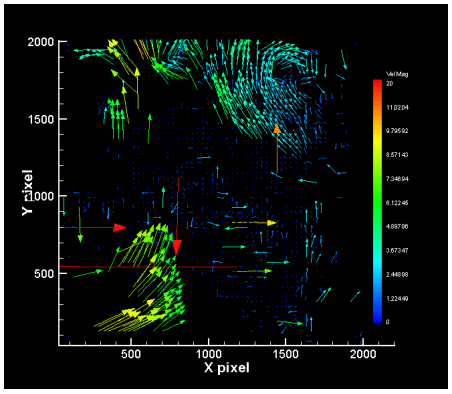

Figure A.179: Additional Vortex Shedding Series 8 at t6

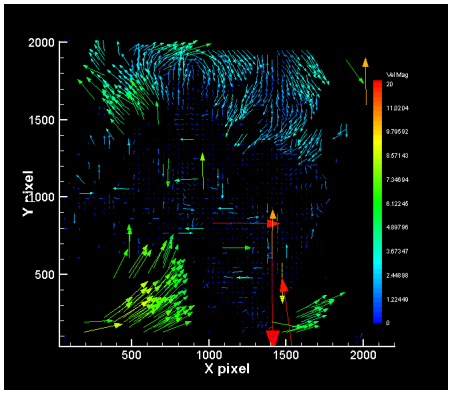

Figure A.180: Additional Vortex Shedding Series 8 at t7

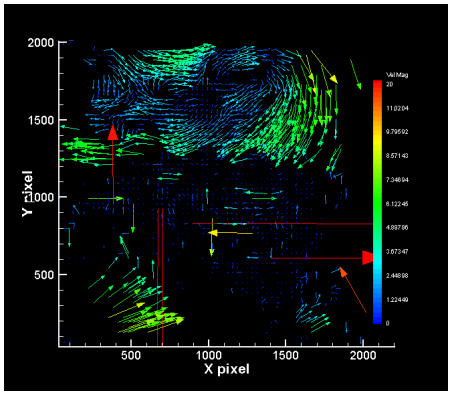

Figure A.181: Additional Vortex Shedding Series 8 at t8

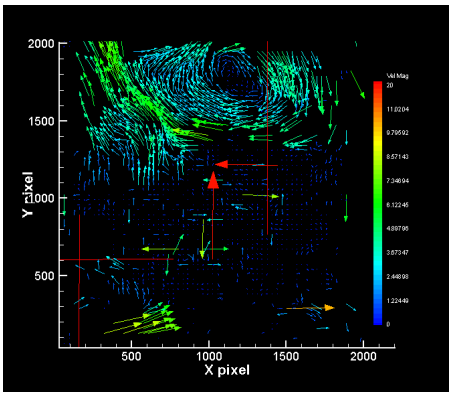

Figure A.182: Additional Vortex Shedding Series 8 at t9

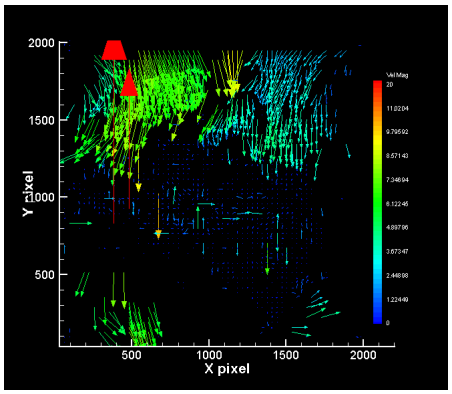

Figure A.183: Additional Vortex Shedding Series 8 at t10

DEPARTMENT OF MECHANICS AND MARITIME SCIENCES
CHALMERS UNIVERSITY OF TECHNOLOGY
Gothenburg, Sweden
www.chalmers.se

CHALMERS
UNIVERSITY OF TECHNOLOGY